



HELSINKI UNIVERSITY OF TECHNOLOGY  
Faculty of Electronics, Communications and Automation  
Department of Micro and Nanosciences

Sardar Bilal Alam

## **Single Compartment Micro Direct Glucose Fuel Cell**

Thesis submitted in partial fulfilment of the requirement for the degree of Master of Science in Technology in Espoo, Finland, 23 November 2009.

Supervisor: Prof. Sami Franssila



# HELSINKI UNIVERSITY OF TECHNOLOGY

## ABSTRACT of the Master's thesis

<b>Author:</b>	Sardar Bilal Alam		
<b>Title of the thesis:</b>	Single Compartment Micro Direct Glucose Fuel Cell		
<b>Date:</b>	23 November 2009	<b>Number of pages:</b>	131
<b>Faculty:</b>	Faculty of Electronics, Communications and Automation		
<b>Professorship:</b>	MT-45, Department of Materials Science and Engineering		
<b>Supervisor:</b>	Prof. Sami Franssila		
<b>Abstract</b> <p>Micro fuel cells have received considerable attention over the past decade due to their high efficiency, large energy density, rapid refuelling capability and their inherent non-polluting aspect. An air breathing abiotically catalyzed single compartment micro direct glucose fuel cell (SC-μDGFC) has been developed using microfabrication technologies. The single compartment of the fuel cell was shared by the anode and cathode that had an interdigitating comb electrodes configuration. The SC-μDGFC compartment was formed of polydimethylsiloxane (PDMS) which exhibits high permeability to oxygen and served as the membrane through which oxygen from ambient environment was able to permeate to the cathode. To minimize the losses associated with fuel crossover, two features were incorporated in the fuel cell: (i) silver was used as the catalyst to selectively reduce oxygen in the presence of glucose and (ii) cathodes were made 25-45μm higher than the anode to reduce access of oxygen to the anode with nickel or platinum catalyst. For 1M glucose/2M KOH solution, an initial OCV of 120-160mV was recorded, which gradually decreased with time and stabilized at 60-75mV. For a fuel cell tested without PDMS membrane, maximum OCV of 135mV and power density of 0.38μW/cm<sup>2</sup> was obtained.</p>			
<b>Keywords:</b> Micro fuel cells, direct glucose fuel cell, microfabrication			



# Preface

---

This study was conducted in the Microfabrication Group (MFG) of Department of Micro and Nanosciences, Faculty of Electronics, Communications and Automation, Helsinki University of Technology (TKK). The basic design concept for the fuel cell was proposed by TKK's Laboratory of Applied Thermodynamics. The fuel cells were fabricated in the TKK's cleanroom facilities at Micronova, Espoo. This work was partly funded by Tekes, Finland.

The work presented in this thesis was made possible by the generous support of a number of people. I would like to thank my supervisor Prof. Sami Franssila for giving me the opportunity to work in MFG. I am thankful for his continuous guidance, support, enthusiasm and most of all his patience. I wish to show my gratitude to my colleagues at MFG, who always helped and advised me whenever I was in need. I appreciate the members of Micronova's MINFAB Group for taking care of chemicals and maintenance matters concerning the cleanroom.

I am thankful to Dr.Jukka-Pekka Spets, Jenni Sallinen and Tuula Noponen of Laboratory of Applied Thermodynamics at TKK for their insightful comments and suggestions. I would like to thank Petri Kanninen from Laboratory of Physical Chemistry and Electrochemistry at TKK for helping me test the fuel cells.

Finally, I would like to express my gratitude and love to my family in Pakistan for their endless support and care regardless of how far away from home I may go. I dedicate this work to my parents Nazli and Zia.

Sardar Bilal Alam  
23 November 2009  
Espoo, Finland.



# Contents

---

<i>Abstract</i>	<b>i</b>
<i>Preface</i>	<b>iii</b>
<i>List of Symbols</i>	<b>ix</b>
<i>List of Abbreviations</i>	<b>xi</b>
<b>Chapter 1 Introduction</b>	<b>1</b>
1.1 Overview.....	1
1.2 Need for micro fuel cells.....	1
1.3 Thesis objective.....	2
1.4 Thesis outline.....	3
<b>Chapter 2 Fuel Cell Theory</b>	<b>5</b>
2.1 Overview.....	5
2.2 Hydrogen fuel cells – basic principle.....	5
2.3 Typical design of a fuel cell.....	8
2.4 Types of fuel cells.....	11
2.4.1 Alkaline fuel cells.....	11
2.4.2 Proton exchange membrane fuel cells.....	13
2.4.3 Direct methanol fuel cells.....	13
2.4.4 Phosphoric acid fuel cells.....	14
2.4.5 Molten carbonate fuel cells.....	14
2.4.6 Solid oxide fuel cells.....	14
2.4.7 Biological fuel cells.....	15
2.5 Fuel cell characteristics.....	16

2.6	Fuel cell performance figures .....	19
-----	-------------------------------------	----

<b>Chapter 3</b>	<b>Micro Fuel Cells</b>	<b>21</b>
------------------	-------------------------	-----------

3.1	Overview .....	21
3.2	Scaling effects .....	21
3.3	Micro proton exchange membrane fuel cell .....	24
3.3.1	Micro flow plates .....	24
3.3.2	Diffusion layer .....	28
3.3.3	Catalyst layer .....	29
3.3.4	Electrolyte .....	31
3.3.5	Stack vs. planar design .....	32
3.3.6	Performance .....	33
3.4	Micro direct methanol fuel cell .....	35
3.5	Micro direct glucose fuel cell .....	36
3.5.1	Operational principle .....	38
3.5.2	Catalyst materials .....	39
3.5.3	Design .....	40
3.5.4	Performance .....	46
3.6	Other micro fuel cells .....	48
3.6.1	Micro direct formic acid fuel cell .....	48
3.6.2	Laminar flow based fuel cell .....	50
3.6.3	Micro solid oxide fuel cell .....	52
3.7	System considerations .....	54
3.7.1	Cell connectivity .....	54
3.7.2	Oxidant delivery .....	55
3.7.3	Fuel delivery .....	55
3.7.4	Water management .....	56
3.7.5	Thermal management .....	57
3.7.6	Load handling .....	57



---

<b>Chapter 4</b>	<b>Single Compartment Micro Direct Glucose Fuel Cell</b>	<b>59</b>
4.1	Overview.....	59
4.2	Design features.....	59
4.3	Fabrication.....	61
4.3.1	UV-LIGA process.....	61
4.3.1.1	Thick film photoresist processing.....	63
4.3.1.2	Copper Electroplating.....	67
4.3.2	Catalyst deposition.....	71
4.3.3	Copper seed layer etching.....	72
4.3.4	PDMS cover/membrane fabrication.....	73
4.3.5	SU-8 master fabrication.....	75
4.3.6	PDMS membrane bonding.....	77
4.3.7	Complete fabrication process.....	77
<b>Chapter 5</b>	<b>Results and Discussion</b>	<b>81</b>
5.1	Overview.....	81
5.2	Fabrication results.....	81
5.2.1	AZ4562 processing.....	83
5.2.2	Electrode electroplating.....	87
5.2.3	Catalyst deposition.....	91
5.2.4	Seed layer etching.....	92
5.2.5	PDMS membrane.....	93
5.2.6	Defect analysis.....	94
5.3	Performance of SC- $\mu$ DGFCs.....	99
<b>Conclusions</b>		<b>105</b>
<b>References</b>		<b>109</b>



# List of Symbols

---

$A$	Area of deposit
$a_i$	Activity of specie $i$
$D$	Diffusion constant
$D_h$	Hydraulic diameter
$E_{act}$	Activation overpotential
$E_L$	Fuel crossover and internal current overpotential
$E_{oc}$	Open circuit voltage
$E_{ohm}$	Ohmic overpotential
$E_{STP}$	Open circuit voltage at standard temperature and pressure
$E_{trans}$	Mass transport overpotential
$F$	Faraday constant
$h$	Thickness of deposit
$I$	Total current
$i$	Current density
$I_o$	Initial current
$L$	Characteristic length
$M$	Molar mass
$n$	Charge of the deposited ion
$Pe$	Péclet number
$P_i$	Partial pressure of specie $i$
$P^\circ$	Standard pressure
$R$	Universal gas constant
$Re$	Reynolds number
$S$	Scaling factor
$T$	Temperature
$t$	Time
$T_j$	Electroplating time
$U$	Mean flow velocity
$V_c$	Operational voltage

$z$	Number of electrons transferred per fuel molecule
$\alpha$	Current efficiency
$\Delta g_F^o$	Standard molar Gibbs free energy
$\Delta i_j$	Current increment
$\Delta t_j$	Time increment
$\Delta p$	Pressure drop
$\eta$	Ideal efficiency
$\mu_f$	Fuel utilization
$\rho$	Density of deposit
$\nu$	Kinematic viscosity

## List of Abbreviations

---

AC	Alternating current
AFC	Alkaline fuel cell
BOP	Balance of plant
CGO	Cerium gadolinium oxide
C-MEMS	Carbon-microelectromechanical systems
CNT	Carbon nano tube
CVD	Chemical vapour deposition
DC	Direct current
DGFC	Direct glucose fuel cell
DIW	De-ionized water
DMFC	Direct methanol fuel cell
DNQ	Diazonaphtoquinone
DRIE	Deep reactive ion etching
EDL	Electric double layer
EMF	Electromotive force
GDE	Gas diffusion electrode
GDL	Gas diffusion layer
HMDS	Hexamethyldisilazane
LFFC	Laminar flow based fuel cell
LIGA	Lithographie, galvanoformung, abformung
MCFC	Molten carbonate fuel cell
MEA	Membrane electrode assembly
MEMS	Microelectromechanical systems
$\mu$ SC-SOFC	Micro single chamber solid oxide fuel cell
$\mu$ DFAFC	Micro direct formic acid fuel cell
$\mu$ DGFC	Micro direct glucose fuel cell
$\mu$ DMFC	Micro direct methanol fuel cell
$\mu$ PEMFC	Micro proton exchange membrane fuel cell

$\mu$ SOFC	Micro solid oxide fuel cell
OCV	Open circuit voltage
PAFC	Phosphoric acid fuel cell
PBS	Phosphate buffered saline
PCB	Printed circuit board
PCL	Polycaprolactone
PDMS	Polydimethylsiloxane
PEB	Post exposure bake
PEM	Proton exchange membrane
PEMFC	Proton exchange membrane fuel cell
PLD	Pulsed laser deposition
PMMA	Polymethylmethacrylate
Pt/C	Carbon supported Pt nano particles
PTFE	Polytetrafluoroethylene
PVD	Physical vapour deposition
RCA	Typical cleaning bath for silicon wafers to remove particles
RF	Radio frequency
RIE	Reactive ion etching
RT	Room temperature
SC- $\mu$ DGFC	Single compartment micro direct glucose fuel cell
SDC	Samaria doped ceria
SEM	Scanning electron microscope
SOFC	Solid oxide fuel cell
UV-LIGA	Ultra violet - lithographie, gavanoformung, abformung
YSZ	Yttria stabilized zirconia

# Chapter 1

## Introduction

---

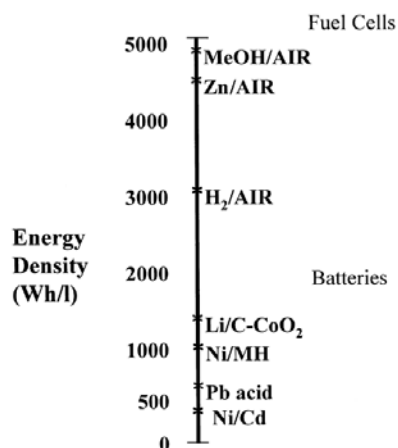
### 1.1 Overview

This chapter advocates the need for developing micro fuel cells, highlights the objective of this thesis and outlines its contents.

### 1.2 Need for micro fuel cells

Manufacturers of portable electronic devices like mobile phones, personal digital assistants, laptops and other portable communication and computing devices are constantly upgrading their products by adding new functionalities. The addition of new functionalities to portable devices along with the trend towards compact design and extended periods of un-tethered operation has put more demand on power sources [1, 5]. The next generation of portable electronic devices require the power sources to have higher energy density and longer operating time between recharges. Lithium-ion or nickel metal hydride based rechargeable batteries have been sufficient in meeting the demands for portable applications. However, in the future, rechargeable batteries will not be adequate to meet the demands for power hungry portable applications. Micro fuel cells, which have higher energy density (i.e., the energy produced per mass or volume of the device) compared to rechargeable batteries (Figure 1.1) and operate for longer times without refueling, represent a true alternative to rechargeable batteries for portable applications [1]. Also, unlike batteries which require certain amount of time to recharge, a micro fuel cell's fuel reservoir can be instantly filled with more fuel to resume

operation. Micro fuel cells are non-polluting technology and hold promise as “green energy” source for portable applications.



**Figure 1.1** Theoretical energy densities. Reproduced from [1].

Micro fuel cells have received considerable attention over the past decade [2]. The publications on micro fuel cells have reported various designs and performance numbers. In addition to academic research labs, companies like Ultracell, Casio, Seiko, Canon, Hitachi, Samsung, Motorola, Fujitsu, Intel and Toshiba are also conducting research in micro fuel cell technology [5]. Generally, micro fuel cells reported in publications have power densities which range from few tenths of  $\mu\text{W}/\text{cm}^2$  up to several hundreds of  $\text{mW}/\text{cm}^2$  [4]. The miniaturization of fuel cell has been made possible by the advancements made in the field of microfabrication [8]. Despite considerable research in micro fuel cells, widespread commercial applications are still several years away [9]. Significant innovations are still required in micro fuel cell technology, particularly at the system level where peripherals integration should be addressed to make micro fuel cells cost effective replacements of batteries [10].

### 1.3 Thesis objective

The objective of this work was to develop a passive air breathing abiotically catalyzed micro direct glucose fuel cell ( $\mu\text{DGFC}$ ) using microfabrication technologies. This work presents the design, fabrication and operation of the  $\mu\text{DGFC}$ . The  $\mu\text{DGFC}$  features a single compartment to host both anode and cathode, and an oxygen permeable membrane. The single compartment design reduces the demands of hybrid integration



needed in more conventional micro fuel cells. The fabricated fuel cells are unique in design and the results obtained are used to evaluate their feasibility.

## **1.4 Thesis outline**

The main body of the thesis is divided into five chapters. Chapter 2 explains the basic theory of fuel cells including the fundamental electrochemistry, components, types and performance parameters. Chapter 3 is a literature review of current micro fuel cell technologies. It discusses the common types of micro fuel cells and summarizes the advancement made in their development. Chapter 4 and 5 are dedicated to the  $\mu$ DGFC presented in this work. Chapter 4 presents the design and fabrication of the proposed single compartment  $\mu$ DGFC. The key microfabrication techniques utilized in fabricating the proposed fuel cell are explained in detail. Results related to the fabrication process and electrical performance of the fuel cells are presented and discussed in Chapter 5. Finally, conclusions are derived from the results and recommendations are made for future work.



# Chapter 2

## Fuel Cell Theory

---

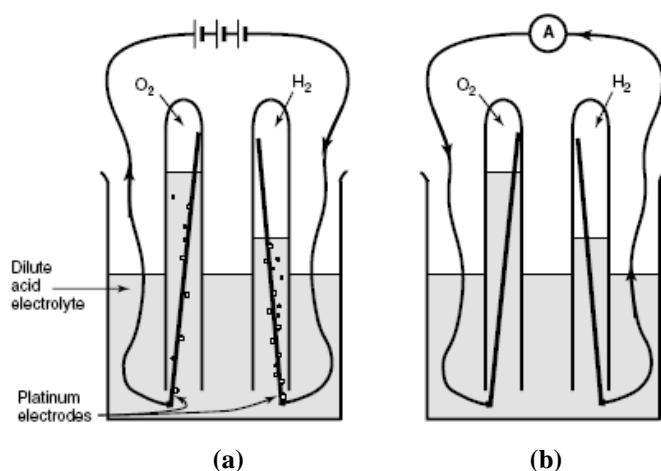
### 2.1 Overview

This chapter briefly explains the basic principal of a fuel cell, its typical assembly, types, characteristics and performance parameters. Fuel cells are electrochemical devices which directly convert chemical energy of a fuel into electrical energy. The invention of fuel cell is credited to William Grove, who demonstrated the first fuel cell in 1839 [6]. Even though fuel cells have evident advantage of high efficiency, the research in fuel cells took well over a century to mature to a level where practical applications were possible. The slow development of fuel cell technology is attributed to the lack of suitable materials for making cheap and high performance fuel cells and to the success of competing technologies like the internal combustion engine. However, in the past decades, development in material science and the need for clean and renewable energy has driven the development of fuel cells. Successful prototypes and commercial fuel cell systems have been fabricated for production of electricity and for portable applications like propulsion of vehicles [11, 12].

### 2.2 Hydrogen fuel cells – basic principle

The basic operation of a fuel cell is very simple. An experiment along the lines of one conducted by William Grove in 1839 is shown in Figure 2.1 [6]. In the experiment, water is first electrolysed into hydrogen and oxygen by a power supply. When the power supply is replaced by an ammeter, a small current is observed, which is depicted by arrows in Figure 2.1 as the flow of electrons from the anode (-) to the cathode (+).

Electric current, along with heat and water, is the by product of re-combination of hydrogen and oxygen. In other words, it may be stated that hydrogen fuel is “burnt” to produce electricity in the reaction:



**Figure 2.1** (a) The electrolysis of water into hydrogen and oxygen. (b) The combination of hydrogen and oxygen to produce electric current. Reproduced from [6].

To understand the flow of current and the source of electrons, the reaction at the anode and cathode has to be examined. At the anode of an acid electrolyte fuel cell, the hydrogen gas ionizes, creating  $\text{H}^+$  ions (or protons), and releasing electrons and energy.

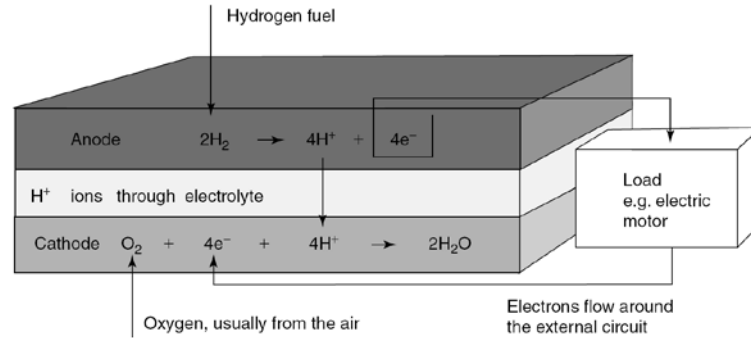


At the cathode, oxygen reacts with electrons taken from the electrode and  $\text{H}^+$  ions from the electrolyte to form water.



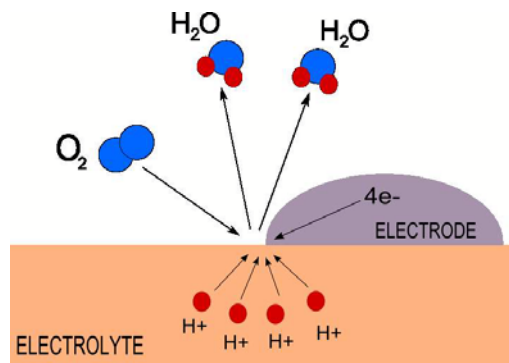
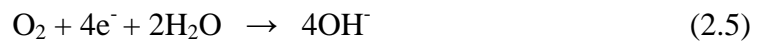
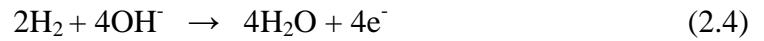
For both reactions to proceed continuously, the electrons from the anode must reach the cathode via an external electric circuit (load). The  $\text{H}^+$  ions reach the cathode through the electrolyte. The electrolyte can be any medium that can support the movement of free  $\text{H}^+$  ions or protons. An acid, which has free  $\text{H}^+$  ions, was the natural choice of electrolyte in the early development of fuel cells. Certain solid polymers can be tailored to support mobile  $\text{H}^+$  ions (or protons). The flow of electrons through the

external circuit and transport of protons through the electrolyte are explained in Figure 2.2.



**Figure 2.2** Electrode reaction and charge flow for an acid electrolyte fuel cell.  
Reproduced from [6].

In an alkaline electrolyte fuel cell the overall reaction is the same as for acid electrolyte fuel cells, but the reactions at each electrode is different. In an alkali the hydroxyl ( $\text{OH}^-$ ) ions are available and mobile. Equation 2.4 and 2.5 present the reactions at the anode and cathode respectively:



**Figure 2.3** The protons from electrolyte (liquid), the electrons from the electrode (solid) and oxygen (gas) combine at the three phase contact area to form water.

If we consider Eq.2.4, the fuel ( $\text{H}_2$ ) and the hydroxyl ion should “come together” on the surface of the electrode, so that the electrons produced can be transferred to the

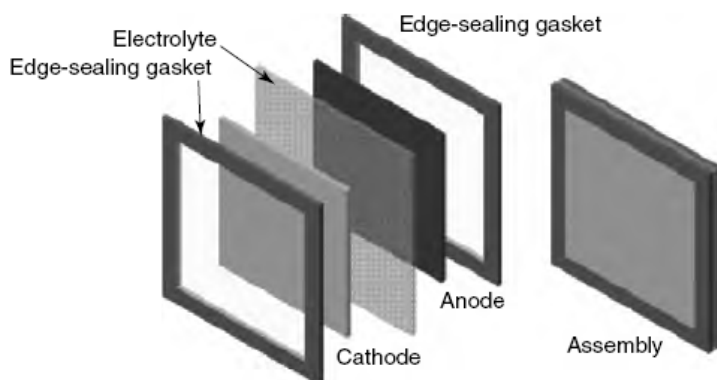
external circuit. This reaction involving fuel or oxygen (usually gas), electrolyte (usually liquid) and the electrode (solid) is referred to as the three phase contact. The bringing together of the electrons, the ions and fuel or oxygen is a very critical issue in fuel cell design. Three phase contact area is illustrated for Eq. 2.3 in Figure 2.3.

## 2.3 Typical design of a fuel cell

The setup in Figure 2.1 serves well to explain the basic principal of fuel cells; however such a design is not suitable for practical purposes since very small current is generated. The main reasons for small current are:

- small three phase contact area, which in case of Figure 2.1 is only a ring where the electrode emerges out of the electrolyte.
- large distance between the electrodes; the electrolyte resists the flow of ions and thus of the current [6].

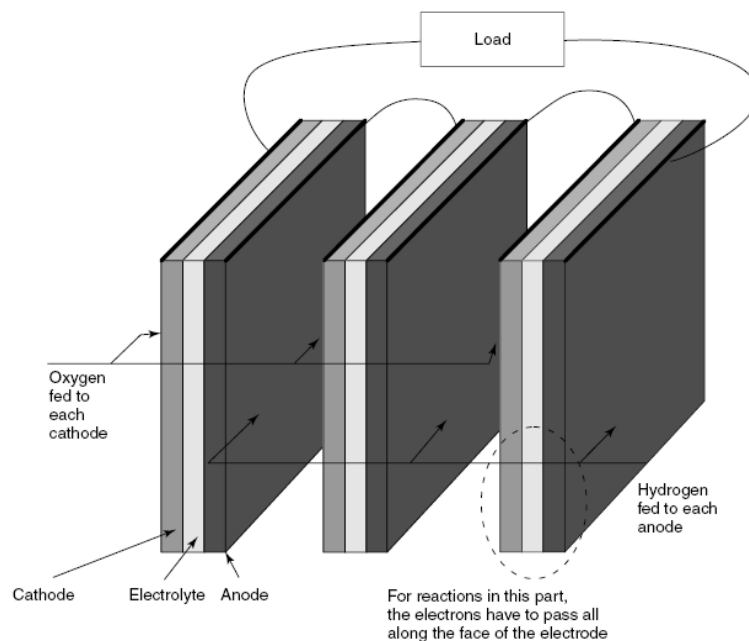
These problems can be overcome by making the electrodes flat and using a thin layer of electrolyte between them (Figure 2.4). The electrolyte, besides conducting ions between anode and cathode, also serves as a gas separator and electronic insulator. To improve the three phase contact, the structure of the electrode is made porous so that both the electrolyte from one side and the gas from the other can penetrate it. The surface area of electrodes is very critical for fuel cells, since the reaction rates are proportional to the electrode's surface area. Modern fuel cells electrodes have microstructures that gives them surface area that can be hundred to thousand times their straight forward geometrical area (length x width). In addition to micro structured surface, fuel cell electrodes usually have to incorporate suitable catalyst to increase the reaction rate.



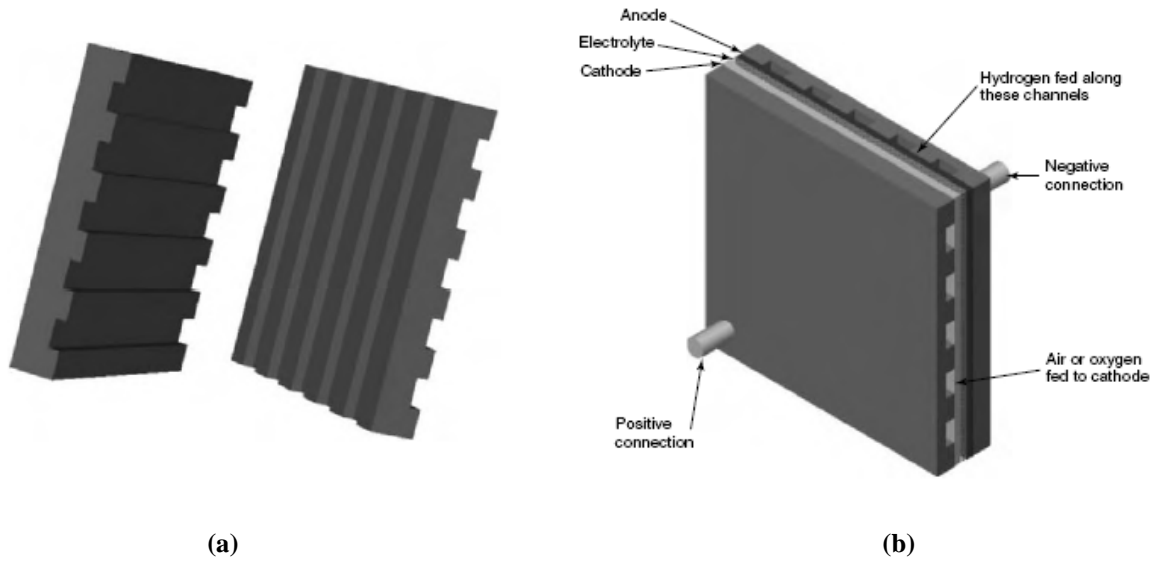
**Figure 2.4** Construction of cathode/electrolyte/anode assembly with edge seals.

Reproduced from [6].

When drawing a useful current, the voltage of a fuel cell is quite small, about 0.7 V [6]. To produce useful voltage a collection of fuel cells are connected in series. This collection of fuel cells connected in series is known as the fuel cell stack. The most obvious way to achieve this is to connect the edge of each anode to the cathode of the next, all along the line, as shown in Figure 2.5. The disadvantage of this approach is that electrons have to flow across the face of the electrode to reach the current collector at the edge. The electrodes might be good conductors of electricity but since voltage for each cell is low (ca. 0.7 V), even small drop in voltage is important. For efficient current collection, bipolar plate is used (Figure 2.6). Bipolar plate makes connections all over the surface of the cathode and the anode of the next cell (hence named bipolar) and at the same time, serves as a means of feeding oxygen to the cathode and fuel gas to the anode (Figure 2.7). The bipolar plates are made of good conductors like graphite, stainless steel or mouldable graphite-polymer composite material [12] and have channels cut in them so that the gases can flow over the face of the electrodes, hence they are also called flow plates. The channels in the flow plate are designed to ensure even distribution of reactants across the electrode.

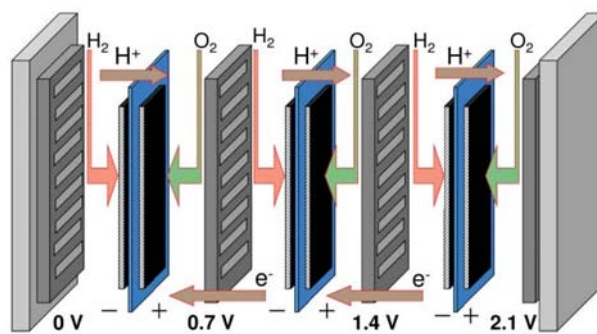


**Figure 2.5** Simple edge connection of three cells in series. Reproduced from [6].



**Figure 2.6** (a) Two bipolar plates of very simple design. (b) Single fuel cell with end plates for collecting current all over the face of the electrodes and to supply gas to the whole electrode.

Reproduced from [6].



**Figure 2.7** Schematic, simplified overview of a fuel cell stack. Reproduced from [12].

The fuel cell stack is the core of a fuel cell power system. However, additional subsystems are also needed to operate the fuel cell stack in a practical application. These additional components are often called the balance of plant (BOP) [6]. The extra components required depend on the size and type of the fuel cell, and also on the type of fuel used. The BOP specifically addresses supply and control of the reactants (air and fuel) and removal of the by-products (heat and water). Sensors to monitor and control the flow of reactants, the removal of by-products, temperature, and pressure are necessary components of a BOP. Pumps, blowers and/or compressors usually make up the delivery systems for circulating the reactants. Major components of the thermal management subsystem include the heat exchanger, cooling plates, and pumps and controllers for coolant flow. Water management is addressed by using components like



reservoirs, accumulators, humidifiers, condensers and pumps. The direct current (DC) output of a fuel cell usually does not meet the demands of an electrical load. Thus, some kind of power conditioning is required. This is accomplished by components like amplifiers, voltage regulators, DC-DC convertors or DC-AC convertors.

## 2.4 Types of fuel cells

Conventional fuel cells are usually classified by the electrolyte employed in the cell. An exception to this classification is the Direct Methanol Fuel Cell (DMFC), in which methanol is directly feed to the anode. The electrolyte of this cell is not determining for its class. A second grouping can be done by looking at the operating temperature for each of the fuel cells. There are, thus, low-temperature and high-temperature fuel cells. Low-temperature fuel cells are the Alkaline Fuel Cell (AFC), the Polymer Electrolyte or Proton Exchange Membrane Fuel Cell (PEMFC), the Direct Methanol Fuel Cell (DMFC) and the Phosphoric Acid Fuel Cell (PAFC). The high-temperature fuel cells operate at temperatures approx. 600 - 1000 °C and two different types have been developed, the Molten Carbonate Fuel Cell (MCFC) and the Solid Oxide Fuel Cell (SOFC). In addition to the major fuel cells presented in Table 2.1, another class of fuel cell, Biological Fuel Cell (biofuel cell), has gained much attention in recent years [13]. Biofuel cell normally use organic fuel such as ethanol or glucose and employ biocatalyst to promote reactions. All major types of fuel cells are briefly discussed in this section.

### 2.4.1 Alkaline fuel cells

AFC was one of the first fuel cells to be used in space. It was used for Apollo mission and the Space Shuttle program. The electrolyte of the AFC consists of liquid potassium hydroxide (KOH) usually in concentrations of 30-45 wt.%. KOH electrolyte has an advantage over acid fuel cells, which is that the oxygen reduction kinetics are much faster in alkaline electrolyte than in acid making the AFC a very attractive system for specific applications [11]. The AFC exhibits the highest electrical efficiencies of all fuel cells but it works properly with only very pure gases, which is considered a major constraint for most applications. AFCs are normally operated at temperatures below 100°C. AFC electrodes used to be Ni based catalysts sometimes activated with Pt. Carbon supported platinum nanoparticles (Pt/C) based gas diffusion electrodes are now generally used for both the anode and cathode. These days advance catalysts like Pt-Co

or Pt-Pd are also being suggested [11]. Three types of AFC designs exist: static electrolyte AFC, mobile electrolyte AFC and dissolved fuel AFC. In static electrolyte AFC, the KOH is held in a matrix material between the electrodes of each stack [6]. In mobile electrolyte AFC, KOH is circulated between the electrodes. The main advantage of mobile electrolyte over static electrolyte is that it can be replaced from time to time. This is necessary because the carbon dioxide in the air will react with KOH to form potassium carbonate. The formation of carbonate will destroy the electrolyte as the  $\text{OH}^-$  ions are replaced by  $\text{CO}_3^{2-}$  ions. Thus, pure oxygen at the cathode is almost obligatory for matrix-held electrolytes. In dissolved fuel AFC, the KOH electrolyte solution is mixed with the fuel such as hydrazine or ammonia. The fuel is fully in contact with both the anode and cathode. Dissolved fuel AFC is more suitable for low power applications [6].

**Table 2.1** Data for major types of fuel cells [11].

Fuel Cell Type	Fuel	Electrolyte	Charge carrier in the Electrolyte	Anode Reaction	Cathode Reaction	Operating Temp. (°C)
Alkaline (AFC)	Hydrogen	Immobilized or mobilized potassium hydroxide	$\text{OH}^-$	$\text{H}_2 + 2\text{OH}^- \rightarrow 2\text{H}_2\text{O} + 2\text{e}^-$	$\frac{1}{2}\text{O}_2 + \text{H}_2\text{O} + 2\text{e}^- \rightarrow 2\text{OH}^-$	<100
Proton Exchange Membrane (PEMFC)	Hydrogen	Proton conducting polymer	$\text{H}^+$	$\text{H}_2 \rightarrow 2\text{H}^+ + 2\text{e}^-$	$\frac{1}{2}\text{O}_2 + 2\text{H}^+ + 2\text{e}^- \rightarrow \text{H}_2\text{O}$	60 - 120
Direct Methanol (DMFC)	Methanol	Proton conducting polymer	$\text{H}^+$	$\text{CH}_3\text{OH} + \text{H}_2\text{O} \rightarrow \text{CO}_2 + 6\text{H}^+ + 6\text{e}^-$	$\frac{3}{2}\text{O}_2 + 6\text{H}^+ + 6\text{e}^- \rightarrow 3\text{H}_2\text{O}$	60 - 120
Phosphoric Acid (PAFC)	Hydrogen	Immobilized liquid phosphoric acid	$\text{H}^+$	$\text{H}_2 \rightarrow 2\text{H}^+ + 2\text{e}^-$	$\frac{1}{2}\text{O}_2 + 2\text{H}^+ + 2\text{e}^- \rightarrow \text{H}_2\text{O}$	160 - 220
Molten Carbonate (MCFC)	Reformed hydrocarbons	Immobilized liquid molten mixture of alkaline metal carbonates	$\text{CO}_3^{2-}$	$\text{H}_2 + \text{CO}_3^{2-} \rightarrow \text{H}_2\text{O} + \text{CO}_2 + 2\text{e}^-$	$\frac{1}{2}\text{O}_2 + \text{CO}_2 + 2\text{e}^- \rightarrow \text{CO}_3^{2-}$	600 - 800
Solid Oxide (SOFC)	Hydrogen / reformed hydrocarbons	Oxygen ion conducting ceramic (stabilized zirconia)	$\text{O}^{2-}$	$\text{H}_2 + \text{O}^{2-} \rightarrow \text{H}_2\text{O} + 2\text{e}^-$	$\frac{1}{2}\text{O}_2 + 2\text{e}^- \rightarrow \text{O}^{2-}$	500 - 1000

### 2.4.2 Proton exchange membrane fuel cells

PEM fuel cells use a proton exchange membrane (PEM) as an electrolyte. They are low-temperature fuel cells, generally operating between  $85\pm 105^{\circ}\text{C}$ . Cold start, below  $0^{\circ}\text{C}$ , is possible [12]. PEM is an ion conducting polymer and the mobile ion in the polymer is  $\text{H}^{+}$  ion (protons). The different companies producing polymer electrolyte membranes have their own special tricks, mostly proprietary. However, a common theme is the use of sulphonated fluoropolymers, usually fluoroethylene [6]. Membranes in PEM fuel cells are generally water filled to keep the conductivity high. A dried out membrane possesses a lower conductivity as proton transport through a wet membrane is similar to that of an aqueous solution. Since PEM has to be kept well humidified, water management is one of the major issues in PEM technology. Electrodes for PEM fuel cells are generally porous gas diffusion electrodes to ensure the supply of the reactant gases to the active zones where the noble metal catalyst (usually Pt) is in contact with the ionic and electronic conductor. Pt dispersed on carbon or other small Pt particles (such as colloids) usually form the cathode or anode. CO is one of the major poisons in low temperature fuel cells [11]. In PEMFC CO poisoning occurs due to adsorption of the species to the active sites of the Pt catalysts so that no sites are available for reaction with  $\text{H}_2$ . CO-tolerant anodes, which usually contain Pt-Ru alloys, have been used and investigated.

### 2.4.3 Direct methanol fuel cells

DMFCs are similar to PEMFCs. They use proton exchange membrane (PEM), as the electrolyte and operate at similar temperatures. In a DMFC, methanol is directly fed into the fuel cell without the intermediate step of reforming the alcohol into hydrogen. The power density of the DMFC is considerably lower than that of the PEMFC [12]. This is because in DMFC, the fuel anode reactions proceed slowly than with hydrogen when Pt is used as anode catalyst. The oxidation of hydrogen occurs readily compared to the oxidation of methanol, which is a much more complex reaction, and proceeds much more slowly. Bimetals and higher catalyst loading has been found to improve the performance of DMFC. Pt/Ru alloys are the most widely used anode catalyst for DMFC [6, 11]. For oxygen reduction, like in PEMFC, Pt is used as the catalyst. DMFC performance is also affected by the methanol crossover. PEM in DMFC readily absorb methanol, which mixes well with water, and so quickly reaches the cathode. At the

cathode, methanol causes a mixed potential due to the interference of methanol oxidation with the oxygen reduction reaction.

#### **2.4.4 Phosphoric acid fuel cells**

In PAFC, the electrolyte is an inorganic acid; concentrated phosphoric acid (nearly 100%) which, like the membranes in the PEM cells, will conduct protons. As with the PEM fuel cells, Pt or Pt alloys are used as the catalyst at both electrodes. The advantages of the PAFC are its simple construction, its stability thermally, chemically, and electrochemically, and the low volatility of the electrolyte at operating temperatures (150-200°C) [6,11]. These factors probably assisted the earlier deployment of PAFC into commercial systems compared to the other fuel cell types. Pure 100 % phosphoric acid has a freezing point of 42°C. To avoid stresses caused by freezing and/ or thawing, PAFCs are always kept at a higher temperature once they are commissioned. Due to their higher operating temperature, they are less sensitive to CO impurities in the fuel and water management is less of an issue [6].

#### **2.4.5 Molten carbonate fuel cells**

An interesting feature of MCFC is that it requires CO<sub>2</sub> in the air to work. The electrolyte of the MCFC is a molten mixture of alkali metal carbonates which is retained in a ceramic matrix of LiAlO<sub>2</sub>. The electrolyte is usually a binary mixture of lithium and potassium, or lithium and sodium carbonates, which at high operating temperatures (typically 600–700°C) is highly conductive, with carbonate CO<sub>3</sub><sup>2-</sup> ions providing the ionic conduction. High operating temperature of MCFC allows the use of non-noble catalysts along with direct internal processing of fuels such as natural gas. Ni was used as the catalyst for anode during the early development of MCFC. However, Ni was found to be unstable under MCFC operating conditions and has been replaced by Ni-Al or Ni-Cr alloy [11]. Cathodes for MCFCs are usually NiO made by an anodic oxidation of a Ni sinter or by an in-situ oxidation of Ni metal during the cell start-up time. NiO cathodes are active enough for oxygen reduction at high temperatures so that a Pt based metal is not necessary.

#### **2.4.6 Solid oxide fuel cells**

The SOFC is a complete solid-state device that uses an oxide ion-conducting ceramic material as the electrolyte and operates in the temperature range of 500 to 1000°C.

SOFC is simple as compared to other fuel cells since it is a two phases (gas and solid) system and has no problem with water management, flooding of the catalysts layer or slow oxygen reduction kinetics [6, 11]. As with the MCFC, the high operating temperature translates into non-noble catalysts, direct internal hydrocarbon fuel processing and high quality waste heat that can be utilized in combined-cycle power plants. Zirconia doped with yttria (yttria-stabilised zirconia (YSZ)) is the most effective electrolyte for the high-temperature SOFC, although several others have been investigated including  $\text{Bi}_2\text{O}_3$ ,  $\text{CeO}_2$ , and  $\text{Ta}_2\text{O}_5$  [6]. The anode of state of the art SOFCs is a cermet made of metallic nickel and a YSZ skeleton. The anode has a high porosity (20–40%) so that mass transport of reactant and product gases is not inhibited. Similar to the anode, the cathode is a porous structure that must allow rapid mass transport of reactant and product gases. Strontium-doped lanthanum manganite ( $\text{La}_{0.84}\text{Sr}_{0.16}\text{MnO}_3$ ), a *p*-type semiconductor, is most commonly used for the cathode material [6].

#### 2.4.7 Biological fuel cells

Biological fuel cells (biofuel cells) are defined as those fuel cells which employ biocatalysts like enzymes or microorganism instead of metallic inorganic catalysts [13, 14]. Biofuel cells normally use organic fuel, such as glucose, ethanol or even larger molecules like soluble starches, and tend to operate under mild conditions; 20–40°C and near neutral pH [13]. Fuel cells which use biological fuel but have inorganic catalysts are not defined as biofuel cells. Biofuel cells are categorized according to the source of the biocatalysts into two main types: enzymatic and microbial biofuel cell. Enzymatic biofuel cells use enzyme for catalysis. A major benefit of using enzymes is that each individual enzyme is tailored for specific reaction catalysis. A major benefit of the specificity of enzyme catalysis is that fuel and oxidant can be mixed together, and anode and cathode can be housed in a single compartment without the need for a membrane. This simplifies the fuel cell design and eliminates fuel crossover. Microbial fuel cells use whole living microorganisms for catalysis. Microbial fuel cells can work with a variety of biofuel feeds, are resistant to poisoning, and are usually capable of oxidizing the fuel completely to carbon dioxide and water [13, 14].

Current biofuel cells lag behind conventional fuel cells in terms of current densities and voltage [13]. At present they are only suitable for low power applications. A disadvantage of enzymatic biocatalysts is their limited lifetime, which is usually a few days or in favorable cases a few weeks [13,15]. A critical factor in the design of biofuel

cells is the inefficient conduction of electrons between the biocatalyst and the electrode [15]. The electrons are either directly transferred between the reaction site on the biocatalyst and the surface of the electrode, or a mediator molecules is used to relay the electrons [13, 15].

## 2.5 Fuel cell characteristics

The electromotive force (EMF) or the reversible open circuit voltage (OCV) of a fuel cell is given as:

$$E_{oc} = \frac{-\Delta g_F^o}{zF} \quad (2.6)$$

where  $E_{oc}$  is the OCV,  $z$  is the number of electrons transferred for each molecule of fuel,  $F$  is the Faraday constant, and  $\Delta g_F^o$  is the standard molar Gibbs free energy released during the fuel cell reaction and is equal to the electrical work done. The negative sign is due to the fact that Gibbs free energy is liberated. Gibbs free energy is dependent on the reactant pressure, concentration and temperature.

The Nernst equation expresses the dependence of Gibbs free energy on reactant pressure, concentration and temperature. The reversible Nernst voltage of hydrogen fuel cell is given as:

$$E_{oc} = E_{STP} + \frac{RT}{2F} \ln \left( \frac{a_{H_2} a_{O_2}^{\frac{1}{2}}}{a_{H_2O}} \right) \quad (2.7)$$

where  $E_{STP}$  is the OCV at standard temperature and pressure,  $R$  is the universal gas constant,  $T$  is the actual temperature, and  $a_i$  is the activity of the specie  $i$ . The activity is defined as:

$$a_i = \frac{P_i}{P^o} \quad (2.8)$$

where  $P_i$  is the partial pressure of the specie  $i$  and  $P^\circ$  is the standard pressure, or 0.1 MPa. If we apply Equation 2.8 to Equation 2.7, and assume that the  $H_2O$  vapours produced behave as an ideal gas and the pressures are given in bar, we get:

$$E_{oc} = E_{STP} + \frac{RT}{2F} \ln \left( \frac{P_{H_2} P_{O_2}^{\frac{1}{2}}}{P_{H_2O}} \right) \quad (2.9)$$

In an operational fuel cell, knowledge of the Nernst voltage requires knowledge of partial pressures of all species involved in the reaction. In most fuel cell experiments involving hydrocarbons, the partial pressures of the species are neither controlled nor measured and operational fuel cell voltage are simply compared to the standard potential [16].

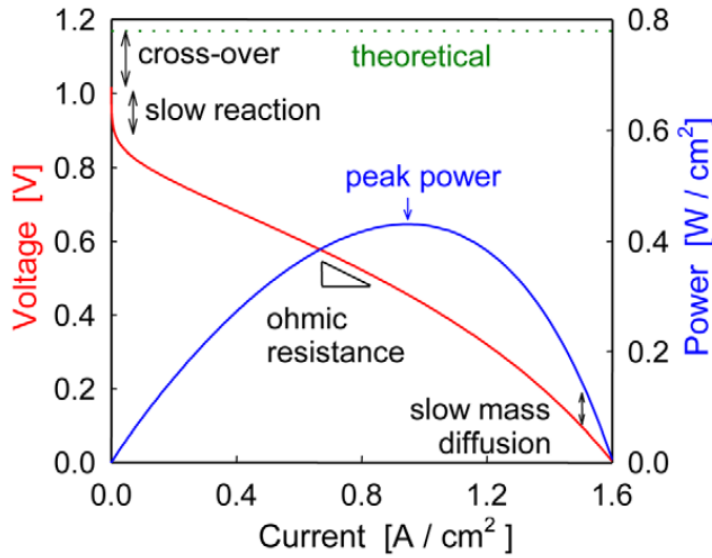
Eq. 2.6 (and 2.9) gives the maximum theoretical value of fuel cell output voltage since it assumes no irreversibilities (i.e. 100% efficiency). In practical fuel cells, when the current is drawn, the operational voltage ( $V_c$ ) will drop due to certain losses. By considering the losses, the measured voltage of the fuel cell can be written as:

$$V_c = E_{oc} - E_L - E_{act} - E_{ohm} - E_{trans} \quad (2.10)$$

In this equation,  $E_{oc}$  is the reversible OCV given by equation 2.6,  $E_L$  is the loss in voltage due to leaks across the electrolyte,  $E_{act}$  is the activation overpotential due to slow electrode reactions,  $E_{ohm}$  is the overpotential due to ohmic resistance in the cell, and  $E_{trans}$  is the overpotential due to mass transport limitations. The losses can be studied by examining the polarization curve of the fuel cell since each loss is dominant at different current stage (Figure 2.8).

In open circuit conditions when no current is drawn from the fuel cell, the measured voltage should be equal to the Nernst voltage. However, due to leakages in the electrolyte or poor sealing, the fuel will diffuse from the anode through the electrolyte to the cathode. At the cathode, it will react directly with the oxygen due to the catalyst, producing no current that flows through the external circuit. The leakage of oxygen to the anode will cause similar effect. This is known as fuel crossover and this problem becomes very significant for membraneless single compartment fuel cells. The

electrolyte may also have partial electronic conductivity which causes internal currents in the cell. The fuels cross over and internal currents define  $E_L$ .



**Figure 2.8** Schematic fuel cell polarization (voltage vs. current density) and power density curves. Reproduced from [16].

Activation overpotential ( $E_{act}$ ) is associated with the activation energy required to overcome the resistance to charge transfer. The resistance to charge transfer results in slow reaction rate. A part of the voltage generated is lost in driving the chemical reaction that transfers the electron to or from the electrode. Activation overpotential is dominant at lower currents and is almost entirely due to sluggish oxygen reduction at the cathode [6, 16].  $E_{act}$  can be reduced by increasing the cell temperature, using more effective catalysts, increasing active area of the electrodes, increasing the reactant concentration and by increasing the pressure.

Ohmic overpotential ( $E_{ohm}$ ) is due to the resistance to flow of electrons through the material of the electrodes, and the various interconnections, as well as the resistance to the flow of ions through the electrolyte.  $E_{ohm}$  is proportional to the current density and partly characterize the linear region in the I-V curve in Figure 2.8.

Mass transport (or concentration) overpotential ( $E_{trans}$ ) describes the losses caused by the restrictions to the transport of the reactant gases to the reaction sites and by the ineffective removal of by-products.  $E_{trans}$  is generally established by the rate of reactants flowing to the electrolyte through the electrodes and the rate of the products flowing away [16]. Mass transport losses become severe as current is increased because as greater current is drawn, the reactant depletion zone or the by-product build-up will



become greater [16]. In practical situation, this means that ineffective transport of the reactants will limit the maximum current density that can be achieved by a fuel cell. In free air breathing micro fuel cells, the transport losses could dominate and limit the fuel cell performance [9,10].

From the above discussion, we can define the material requirements for the components of a fuel cell. The electrolyte of the fuel should have (i) high ionic conductivity, (ii) negligible electronic conductivity, (iii) chemical stability with electrodes, (iv) impermeability to gases, and (v) sufficient mechanical stability so that its thickness can be minimized and development of cracks and pores is avoided. The demands on the fuel cell electrodes are also strict. The electrode should have (i) sufficient porosity and high surface area, (ii) have good electronic and ionic conductivity and (iii) good electrochemical activity to promote redox reactions.

## 2.6 Fuel cell performance figures

Certain key figures are used to compare the fuel cells with each other and also, with other power generators. For comparing fuel cell electrodes and electrolyte, current density is the key figure [6]. Current density is defined as the current per unit area (of the electrode) and it is usually given in mA/cm<sup>2</sup>. The figure of current density should be given for a specific operating voltage.

The current density and the corresponding operating voltage can be multiplied to give the power density. Power density, defined as power per unit area, is a key performance figure for a fuel cell and is usually given in mW/cm<sup>2</sup>. Power density is widely used in comparing miniature fuel cells. For the complete fuel cell system which includes BOP, a key figure of merit is volumetric power density defined as power per unit volume. Another metric used for complete fuel cells systems is specific power. Specific power is defined as power per unit mass. To evaluate the specific power, the mass of various components of the system like fuel cell stack, fuel(s) and BOP components are considered. Another, important performance figure for fuel cells is the efficiency. The ideal efficiency ( $\eta$ ) of a fuel cell is given as:

$$\eta = \mu_f \frac{V_c}{E_{ocv}} 100\% \quad (2.11)$$

where  $\mu_f$  is fuel utilization coefficient, which accounts for the fact that in practical situations not all fuel that is fed to a fuel cell can be used. Some fuel has to pass through un-reacted.  $\mu_f$  is defined as:

$$\mu_f = \frac{\text{mass\_of\_fuel\_reacted\_in\_cell}}{\text{mass\_of\_fuel\_input\_to\_cell}} \quad (2.12)$$

# Chapter 3

## Micro Fuel Cells

---

### 3.1 Overview

A variety of micro fuel cells have been implemented using different materials and a wide range of MEMS technologies [2-5, 9, 10, 17]. PEMFC and DMFC have been extensively investigated as the most viable candidates for portable applications [3,5, 10, 17]. In addition to PEMFC and DMFC, direct glucose fuel cells (DGFC) are also considered for miniaturization. The key driver for miniaturization of DGFC is the fact that glucose and oxygen are readily available body fluids. This makes implantable fuel cells [18] an attractive possibility. In this chapter, a literature review of the recent progress made in micro PEMFC, DMFC and DGFC is presented. Some alternate micro fuel cell technologies are also briefly discussed. In practice, a micro fuel cell stack cannot operate on its own. It requires BOP components to maintain its operation. The requirements imposed by micro fuel cell system on its BOP are also discussed.

### 3.2 Scaling Effects

The theory discussed in Chapter 2 is valid for both macro and micro scale fuel cells. However, there are certain physical effects which are unique to micro fuel cells due to their micro scale dimensions [3, 19]. These effects can be explained by the scaling law. For a scaling factor of  $S$ , the surface area to volume ratio is given as:

$$\frac{\text{surface\_area}}{\text{volume}} \propto \frac{S^2}{S^3} = S^{-1} \quad (3.1)$$

In case of miniaturization,  $S < 1$  and  $S^{-1} > 1$ . From Equation 3.1, we can conclude that the surface effects are more dominate for micro fuel cells. This translates into an improvement in reaction conditions and cell performance [3].

Scaling law also helps in explaining the mass transport mechanism in micro fuel cells. The flow phenomenon in micro fuel cells is different from macro fuel cells due to the micro scale dimensions of the channels of flow plates (bipolar plates). The flow in micro fuel cells can be defined with the help of two dimensionless numbers: Reynolds number (Re) and Péclet number (Pe). Re gives a measure of the ratio of inertial forces to viscous forces [20]. Re is given as [3]:

$$\text{Re} = \frac{UD_h}{\nu} \quad (3.2)$$

where  $D_h$  is the hydraulic diameter of the channel,  $U$  is the mean flow velocity and  $\nu$  is the kinematic viscosity. For Equation 3.2,  $U$  and  $\nu$  are assumed to be constant. For mircochannels, Reynolds number is typically low ( $\text{Re} < \sim 500$ ), which means that the flow in micro fuel cells is laminar due to the dominance of viscous forces over inertial forces [20].

Pe estimates the relative importance of mass transfer by convection compared with mass transfer by molecular diffusion [20]. Pe is given as:

$$\text{Pe} = \frac{UL}{D} \quad (3.3)$$

where  $L$  is the characteristic length and  $D$  is the diffusion coefficient.  $U$  and  $D$  are considered constant in Equation 3.3.  $\text{Pe} \gg 1$  indicates convection is responsible for mass transfer, whereas  $\text{Pe} \ll 1$  means that diffusion is the dominate transport mechanism. The diffusion coefficient  $D$  of liquids is several orders of magnitude smaller than those of gases. Thus, Péclet number is relatively large for liquid fuels (like methanol for  $\mu\text{DMFC}$ ) compared to gases (like  $\text{H}_2$  for  $\mu\text{PEMFC}$ ) flowing in the mircochannel. Hence, in micro fuel cells such as  $\mu\text{DMFC}$  that utilizes liquid fuel, convection is the dominate mode of mass transfer and this may prevent the diffusion of fuel towards the PEM [3]. Relatively small Péclet number for  $\text{H}_2$  flow in  $\mu\text{PEMFC}$

facilitates its diffusion to the PEM but may lead to insufficient removal of water vapours formed at the cathode [3].

Pressure drop ( $\Delta p$ ) in a microchannel increases with the decrease in channel width and depth [21-23]. For constant flow rate:

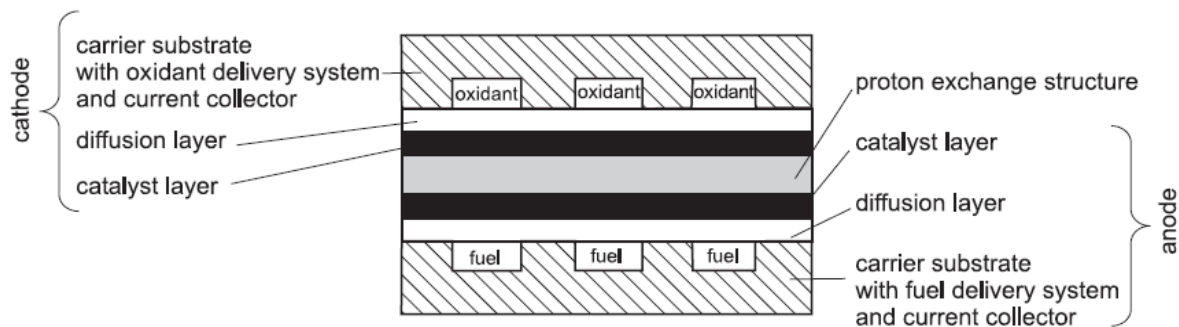
$$\Delta p \propto \mu S^{-3} \quad (3.4)$$

where  $S < 1$  for microchannels [2, 3]. A key reason for the pressure drop is the increased fluid friction in smaller microchannels. Higher pressure drop means that more pumping power is required to supply the reactants and remove the by-products [19]. However, increased pressure drop will improve the diffusion of the reactants to the reaction sites [2, 3]. Higher pressure drop will force the reactant to go directly into the diffusion layer, leading to better reactant permeability.

Cha et al. [19] conducted both computational and experimental study of the scaling effect of flow channels on the performance of  $\mu$ PEMFC. They varied the dimensions (width, depth and spacing) of their square-shaped microchannels from 5-500 $\mu$ m. The 3D computational model predicted a continual improvement in the power density and efficiency of the fuel cell as the channel dimension is reduced. The performance improvement is attributed to (i) the increase in gas flow velocity with reduction of channel dimensions (gas velocity  $\sim 1/\text{channel dimension}$ ), (ii) reduction of dead zones in the microchannels flow field, and (iii) deeper penetration of the convective flow in the porous gas diffusion layer due to higher flow resistance in smaller channels [19]. Experimental results of Cha et al. showed that the performance of the fuel cells improved as the microchannels size decreases from 500 $\mu$ m to 100 $\mu$ m. The fuel cell performance is at its peak for 100 $\mu$ m size but contrary to the computational model, performance decreases gradually with further decrease in channel size. The decrease in the performance of  $\mu$ PEMFCs with smaller microchannels ( $<100\mu$ m) is attributed to condensation of water at the cathode. Sufficient condensation of water will cause water flooding (or blocking) of cathode, which will limit the access of oxygen to reaction sites at the cathode [24]. The computational model used by Cha et al. did not account for two phase flow dynamics and thus could not predict the effect of water flooding on cell performance. The work done by Cha et al. clearly indicates that the flow field geometry has to be optimized for micro fuel cells in order to achieve optimum performance.

### 3.3 Micro proton exchange membrane fuel cell

Micro proton exchange membrane fuel cells ( $\mu$ PEMFC), along with micro direct methanol fuel cell ( $\mu$ DMFC), have been widely studied since they are considered most suitable for low temperature, low power portable applications [2-5,9,10]. The miniaturization of PEMFC and other fuel cells has been made possible by MEMS micromachining technologies [8]. The basic design and components of a typical  $\mu$ PEMFC, shown in Figure 3.1, are similar to conventional macro fuel cells (Figure 2.6).

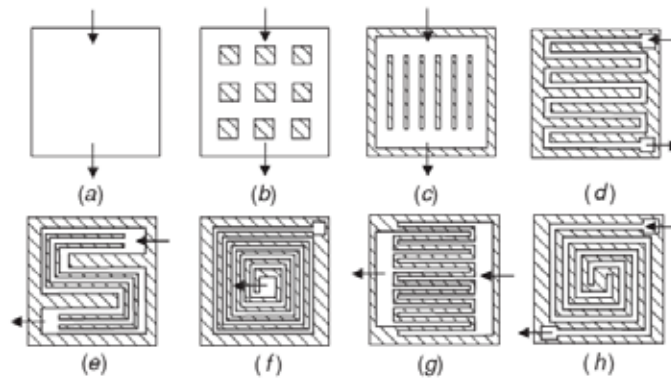


**Figure 3.1** Basic components of a typical  $\mu$ PEMFC. Reproduced from [3].

Considerable research in  $\mu$ PEMFC has yielded a range of different designs using a variety of different materials and microfabrication technologies [4]. In the following subsections, different components of  $\mu$ PEMFC are explained.

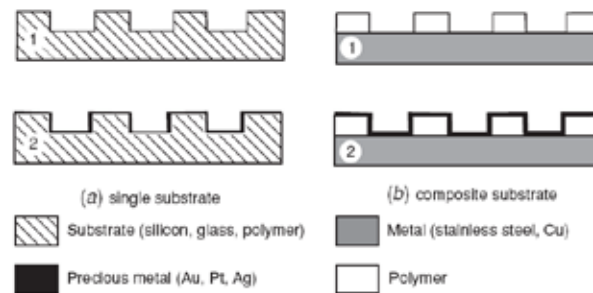
#### 3.3.1 Micro flow plates

$\mu$ PEMFC flow plates are used to deliver fuel and oxidant to the reaction sites. The micro flow plates are also meant to collect current and are either made of or are coated with a conductive material. As discussed in Section 3.2, the design of microchannels of flow plates is an important issue for micro fuel cells. Different designs of the flow field have been reported in the literature and have been summarized by Nguyen et al. [3] in Figure 3.2. In general, serpentine and spiral designs show higher performance compared to direct or parallel designs [3]. This may be due to better fuel distribution, better removal of water, and/or better utilization of the active membrane area [3].



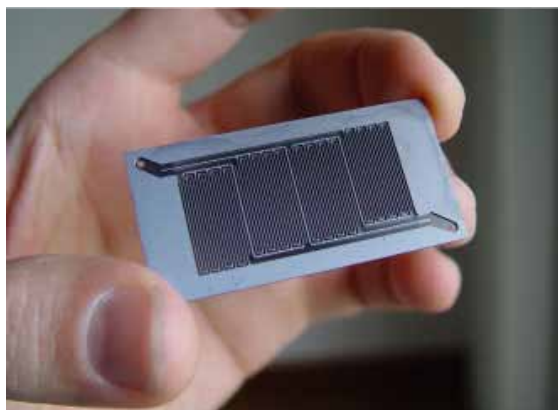
**Figure 3.2** Typical fuel delivery designs: (a) direct supply, (b) with distribution pillars, (c) parallel microchannels, (d) serpentine microchannel, (e) parallel/serpentine microchannel, (f) spiral microchannel, (g) interdigitated microchannel, (h) spiral/interdigitated microchannel.

Reproduced from [3].

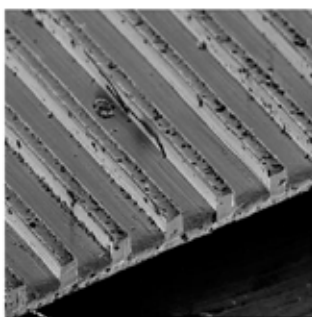


**Figure 3.3** Fabrication steps of flow plates: (a) bulk micromachining on a single substrate, (b) micromachining of a composite substrate. Reproduced from [3].

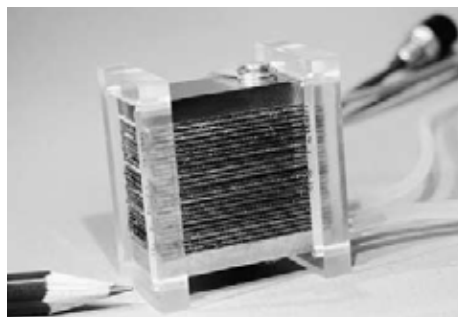
Different materials have been used to fabricate the micro flow plates [4]. The flow plate's substrate is formed of a single material or a combination of materials, as shown in Figure 3.3. Silicon (Si) has been a popular material choice for flow plates [10, 25-37] because of the well established Si based microfabrication technologies [8]. Another advantage of Si based micro fuel cells is that the fuel cell can be integrated with other electronic devices on the same chip. Basic Si micromachining processes like anisotropic wet etching, reactive ion etching (RIE) and deep reactive ion etching (DRIE) can be used to fabricate microchannel structures in the Si substrate. Thin film deposition technologies [8] like radio-frequency (RF) or magnetron sputtering, e-beam evaporation, physical vapour deposition (PVD), chemical vapour deposition (CVD), and pulsed laser deposition (PLD) are used to deposit current collector (Ag, Cu, Au or other metal) on the microchannels. The microchannels in the flow plate and the current collector layer are patterned using photolithography process [8].



**Figure 3.4** Flow field formed in silicon substrate using deep reactive ion etching (RIE) process. Reproduced from [2].



(a)



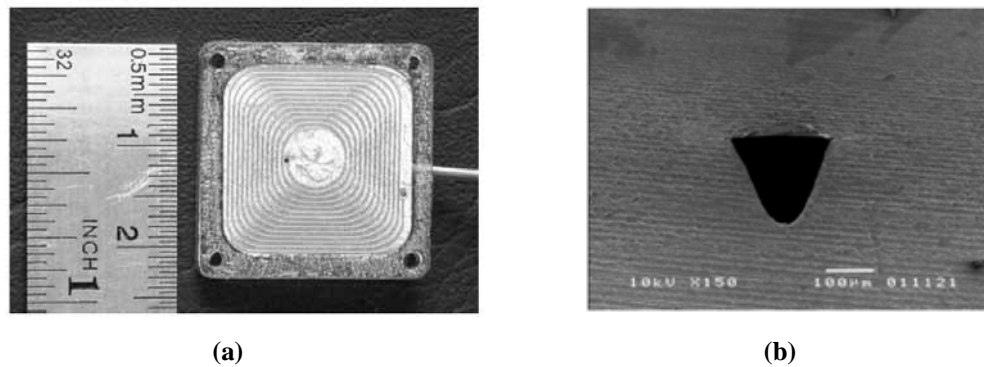
(b)

**Figure 3.5** (a) SEM image of a metal foil with micro channels of  $150 \times 150 \mu\text{m}^2$  cross-sectional area. (b) 25 cell stack with micromachined metal flow fields. Reproduced from [39].

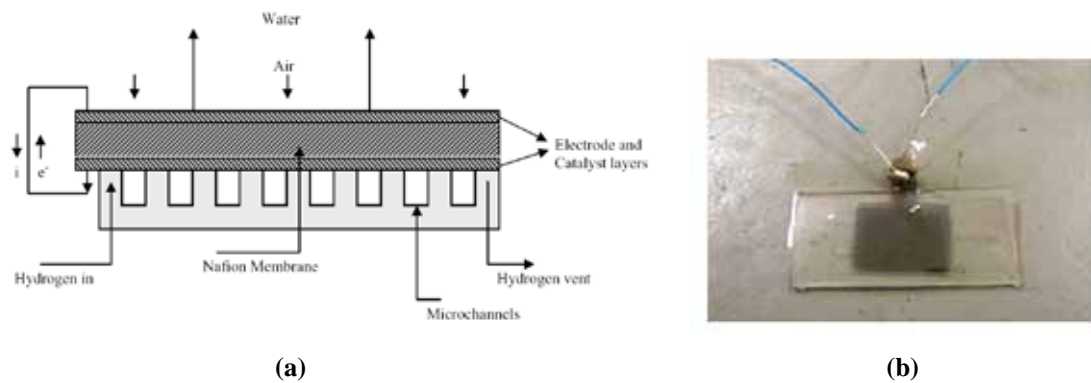
Silicon substrate is relatively fragile, which makes it difficult to compress the fuel cell for tight seals and low contact resistance between flow plates and MEA. More compressible materials like metal or alloy foils, polymers and printed circuit board (PCB) have also been used for fabricating micro flow plates [4]. Stainless steel foils are commercially available and can be micromachined by etching, laser machining and punching [3, 38]. Muller et al. fabricated micro flow plates with stainless steel [39]. They demonstrated a 25 cell stack, where nickel coated brass is the material used for the micro flow plates [39]. Hahn et al. [38] used stainless steel foil laminated onto polyimide film as the substrate. The microchannels are patterned in the polyimide by RIE and gold (Au) is deposited by electroplating and patterned to form the current collector [38]. Hsieh et



al. have proposed copper (Cu) flow plates, which are formed using UV-LIGA process [40].

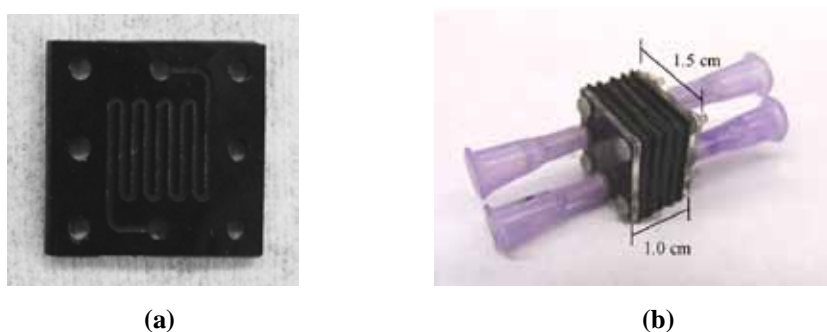


**Figure 3.6** (a) Image of the spiral shaped flow field fabricated in PMMA substrate by laser ablation, and coated with Au current collector (b) SEM cross-sectional view of Gaussian shaped microchannel fabricated in PMMA. Reproduced from [41].



**Figure 3.7** (a) Schematic cross-section and (b) image of the PDMS based  $\mu$ PEMFC presented in [42]. Reproduced from [42].

Polymers like polymethylmethacrylate (PMMA) and polydimethylsiloxane (PDMS) have also been used for flow plates [4]. Polymeric micromachining technologies such as RIE, hot embossing, soft lithography, laser ablation and molding are readily available [3]. Chan et al. [41] fabricated spiral shaped flow field in PMMA. The microchannels were fabricated using laser ablation and each channel had a Gaussian shaped cross section. The smooth Gaussian shape ensures that the gold current collector layer will cover all sides of the channel, which will eventually reduce internal resistance [41]. Shah et al. [42] fabricated the flow plates of their air breathing  $\mu$ PEMFC with PDMS. PDMS flow plates are fabricated using molding and are inexpensive compared to Si.



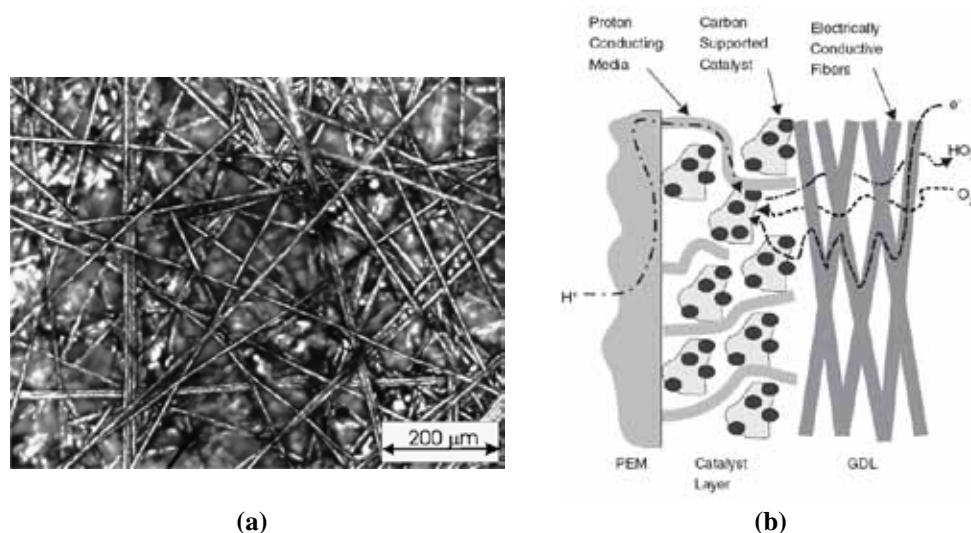
**Figure 3.8** (a) Carbon bipolar plate fabricated by C-MEMS technology. (b) Assembled three cell stack with carbon bipolar plates. Reproduced from [46].

PCB technology has also been employed in fabrication of micro fuel cells [43-45]. O'Hayre et al. [43] used PCB as the substrate for fabrication of arrays of planar micro fuel cells. The planar micro fuel cells arrays demand complex insulator-collector layouts, which are possible by PCB technologies. The microchannels are formed by etching the Cu layer of PCB. The underlying insulating substrate of Flame Retardant 4 (FR4) material was etched to form channels for delivery of fuel to the Cu microchannels. Lin et al. [46] fabricated carbon flow plates for their micro fuel cell and stacked three fuel cells together. Their carbon flow plates were fabricated using carbon-microelectromechanical systems (C-MEMS) technology [46], in which an organic material is machined or patterned into the desired structure and then pyrolysis process converts the whole structure into carbon.

### 3.3.2 Diffusion layer

From Figure 3.1, it can be seen that in case of the absence of diffusion layer, the catalyst layer area immediately below the ribs (between the microchannels) of the flow plates will not have access to the reactant gas, resulting in large number of unused reaction sites. This problem is solved by incorporating diffusion layers in the fuel cell design. The diffusion layer is also referred as gas diffusion layer (GDL). The purpose of the diffusion layer is to transport and evenly distribute fuel or oxidant over the catalyst layer. The diffusion layer also provides electrical connection between catalyst layer and flow plate and can help in removing product water. Diffusion layers are usually made of electrically conductive porous materials like carbon paper, carbon cloth or metal mesh [3, 39]. Carbon paper has been a popular choice for diffusion layer in micro fuel cells [3] and it can be modified to improve its property. Carbon paper can be treated with

graphite or filled with conductive powder like carbon black to further improve its conductivity. Carbon paper can also be treated with hydrophobic material like polytetrafluoroethylene (PTFE) which aids in removing water from its pores.



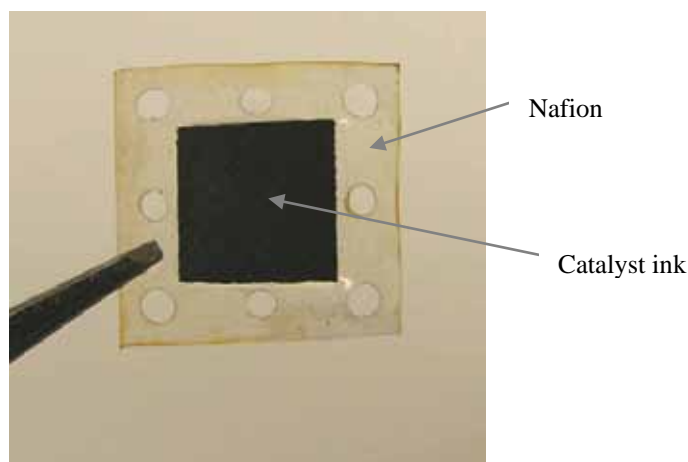
**Figure 3.9** (a) SEM image of carbon paper GDL (b) schematic diagram illustrating the interface between GDL, catalyst layer and electrolyte. Reproduced from [47].

A disadvantage of diffusion layers is that they prevent the convective transport of reactants to the reaction sites [39]. The supply to the reaction sites with diffusion is less than what it could be with convective dominated transport without a diffusion layer [39]. The use of diffusion layers in micro fuel cells means that one more component has to be heterogeneously integrated with the rest of the micro fuel cell components. Most micro fuel cell designs avoid this integration issue by replacing the diffusion layer with microstructures like porous silicon [26] or micropillars incorporated in the flow field [35].

### 3.3.3 Catalyst layer

Platinum (Pt) or Pt based alloy like Pt-Ru are used as the catalyst in  $\mu$ PEMFCs. Catalyst thin films can be deposited using deposition technologies like sputtering or e-beam evaporation. To increase the three phase contact area and minimize the costs associated with deposited thin films of Pt, Pt or Pt alloy nanoparticles supported on conductive carbon black or fine Pt powder (Pt black) are used to form the catalyst layer. Carbon supported Pt nanoparticles (Pt/C) or Pt black is added to a solution of de-ionized water

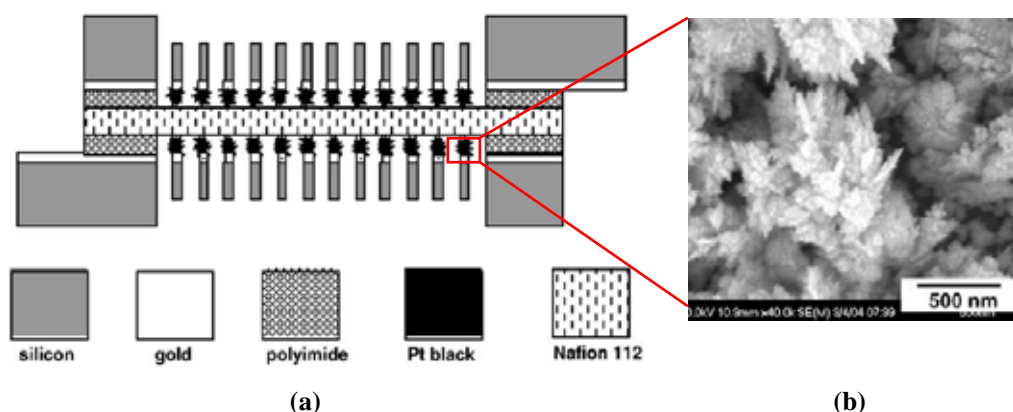
(DIW), a solvent, and dilute Nafion solution (ca. 5%) to form slurry termed as catalyst ink. In addition to carbon black, recently, carbon nano tubes (CNTs) have also been proposed as the support for the catalysts [48, 49].



**Figure 3.10** Membrane electrode assembly (MEA) formed by brushing catalyst ink on both sides of Nafion membrane. Reproduced from [46].

There are four different approaches by which the catalyst layer can be integrated into the micro fuel cell design:

1. The standard approach, which is also seen in most macro PEMFCs, is to apply the Pt based catalyst ink onto the PEM with a spray or brush [3,6].
2. The catalyst ink can also be applied to the GDLs (carbon paper) and the PEM is stacked between the two GDLs afterwards [6].
3. Thin film of catalyst is deposited on the PEM using sputtering or e-beam evaporation [3, 42]. This approach has been applied in the fuel cell in Figure 3.7.
4. A popular approach in fabrication of  $\mu$ PEMFCs is to deposit Pt thin film directly onto the flow plate (Figure 3.11). This approach forgoes the use of a diffusion layer as flow plates usually have microstructures incorporated in their design. Thus, the flow plate, diffusion layer and the catalyst layer are integrated into a single component.



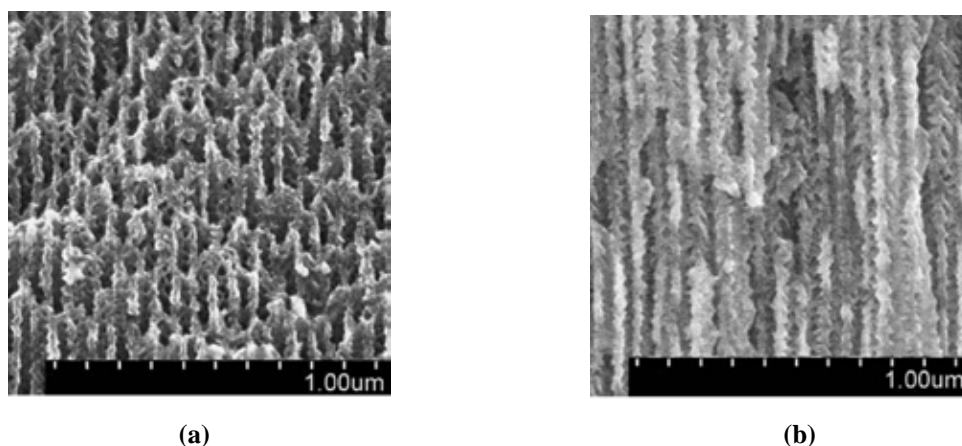
**Figure 3.11** (a) Schematic cross section view of a micro fuel cell without a standard diffusion layer. (b) SEM image of electrodeposited Pt black. Reproduced from [28].

### 3.3.4 Electrolyte

As discussed in Section 2.4.2, PEM is an ion conducting sulphonated fluoropolymer in which  $H^+$  ions (protons) are mobile. Nafion by DuPont has been the PEM of choice for most  $\mu$ PEMFCs presented in literature. In the fabrication of PEM, the starting material is a polymer - polyethylene. The hydrogen in polyethylene is replaced by fluorine through a process known as perfluorination to form polytetrafluoroethylene (PTFE). PTFE, commercially available as Teflon, is durable, resistant to chemical attack and most importantly hydrophobic. To make PTFE into an electrolyte, the basic PTFE polymer is “sulphonated” i.e. a side chain is added, ending with sulphonic acid  $HSO_3$ . The  $HSO_3$  group side chains tend to cluster together in the overall material. Sulphonic acid is highly hydrophilic, thus in Nafion there are hydrophilic regions within a generally hydrophobic material (PTFE). The hydrophilic regions in Nafion can absorb a large quantity of water, which can increase the weight of the membranes by as much as 50% [6]. Within these hydrated regions, the  $H^+$  ions are weakly bonded to  $SO_3^-$  ions and can easily move. Thus, the hydrated regions of Nafion act as dilute acid integrated within a tough hydrophobic material. The proton conductivity of Nafion and other PEM increases as hydration level is increased. In fact, presence of water is essential for function of PEM. As the water contents of PEM falls, the conductivity falls as well.

Since the proton conductivity in Nafion depends on its water content, it cannot be used at higher temperatures, such as  $120^\circ\text{C}$ . Moreover, Nafion expands or shrinks depending on its hydration level, and its mechanical strength changes with temperature and humidity. Nafion is not readily integrated with standard microfabrication techniques

used in making micro-fuel cells [3, 30]. Nafion cannot be easily patterned using photolithography. Zhang et al. [50, 51] used nanoimprint technology to pattern Nafion. They fabricated a grid of dots (micro-convex) in the Nafion membrane to act as GDL and subsequently improve the three phase contact. Bonding Nafion to silicon is often problematic in working fuel cell conditions, due to its volumetric changes with changes in hydration level. Alternates to Nafion (and similar PEMs) have been proposed by some research groups [30, 32, 52- 54]. Gold et al. [30] used nanoporous silicon membrane loaded with sulphuric acid as the proton conductor for their micro fuel cell. The nanoporous silicon is formed by the anodic etching of silicon in hydrofluoric acid (HF). Porous silicon was also used by Pichonat et al. for their electrolyte. However, they loaded their porous silicon with Nafion solution instead of an acid (Figure 3.12) [32, 55]. Stanley et al. [54] used porous glass fibre substrate that is loaded with Nafion solution to form the PEM. Liu et al. [52] used the effect that overlapping electric double layers (EDLs) in a nanochannel will enhance the conduction of protons. They fabricated nanochannels in glass substrate and derivatized their inner walls with  $-\text{SO}_3\text{H}$  group to form their electrolyte [52]. Kanamura et al. fabricated the PEM by first fabricating a macroporous silica membrane and then, filling the pores with a proton conducting gel polymer [53].



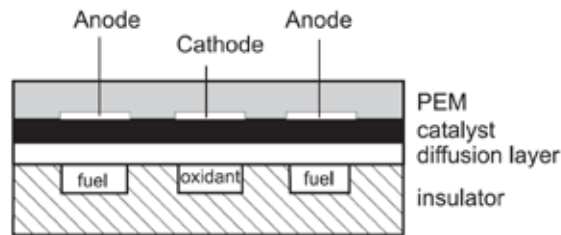
**Figure 3.12** (a) Field Emission Scanning Electron Microscope (FESEM) cross-section views of porous silicon. (b) FESEM cross-section views of porous silicon filled with Nafion.

Reproduced from [32].

### 3.3.5 Stack vs. planar design

There are two configurations for the  $\mu\text{PEMFC}$ : stack design and planar design. The stack design (also referred to in the literature as bipolar or bilayer design) has separate

fuel and oxidant flow plates and the PEM is sandwiched between them. Stack design is the most common configuration and is depicted in Figure 3.1. In planar design, the fuel and oxidant channels are fabricated on a common substrate, as shown in Figure 3.13. The planar configuration is a monolithic design where anode and cathode are present side-by-side. Compared to stack design, planar design is easy to implement since it requires less hybrid integration i.e. there are less separately fabricated components which need to be assembled together.



**Figure 3.13** Planar design of micro fuel cell. Reproduced from [3].

Meyers et al. [10] studied the tradeoffs between stack and planar design. Their mathematical model and practical experiments showed that the performance of the planar fuel cell is inherently limited and lags behind that of the stack design. Since cathode and anode share a common substrate, the planar fuel cell requires a larger surface area compared to a bipolar design to provide the same performance. In planar design, metal lines have to be used as current collectors for the electrodes. This will induce non-uniform current distribution over the electrodes since some parts of the electrode are more accessible for current than others. Though planar fuel cell design seems simple, however, it requires complex fuel and oxidant delivery schemes since flow channels are on the same plane and cannot intersect. For detailed comparison between stack and planar design, the reader is referred to the work of Meyers et al. [10].

### 3.3.6 Performance

If we consider recent  $\mu$ PEMFCs, the literature reports performance that range from  $90 \mu\text{W}/\text{cm}^2$  [26] up to  $700\text{mW}/\text{cm}^2$  [43]. Table 3.1 summarizes the performance of  $\mu$ PEMFCs. Unless mentioned otherwise, the power densities are reported for the fuel cells operating at room temperature ( $20\text{--}25^\circ\text{C}$ ).

**Table 3.1** Design features and performance of  $\mu$ PEMFCs

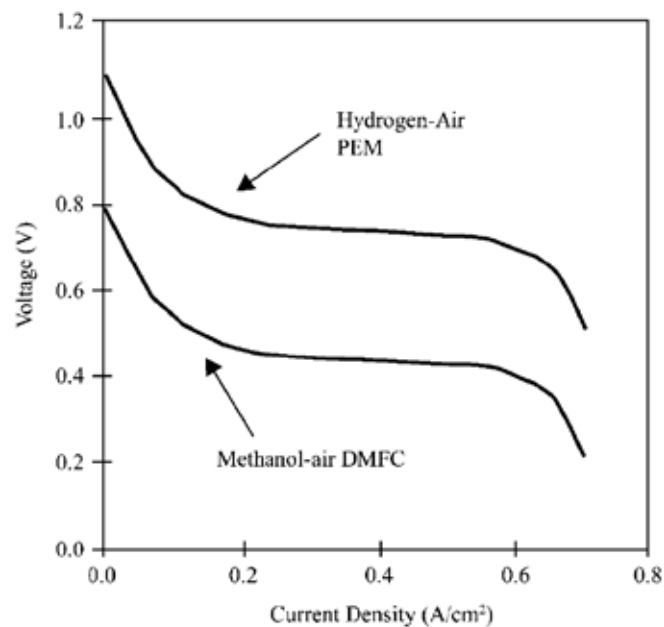
Reference	Substrate	Flow design	PEM	Catalyst form	Oxidant	Maximum power density (mW/cm <sup>2</sup> )	Comments
Chan et al. [41]	PMMA	Spiral	Nafion	Catalyst ink	Forced O <sub>2</sub>	315	82mW/cm <sup>2</sup> with forced air; Figure 3.6
Hahn et al. [38]	Steel/polymer	Parallel	Nafion	Not specified	Air breathing	120	
Hsieh et al. [56]	PMMA	Parallel/serpentine	Nafion	Sputtered thin film on Nafion	Air breathing	25	
Hsieh et al. [40]	Copper sheet	Serpentine	Not specified	Not specified	Forced Air	ca.40	60mW/cm <sup>2</sup> at 50°C
Lee et al. [25]	Silicon	Pillars	Nafion	Catalyst ink	Not specified	42	Planar design; 4 cells connected in series
Lin et al. [46]	Carbon	Serpentine	Nafion	Catalyst ink	Forced air	0.62	1.18 mW/cm <sup>2</sup> for 3 cell stack; Figure 3.8
Min et. al [26]	Silicon/glass	Direct	Flemion	Pt film on porous SiO <sub>2</sub> GDL	Air breathing	0.09	
Muller et al. [39]	Metal foil	Parallel	PRIMEA® by GORE™	PRIMEA® by GORE™	Forced O <sub>2</sub>	50	250mW/cm <sup>2</sup> for 5 cell stack; Figure 3.5
O'Hayre et al. [43]	PCB	Parallel	Nafion	Catalyst ink	Forced O <sub>2</sub>	>700	Fuel cell dimensions are comparable to a 3.5 inch floppy disk
Pichonat et al. [32]	Silicon	Not specified	Nafion filled porous silicon	Catalyst ink	Air breathing	18	Figure 3.12
Shah et al. [42]	PDMS	Parallel	Nafion	Pt thin film deposited on Nafion	Air breathing	0.28	At 60°C; Figure 3.7
Stanley et al. [54]	PDMS	Not specified	Nafion loaded glass fibre	Catalyst ink	Forced air	3.2	At 30°C
Xiao et al. [35]	Silicon/glass	Pillars	Nafion	Pt deposited on flow field pillars	Forced O <sub>2</sub>	13.7	
Yeom et al. [28]	Silicon	Not specified	Nafion	Electrodeposited Pt black	Forced O <sub>2</sub>	35	Figure 3.11
Yu et al. [27]	Silicon	Serpentine	Nafion	Catalyst ink	Forced O <sub>2</sub>	194.3	



### 3.4 Micro direct methanol fuel cell

A major problem faced by the current  $\mu$ PEMFC technology is the unavailability of safe, reliable and efficient means of storing hydrogen in portable devices. There is also a lack of infrastructure for distribution of hydrogen. Unless the problem of hydrogen storage is solved, commercialization of  $\mu$ PEMFC technology will be limited. On the other hand, methanol is in liquid form at ambient temperatures, has high energy density compared to hydrogen, and is easier to store in a portable device. This makes micro direct methanol fuel cell ( $\mu$ DMFC) the most viable candidate for portable applications [2,5,17].

$\mu$ DMFC and  $\mu$ PEMFC share very similar design and components: both use PEM as the electrolyte and Pt based catalysts. The stack and planar design of  $\mu$ PEMFCs presented in Figure 3.1 and Figure 3.13, respectively, are also true for  $\mu$ DMFCs, along with the flow field designs of Figure 3.2. Similar to  $\mu$ PEMFCs,  $\mu$ DMFCs have been implemented using silicon [50, 57-66], polymers [67], or stainless steel foils [68]. In fact, some research groups [28, 35] have tested their fuel cells for both hydrogen and methanol fuels. They reported lower performance for methanol compared to hydrogen (see Figure 3.14), despite the fact that methanol has higher energy density (see Figure 1.1).



**Figure 3.14** Example of fuel cell polarization curves illustrating the difference in performance between  $\mu$ PEMFC and  $\mu$ DMFC operating under nominally equivalent conditions (temperature, air and fuel flow). Reproduced from [2].

One reason for the lower performance of  $\mu$ DMFC is the sluggish reaction kinetics of methanol oxidation at the anode (See Table 2.1 for anode reaction). The oxidation of methanol, which results in 6 electrons per molecule, is a complex process and it occurs in stages [6]. Suitable catalysts are needed to promote the methanol oxidation. Pt/Ru bimetal catalyst provides better performance compared to Pt [17]. The second major problem which lowers  $\mu$ DMFC performance is methanol crossover. The PEM (Nafion) readily absorbs methanol, which mixes with water in the membrane and reaches the cathode [6]. At the cathode, the Pt catalyst will oxidize methanol, resulting in a mix potential and drastic reduction of cathode voltage [6, 17]. This can be considered as a sort of “chemical short circuit” [17]. A standard approach to minimize the crossover is to lower the concentration of methanol by diluting the fuel feed with water [6]. Another standard approach is to make the anode catalyst as active as possible, so that most of the methanol is consumed at the anode and does not permeate to the membrane. It has also been demonstrated that methanol crossover reduces at higher operating currents [6]. Thus, it is beneficial to operate  $\mu$ DMFC near its peak power.

### **3.5 Micro direct glucose fuel cell**

Glucose is a promising fuel for miniature fuel cells. It has high energy content (if it can be completely oxidized), abundant in nature, easy to extract or produce, simple to store due to its nonflammable, nontoxic and nonvolatile nature, renewable, and environmentally friendly [69]. Glucose is also ubiquitously available in body fluids, which makes glucose the most considered fuel for implantable fuel cell systems [18]. Glucose consuming fuel cells can be categorized into three types according to the type of catalyst used to promote the electrode reactions: enzymatic, microbial and abiotically catalyzed glucose fuel cells. Enzymatic and microbial glucose fuel cells are collectively referred to as biofuel cells and have been discussed in Section 2.4.7. Abiotically catalyzed glucose fuel cells make use of non-biological catalysts like noble metals to enable the electrode reactions. In this work, the term micro direct glucose fuel cell ( $\mu$ DGFC) will be exclusively used for miniature abiotically catalyzed glucose fuel cells.

A key application of glucose based fuel cells is to power medical implants because of the relatively constant availability of glucose and oxygen in body fluids (like blood). Though considerable research is being conducted on biofuel cells [7, 13, 14], the current biofuel cells are not suitable for long term medical implants. Enzymatic biofuel

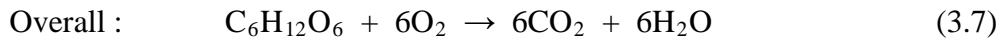
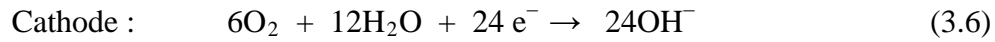
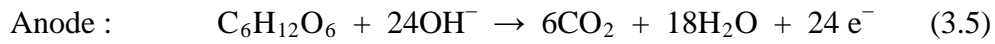
cells suffer from limited lifetime of enzymatic biocatalysts [18,70]. While, microbial fuel cells are not considered for implantation due to the infective nature of most known microorganisms [13, 14, 18].  $\mu$ DGFC intended for long term medical implants, use inorganic catalysts like noble metals and activated carbon [18], which are sterilizable and biocompatible. The inorganic catalyst also exhibit long term stability and in theory,  $\mu$ DGFC can operate in in-vivo applications for indefinite period of time, as long as the reactants are available [18]. The concept of abiotically catalyzed glucose fuel cells was reported for the first time in the late 1960s [18] and the first truly implantable glucose fuel cell were developed by early 1970s [18]. However, with the introduction of lithium-iodine batteries in the mid 1970 [18] as power source for medical implants like pace makers, no further developments were made in glucose fuel cells. In the last decade, the advancement made in MEMS based micro sensors and actuators, and their possible use in medicine has rekindled the interest in glucose based fuel cells. In near future,  $\mu$ DGFCs will power autonomous, implanted, medical sensor–transmitter devices. These medical sensors would provide information for a few weeks on, for example, the local temperature of a site, indicative of local inflammation; or pressure, indicative of fluid blockage; or deviation from the normal concentration of a chemical, specific to a disease.  $\mu$ DGFCs use is not limited to medical implants. Glucose based sensors can also be used to operate low power autonomous integrated sensor and communication microsystems. For instance,  $\mu$ DGFC running on tree sap can be used to power a remote micro sensor.



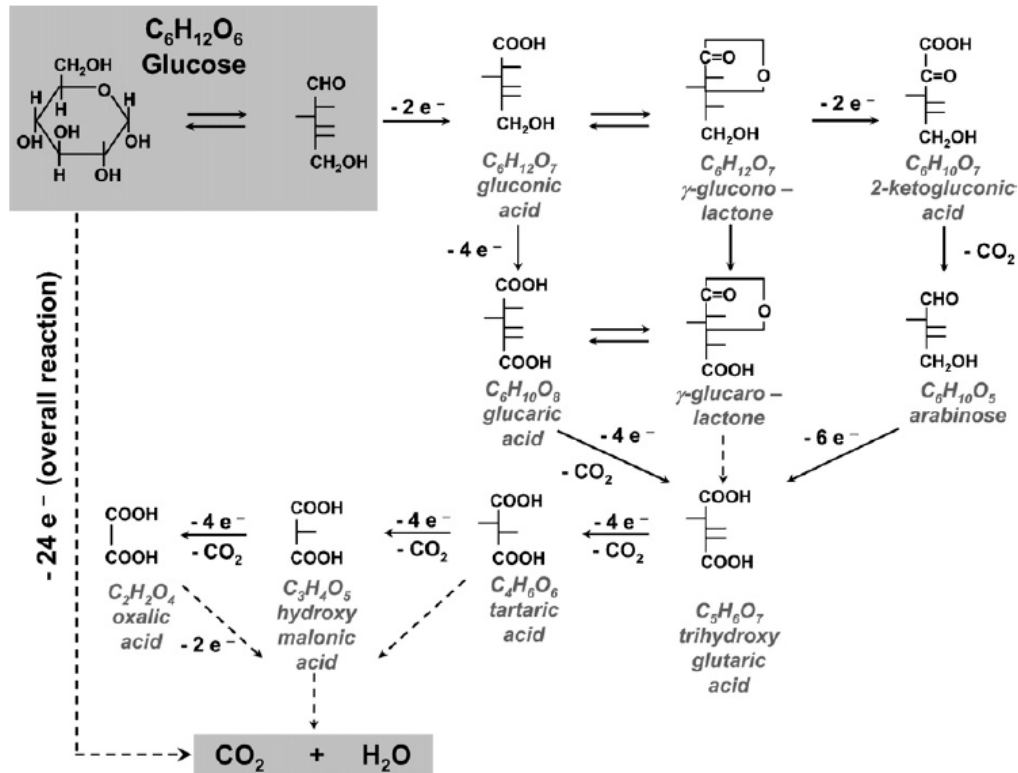
**Figure 3.15** A simple sap harvesting device is inserted into a sugar maple tree. The sap dripping from the device is clearly visible. The device is meant to supply fuel to a  $\mu$ DGFC. Reproduced from [71].

### 3.5.1 Operational principle

Theoretically, glucose can be completely oxidized into carbon dioxide and water, releasing 24 electrons for every glucose molecule. In case of complete oxidation, the reactions occurring at each electrode will be given as:



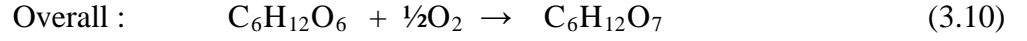
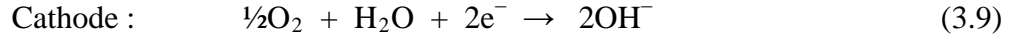
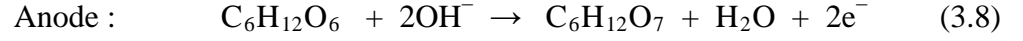
The complete oxidation of glucose is a complex process which occurs in several stages. Figure 3.16 summarizes the tentative oxidation pathways and intermediate reaction products of glucose oxidation.



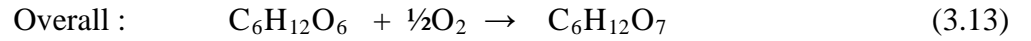
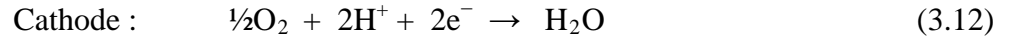
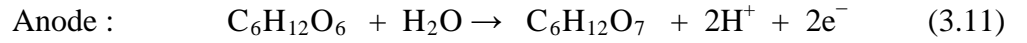
**Figure 3.16** Tentative oxidation pathways and intermediate reaction products of glucose oxidation. Reproduced from [18].

In practice, it is difficult to realize complete oxidation of the glucose molecule and transfer the 24 electrons [18]. In case of Pt electrodes, Rao et al. [72] identified gluconic acid ( $\text{C}_6\text{H}_{12}\text{O}_7$ ) as the only reaction product of glucose oxidation in a neutral buffer solution. Further oxidation of gluconic acid is possible but it will occur at a slow

reaction rate and does not significantly contribute to the overall electron yield [18]. The oxidation of glucose into gluconic acid only yields two electrons. The corresponding electrode reactions for hydroxyl ion conducting electrolyte are:



In case of proton conducting (acidic) electrolyte, the electrode reactions of the DGFC where gluconic acid is the final product are given as:



Ernst et al. used mass spectroscopy to identify glucono lactone as the product of glucose oxidation [18]. Glucono lactone, goes through hydrolysis to form gluconic acid. Kokoh et al. [73] studied the electro-oxidation of glucose with Pt, Au and adatom (Pb, Ti, Bi) modified Pt electrodes in neutral buffer solution with  $50.06 \times 10^{-3}$  mol/L of glucose. The reaction products were analyzed using chromatographic techniques. It was found that irrespective of the reaction conditions, gluconic acid was the main reaction product. However, in addition to gluconic acid, glucuronic, oxalic, glyoxylic and tartaric acid were also detected along with traces of glycolic and formic acid. Lerner et al. [74] studied the number of electrons transferred per glucose molecule for different catalysts. According to their study, for platinised Pt electrodes between 4 to 20 electrons are transferred, while for Raney-type Pt catalyst the average electron yield is 17. The variations in the published result on glucose oxidation products and electron yield can be linked to analytical limitations [18]. Also, in addition to the catalyst material, the pH and ionic strength of the electrolyte will also influence the reaction mechanism of glucose oxidation [18].

### 3.5.2 Catalyst materials

The catalysts for glucose oxidation and oxygen reduction are very critical part of  $\mu$ DGFCs. In situations where reactants (glucose and oxygen) are inseparable, like in implantable or single compartment fuel cells, it is desirous to have catalysts with high

reactant specificity to minimize fuel crossover losses. Catalysts for selective reduction of oxygen in the presence of glucose are available e.g. silver (Ag) and activated carbon [75]. However, no non-biological catalyst is available which can selectively oxidize glucose in the presence of oxygen. Early work on DGFCs generally used Pt as the catalyst for glucose oxidation [18]. However, in recent work other noble metals and alloys have been employed e.g. platinum-ruthenium alloys, rhodium and iridium. The catalyst metals are usually employed as particles supported on activated carbon (carbon powder).

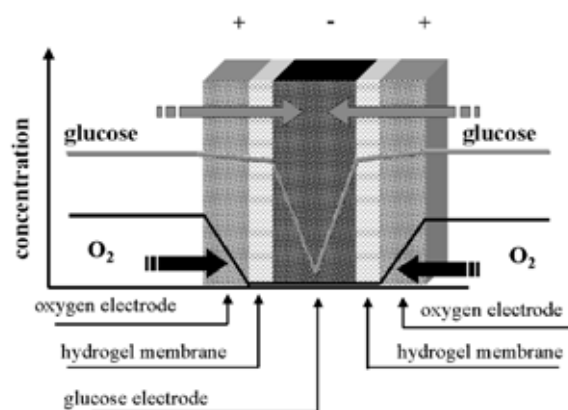
Kerzenmacher et al. [75] used platinum- bismuth (Pt-Bi) alloy supported on the activated carbon as their anode catalyst. This catalyst is commercially available and specifically developed to oxidize glucose into gluconic acid. In the mid 1970s, Gebhardt et al. [76] used a special Raney alloy - Pt with ferrous metal like nickel (Ni) - for glucose oxidation. The non-noble metal is later extracted from the alloy by anodic dissolution and a porous catalyst with improved activity is obtained. They reported further improvement in the catalyst by adding tungsten (W) or tantalum (Ta). The alloy catalyst was able to transfer 17 of the 24 electrons available in a glucose molecule by gradual oxidation which takes several hours. Kerzenmacher et al. [77] followed a process similar to the work in [76]. They electroplated zinc (Zn) on top of Pt foil and annealed at 200°C to form Pt-Zn alloy. The Zn is later dissolved in sulphuric acid to leave behind self supporting porous Pt electrodes.

Wang et al. [78] presented a nanoporous Pt-Pd electrode for glucose oxidation in their glucose sensor. Tominaga et al. [79] developed carbon electrodes modified by gold nano-particles as the catalyst for oxidation of glucose. However, Aoun et al. [80] demonstrated that Pt nano particles modified carbon electrodes have better performance compared to the carbon electrodes with gold nano particles. Recently, Cui et al. [81] reported Pt-Pd alloy nanoparticles deposited on CNTs as the catalyst for glucose oxidation.

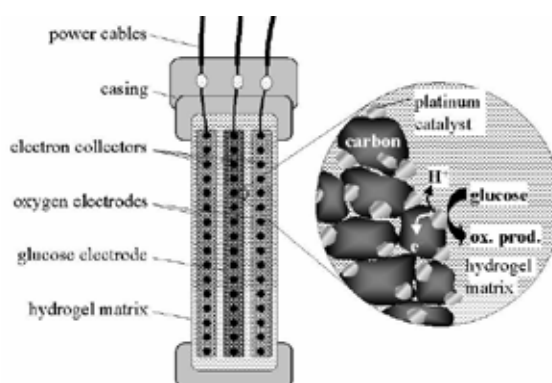
### **3.5.3 Design**

A  $\mu$ DGFC can have a design similar to the one presented in Figure 3.1, in which the fuel and oxidant delivery plates are separated by the electrolyte which is sandwiched between them. However, such a configuration is not applicable to situations in which glucose and oxygen are inseparable e.g. in vivo operation. Since the reactants are inseparable, losses associated with reactant crossover can be significant in implantable and one-

compartment designs. The reason is that the Pt and its alloys (anode catalysts) are not only good catalysts for glucose oxidation but also have higher oxygen reduction performance (compared to Ag or activated carbon). Thus, on the surface of Pt electrode both oxygen reduction and glucose oxidation will occur if the reactants share the same surrounding. The anode will thus attain a mixed potential somewhere between the potentials of glucose oxidation and oxygen reduction. Due to the mixed potential, the overall terminal voltage of the fuel cell will be drastically reduced [6, 70]. Different design approaches have been implemented to minimize the access of oxygen to the anode [18].



**Figure 3.17** Operational principle of implantable  $\mu$ DGFC reported by Stetten et al. See text for explanation. Reproduced from [82].

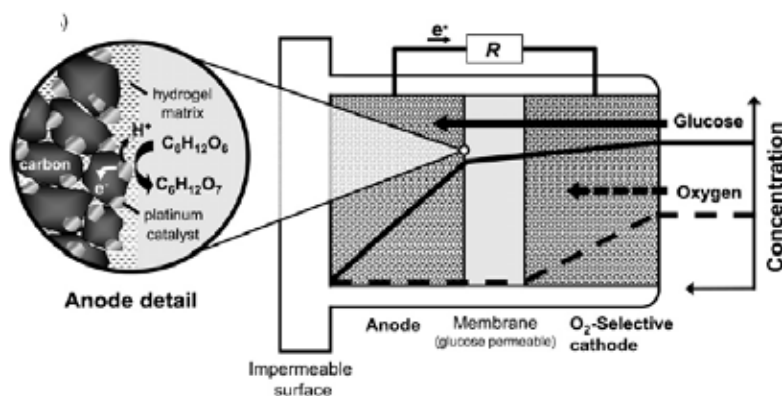


**Figure 3.18** Schematic cross section of the implantable  $\mu$ DGFC presented in [82]. Reproduced from [82].

The implantable  $\mu$ DGFC presented by Stetten et al. [75, 82] features a special arrangement of the electrodes, originally proposed by Rao et al. [72] in the mid 1970s, to prevent oxygen from reaching the anode. The operational principle and schematic diagram of their implantable  $\mu$ DGFC are presented in Figure 3.17 and 3.18 respectively.

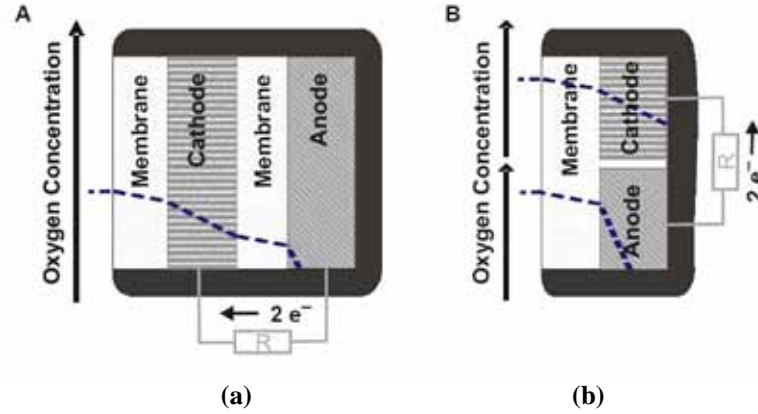
The design features a non-selective anode (Pt or Pt-Bi particles supported on carbon) which is sandwiched between two oxygen selective cathodes (activated carbon). Both anode and cathode are permeable to the reactant mixture (glucose, oxygen and electrolyte), which can diffuse from the surrounding environment. During operation, the oxygen is first selectively reduced at the outer cathodes, resulting in its removal from the reactant mixture. A predominantly anoxic region is formed at the anode where the glucose is oxidized by non-selective catalyst. This design demands that the oxygen be present in the reactant mixture in much lower equivalent concentrations than glucose. This condition is fulfilled in body fluids [72, 18]. The electrodes are fabricated from electrically conductive catalyst particles which are embedded in polymer hydrogel binder. The hydrogel is permeable to the reactant mixture. A hydrogel membrane is also used to electrically insulate the anode from the cathode.

Kerzenmacher et al. have also presented a variation of the above mention design concept in [70] and [75]. In this variant, the anode is sandwiched between a cathode and an impermeable surface. The reactants have access to the fuel cells from only one side as shown in Figure 3.19. The benefit of this design is that the fuel cell can be easily mounted on the surface of the medical implant [70]. Kerzenmacher et al. also studied the side by side configuration of electrodes in  $\mu$ DGFCs (Figure 3.20(b)) [83]. They used Pt-Zn anode for glucose oxidation and studied its tolerance to oxygen. The side by side configuration does not out perform their stack electrodes design. However, it does demonstrate that an oxygen consuming layer in front of the anode is not essential to operate an implantable  $\mu$ DGFC.

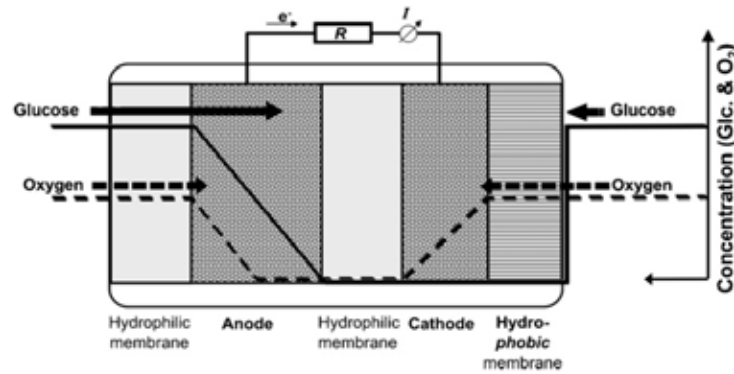


**Figure 3.19** Operation principal of surface mountable  $\mu$ DGFC. Reproduced from [75].





**Figure 3.20**  $\mu$ DGFCs designs: (a) Stacked assembly suggested in [70, 72, 75]; (b) Single layer layout with anode and cathode placed side by side. Reproduced from [83].

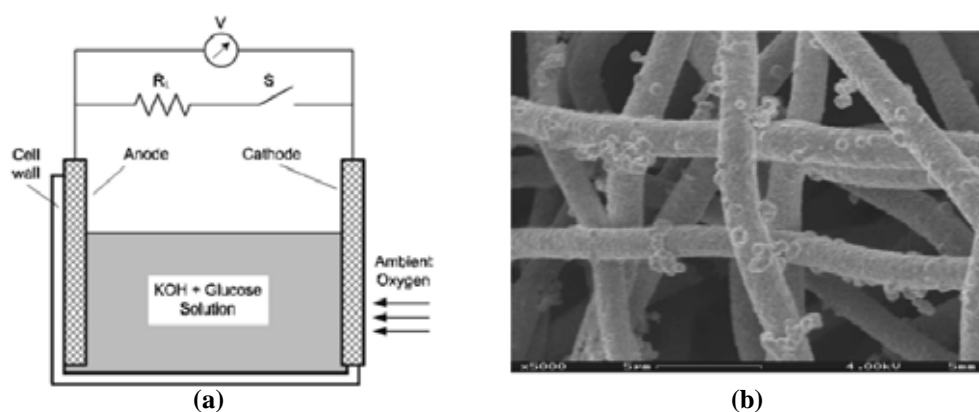


**Figure 3.21**  $\mu$ DGFC with hydrophobic cathode membrane. Reproduced from [18].

Another design concept for reactant separation in implantable  $\mu$ DGFCs is shown in Figure 3.21 [18, 84, 85]. Similar to the designs discussed earlier, the electrodes are permeable to both glucose and oxygen. However, this design utilizes non-selective catalyst for cathode as well. The cathode is protected from the entry of glucose (and rest of body fluids) by a hydrophobic membrane, which is only permeable to gaseous oxygen. Between the anode and cathode, a hydrophilic ion conducting membrane is used for electrical insulation. In [85], PEM is proposed as the membrane between the two electrodes. Both glucose and oxygen have access to the anode. The outer part of the anode serves as a sacrificial layer where the oxygen can directly react with glucose on the surface of the non-selective catalyst (Pt based) and is consumed. This reduces the concentration of oxygen in the interior of the anode, where glucose is oxidized under almost anaerobic conditions. Similar to the designs discussed above, the performance of this fuel cell depends on the concentration of the oxygen in the reactant mixture. At lower oxygen concentrations, the reactant separation will be more effective. The design

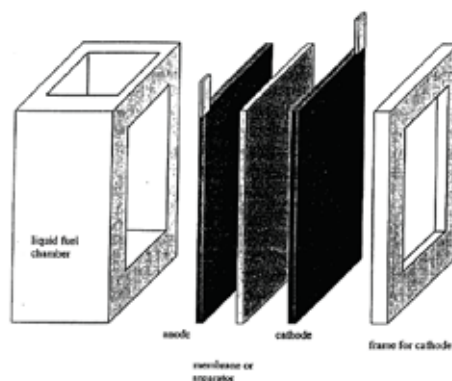
also requires that the glucose concentration must be higher than oxygen, since glucose directly reacts with oxygen at the anode and does not contribute to electron yield. These conditions are fulfilled in body fluids where glucose concentration is ca.  $5 \times 10^{-3}$  mol/L and oxygen is  $0.2 \times 10^{-3}$  mol/L [18].

The designs discussed so far have focused on implantable  $\mu$ DGFCs. Publications on abiotically catalysed  $\mu$ DGFC for non-medical applications are almost nonexistent. Apblett et al. [71] are the only research group to have fabricated a  $\mu$ DGFC similar in configuration to a typical  $\mu$ PEMFC (see Figure 3.2). They used graphite flow plates, carbon paper as diffusion layer, PEM as the electrolyte and catalyst ink (Pt-Ru for anode and Pt for cathode) as the catalyst layer. 1M Glucose solution was used as the fuel and the feed rate is 0.1 ml/min. 1M glucose solution is relatively viscous compared to other liquid fuels like methanol or ethanol, and is not able to appropriately wet all the surfaces in the flow field, the diffusion layer and the catalyst layer. In case of incomplete wetting, very low OCV and currents were observed. Apblett et al. [71], circumvented this problem by first introducing methanol fuel solution to the anode flow fields to obtain maximum wetting of the fuel cell layers. Later, the fuel feed is changed to glucose solution. Apblett et al. [71] have mentioned gluconolactone as the product of the oxidation of glucose which yields two electrons for each glucose molecule. Their  $\mu$ DGFC performance degraded with time, which they attribute to the poisoning of the Pt-Ru catalyst by gluconolactone. Gluconolactone is adsorbed by a catalyst site, which prevents further oxidation of glucose at that site. Apblett et al. also observed glucose crossover since Nafion is permeable to glucose [71].

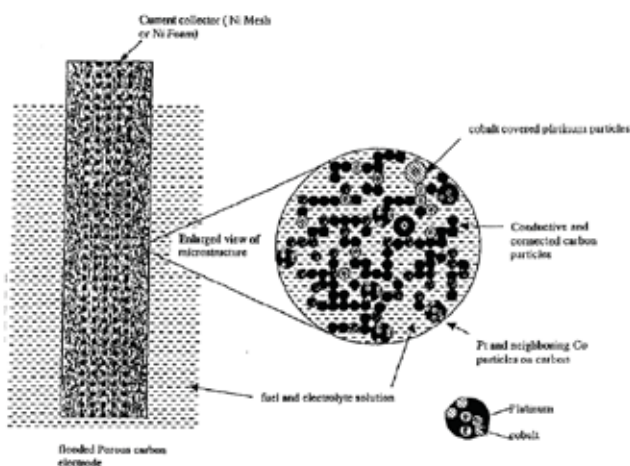


**Figure 3.22** (a) Schematic diagram of the  $\mu$ DGFC presented in [69]. (b) SEM image of the fibrous anode. Reproduced from [69].

Schechner et al. [69] have presented a membraneless single compartment DGFC for portable applications (Figure 3.22). Their design does not incorporate any means to keep the reactants separate. Glucose is mixed with the liquid electrolyte (KOH) solution and both are added together to the fuel cell's single compartment. One of the walls of the fuel cell compartment forms the cathode, which thus has access to ambient oxygen (Figure 3.22). As there is no membrane separating the fuel from the electrolyte, the glucose will also reach the non-selective cathode, causing considerable fuel crossover losses. The fuel cell uses fibrous anode with high surface to volume ratio. The fibrous anode are fabricated by first electrospinning [69] the polymer polycaprolactone (PCL) into unwoven fibrous mat and then plating the PCL fibres with silver for electrical conductivity and catalytic activity. The tests conducted by Schechner et al. concluded that the silver anode have lower performance compared to Pt and the crossover losses is a major factor for relatively low power density. The fuel cell has dimension of several centimetres (6 - 11 cm) and can only be considered for relatively large portable applications.



**Figure 3.23** Schematic of the DGFC presented in [86]. Reproduced from [86].



**Figure 3.24** Schematic diagram of the anode immersed in the fuel and electrolyte solution. Reproduced from [86].

A DGFC (Figure 3.23) for portable applications has also been reported by Chan et al. [86]. Similar to the design in [69], glucose and electrolyte (KOH or NaOH) must be mixed together and added to the cell chamber for operation. The anode is completely immersed in the fuel-electrolyte solution. The anode is formed of Pt particles supported on carbon black and embedded in a polymer [Figure 3.24]. Small amount of Co is also electrochemically deposited to the anode to increase the activity for glucose oxidation [86]. The anode also includes some cobalt oxides. The air breathing cathode with silver catalyst was procured from a commercial vendor. This fuel cell was also used by Mor et al. [87, 88] to study the effect of glucose concentration on the performance of the DGFC with KOH solution as the electrolyte. The study conducted in [87] observed that the OCV, peak power density and peak current have a dependence on the initial glucose concentration. The OCV, peak power density and peak current should increase with increase in glucose concentration. The performance of the fuel cell improved as the glucose concentration was increased from 0.22 to 0.89 M. However, above 0.89 M, the OCV, peak power and current become smaller with further increase in glucose concentrations. One possible explanation for the decrease in cell performance at higher glucose concentration is the increase in side reactions [87, 88]. These side reactions compete for glucose in alkaline conditions in the cell. In these second order reactions, glucose molecules react with each other or with intermediate reaction products of glucose oxidation and do not contribute to electron transfer. Examples of such side reactions that can occur in a DGFC are [87, 88]:

1. Cannizzaro rearrangement of aldehydes; a molecule of glucose is oxidized by another glucose molecule, which is itself reduced. The overall reaction is:



2. Aldol condensation of two glucose molecules, where the overall reaction is:



### 3.5.4 Performance

The performance figure of small scale abiotically catalyzed DGFCs published in the literature in recent years is summarized in Table 3.2.

**Table 3.2** Construction details and performance figures of abiotically catalysed miniature DGFCs.

DGFC Type	Reference	Catalyst		Electrolyte	Glucose Concentration	Oxygen Concentration /Source	OCV (mV)	Power Density ( $\mu\text{W}/\text{cm}^2$ )	Temperature ( $^{\circ}\text{C}$ )	Remarks
		Anode	Cathode							
Implantable	Kerzenmacher et al. [75]	Pt-Bi alloy supported on activated carbon	Activated carbon	PBS solution	$5 \times 10^{-3}$ mol/L	PBS solution is aerated ( $p\text{O}_2 = 196\text{mbar}$ )	$337 \pm 10$	$3.3 \pm 0.2$	$37 \pm 1$	Design shown in Figure 3.19. The performance figures mentioned are taken after 10 days of operation. After 234 days, the OCV and power density decrease to $241 \pm 6$ mV and $1 \pm 0.05$ $\mu\text{W}/\text{cm}^2$ respectively.
	Kerzenmacher et al. [70]	Pt-Bi alloy supported on activated carbon	Activated carbon	PBS solution (pH =7.4)	0.1 wt % of the PBS/Glucose solution	PBS solution is aerated	218	1.1	37	OCV and power density figures mentioned are taken after 40 days of operation of the DGFC.
	Stetten et al. [82]	Pt supported on activated carbon	Activated carbon	PBS solution (pH =7.4)	0.1 wt % of the PBS/Glucose solution	PBS solution is aerated	~480	~ 2	37	Design shown in Figure 3.18
	Stetten et al. [85]	Pt-Bi alloy supported on activated carbon	Activated carbon	PBS solution (pH =7.4)	0.1 wt % of the PBS/Glucose solution	PBS solution is aerated	~380	~3.5	37	
	Kloke et al. [83]	Pt-Zn alloy	Pt-Al alloy	PBS solution (pH =7.4)	$3 \times 10^{-3}$ mol/L	7% $\text{O}_2$ saturation	630	2	37	Design shown in Figure 3.20(b)
In-vitro applications	Apblett et al. [71]	Pt-Ru black	Pt black	PEM (Nafion)	1 M (feed rate is 0.1 ml/min)	20 sccm	~780	~ 2000	60	Design is similar to the generic PEMFC presented in Figure 3.1
	Schechner et al. [69]	Ag electrodeposited on fibrous polymer	Commercial cathode by E-TEK, material is not specified	1 M KOH	0.80 M	Ambient air	385	196	RT	Design shown in Figure 3.22(a). The fuel cell size is relatively large (8 x 6 x 11 cm) and can be categorized as small scale but not micro.
	Chan et al. [86]	Pt supported on activated carbon with some electrodeposited Co	$\text{AgNO}_3$	7 M KOH	1.85 M	Ambient air	850	~2500	RT	Design shown in Figure 3.23. The fuel cell size is relatively large and can be categorized as small scale but not micro.
	Mor et al. [87]	Pt supported on activated carbon with some electrodeposited Co	$\text{AgNO}_3$	0.87 M KOH	0.89 M	Ambient air	740	~610	RT	Used the fuel cell presented by Chan et al. in [86].

Earlier development of  $\mu$ DGFCs were made in the 1960s and 70s with focus on implantable applications. The performance figures of these early DGFCs can be found in [18]. The implantable DGFC of Table 3.2 have been tested only in-vitro but near-physiological conditions. Near physiological conditions refer to experiments in which the  $\mu$ DGFC is immersed in an aerated neutral buffer usually phosphate buffered saline (PBS) solution containing physiological amounts of glucose ( $\sim 5 \times 10^{-3} \text{ mol/L}^{-1}$ ) [18]. The performance of implantable DGFC is significantly lower than the ones meant for in-vitro applications. This is due to the fact that implantable DGFCs were tested at very low concentrations of glucose, using neutral buffered solutions that have low ionic conductivity. Another factor that affects the performance of implantable fuel cells is reactant crossover, which exists despite the implementation of different designs (discussed in Section 3.6.3) meant to mitigate the crossover losses.

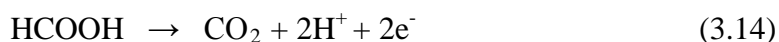
### 3.6 Other micro fuel cells

In addition to the micro fuel cells discussed so far, alternate micro fuel cell technologies have also been developed for portable applications. Some of them are briefly discussed in the following subsections.

#### 3.6.1. Micro direct formic acid fuel cell

Formic acid ( $\text{HCOOH}$ ) is an attractive alternate to methanol as a fuel source for direct micro fuel cells [28, 89- 91]. Formic acid is liquid at room temperature, common to the environment and, unlike methanol, is non-toxic (dilute formic acid is used as a food additive) [90]. Formic acid, being an electrolyte, is also expected to improve the proton conduction [90]. Micro direct formic acid fuel cells ( $\mu$ DFAFCs) are similar in design and construction to  $\mu$ DMFCs. Both can use Nafion as the electrolyte and Pt or Pt alloys as the catalysts [2, 28].

The oxidation of formic acid has improved reaction kinetics compared to methanol. The overall oxidation reaction of formic acid at the anode is given as:



The oxidation of formic can follow two reaction pathways for Pt catalysts [90]. The desirable reaction pathway directly forms  $\text{CO}_2$  and does not form CO as a reaction

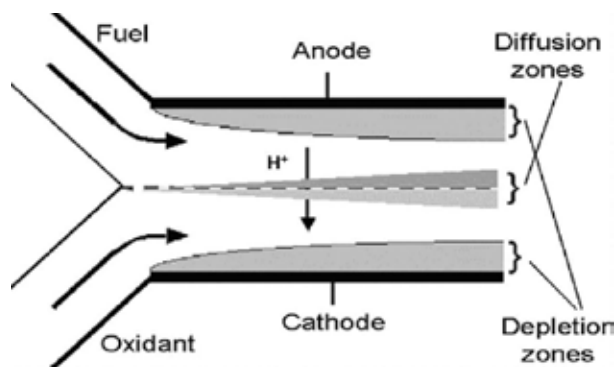
intermediate. However, in the second reaction pathway, adsorbed CO is formed as a reaction intermediate [90]. The adsorbed CO is further oxidized to the gaseous CO<sub>2</sub>. However, not all CO is oxidized, thus causing CO poisoning and reducing the number of active reaction sites. Adsorbed CO is also formed as a reaction intermediate for methanol. Appropriate anode catalyst selection can direct the formic acid oxidation to proceed in the direct oxidation pathway, circumventing the formation of CO intermediate. Rice et al. [92] have reported that Pt/Pd catalyst enhances the electrooxidation of formic acid by the direct pathway.

Compared to DMFC, DFAFC exhibits lower fuel crossover. This is because the permeation rate of formic acid through Nafion membrane is much lower than methanol [93]. Formic acid partially dissociates into formate anions (HCOO<sup>-</sup>), which are repelled by the sulphonic terminal groups within the Nafion membranes. This is assumed to be reason for lower crossover for formic acid. A decrease in fuel crossover allows  $\mu$ DFAFCs to be run at higher concentrations of formic acid [28, 89, 90]. The concentration of methanol is limited to 1-5 M [17] due to severe crossover [2, 28], whereas formic acid feed concentration as high as 20 M is viable [90]. DFAFC compares well with DMFC in terms of energy density. While the theoretical energy density of neat formic acid (2086Wh/l) is smaller than neat methanol (4690Wh/l) [89, 91], the fact that one can use higher formic acid concentrations compared to methanol means that energy density of  $\mu$ DFAFC is higher than  $\mu$ DMFC. For example, the energy density of 10M formic acid is 787Wh/l compared to 380Wh/l for 2M methanol.

$\mu$ DFAFC exhibit better performance compared to  $\mu$ DMFCs [28,89-91]. Yeom et al. ran their PEM based micro fuel cell on both methanol and formic acid. They reported power densities of 0.38mW/cm<sup>2</sup> for 1.25 M methanol and a relatively higher power density of 17mW/cm<sup>2</sup> for 10 M formic acid [28]. Yeom et al. also reported a  $\mu$ DFAFC in [91] with maximum power densities of 12.3mW/cm<sup>2</sup> when operating in passive air breathing mode and 30mW/cm<sup>2</sup> in case of forced oxygen flow. The  $\mu$ DFAFC reported by Ha et al. [89] produced a power density of 33mW/cm<sup>2</sup>. Chu et al. [31] fabricated a passive air breathing  $\mu$ DFAFC, which employs acid loaded porous silicon instead of Nafion as the PEM. They reported an impressive power density of 94 mW/cm<sup>2</sup> for a solution of 5M formic acid with 0.5M H<sub>2</sub>SO<sub>4</sub> as the fuel.

### 3.6.2 Laminar flow based fuel cell

A laminar flow based fuel cell (LFFC) incorporates all the fundamental components of a fuel cell into a single microchannel [94-99]. LFFCs are also referred to in the literature as membraneless fuel cells since they do not require a membrane for ion conduction and reactant separation. Compared to conventional PEM based micro fuel cells, LFFCs have several advantages [95,98]: the fuel and oxidant stream are kept separate without the need of a physical barrier or membrane; issues related to membrane hydration and cathode flooding are eliminated; fuel and oxidant crossover is almost nonexistent and the absence of a membrane means that device fabrication with MEMS technologies is simpler.

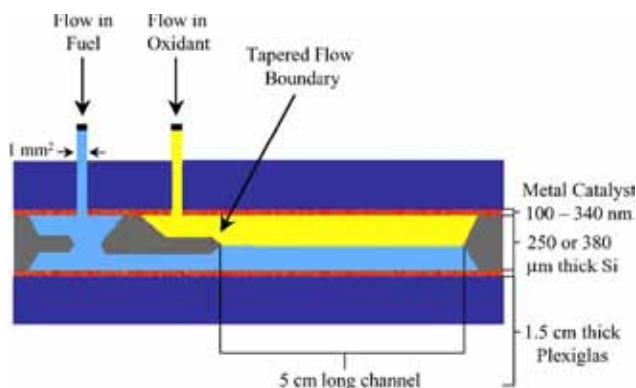


**Figure 3.25** Schematic diagram of top view of a Y-shaped LFFC. Reproduced from [96].

LFFCs exploit the phenomenon of multistream laminar flow to operate. Pressure driven flow in microchannels is generally laminar as the flow has low Reynolds number and reasonably high Peclet number (see Section 3.2). In multistream laminar flow, two or more separate fluid streams with laminar flow will merge into a single microchannel and continue to flow laminarily in parallel without turbulent mixing [94]. The only mechanism of mixing of the streams is the diffusion across their liquid-liquid interface. In a LFFC, a fuel stream and an oxidant stream flow laminarily in parallel along the length of a microchannel with minimal mixing as shown in Figure 3.25. The anode and cathode are placed on opposing sidewalls within the microchannel and usually cover the entire length of the microchannel. The fuel and oxidant streams and their common liquid-liquid interface provide the required ionic conduction for the LFFC to operate. The depletion zones, marked in Figure 3.25, are created close to surface of the electrodes as a result of the reaction of the fuel at the anode and the oxidant at the cathode. To promote ionic conduction, the fuel and/or oxidant are mixed with an acidic or alkaline



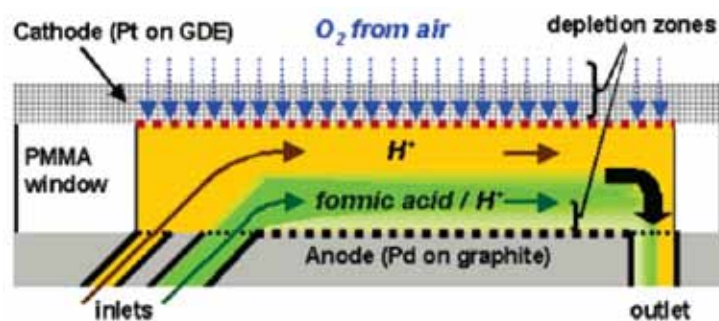
electrolyte before introducing them into the microchannel [94]. Formic acid or methanol are usually used as the fuel, and dissolved oxygen, hydrogen peroxide or permanganate is used as the oxidant.



**Figure 3.26** Schematic diagram of side view of a planar-LFFC. Reproduced from [100].

Currently, two designs exist for the LFFCs. The first design is Y-shaped microchannel with oxidant and fuel flowing side-by-side (Figure 3.25). For Y-shaped design, the fabrication of electrodes on the sidewalls of the microchannels is difficult to accomplish with available MEMS technologies [97]. The second design is the planar-LFFC (Figure 3.26). In planar-LFFC, the fuel and oxidant streams flow on top and bottom of each other or vice versa. The benefit of this design is that standard coating technologies can be easily used to fabricate the electrodes.

The performance of the LFFC using dissolved oxygen as the oxidant is mass transfer limited due to the low solubility of oxygen in aqueous solution (about 2mM)[94, 101]. Chohan et al [95] obtained a power density of 0.4 mW/cm<sup>2</sup> with 2.1M formic acid as the fuel and oxygen dissolved in 0.5M H<sub>2</sub>SO<sub>4</sub>. They improved the performance of their LFFC by using 0.144M potassium permanganate as the oxidant and obtained a power density of 4mW/cm<sup>2</sup>. Similar result was obtained by Li et al. [97]. They obtained a power density of 0.58mW/cm<sup>2</sup> for dissolved oxygen (O<sub>2</sub> saturated 0.1M H<sub>2</sub>SO<sub>4</sub>) and 1.98mW/cm<sup>2</sup> when hydrogen peroxide (0.01M H<sub>2</sub>O<sub>2</sub> + 0.1M H<sub>2</sub>SO<sub>4</sub>) is used as the oxidant. They used 0.5M formic acid in 0.1M H<sub>2</sub>SO<sub>4</sub> as the fuel solution. Jayashree et al. [101] addressed oxygen mass transfer limitation by integrating a porous air-exposed gas diffusion electrode (GDE) as the cathode into their planar-LFFC. The cross sectional view of their fuel cell design is shown in Figure 3.27. They reported a maximum power density of 26mW/cm<sup>2</sup> with formic acid as the fuel.

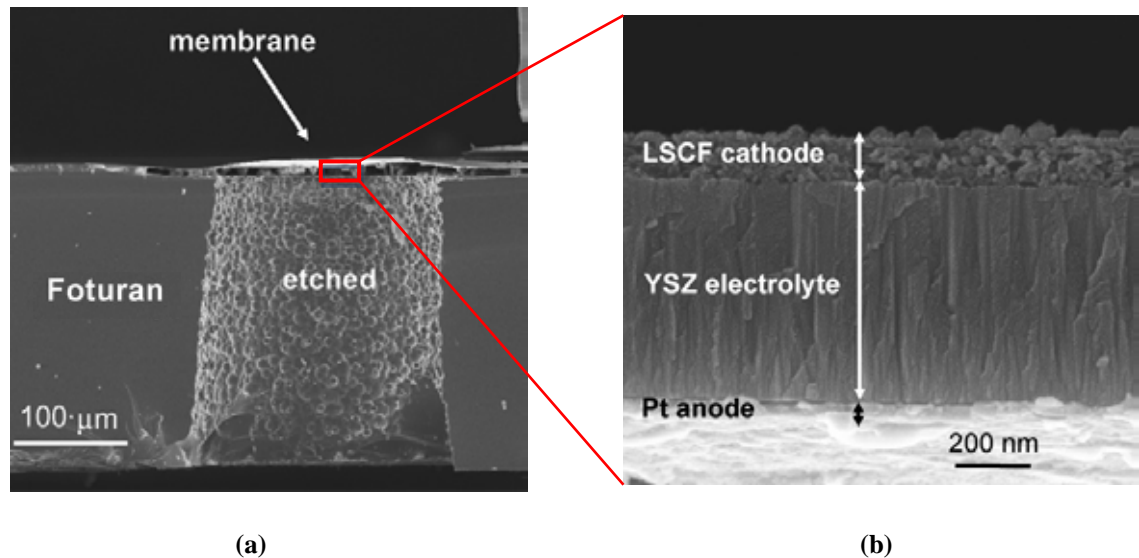


**Figure 3.27** Schematic diagram of side view of a planar LFFC with a porous, air breathing gas diffusion electrode (GDE). Reproduced from [101].

A challenge for LFFC is their inherently low fuel utilization. This problem can be mitigated by introducing design features that will split the fuel and oxidant streams and re-circulating them through the microchannel.

### 3.6.3 Micro solid oxide fuel cell

SOFC (see Section 2.4.6) has also been considered for portable applications [2, 9, 102–105]. Major benefit of micro SOFCs ( $\mu$ SOFCs) is their ability to directly use higher order hydrocarbon fuels, such as methane or propane, at the anode without any intermediate reformer. Higher order hydrocarbons have much higher energy density compared to methanol [2].  $\mu$ SOFC use ceramic based oxygen ion conducting electrolyte that do not require hydration to operate. Thus, water management in  $\mu$ SOFC is simpler compared to Nafion based fuel cells. Ytria stabilized zirconia (YSZ) [103], cerium gadolinium oxide (CGO) [104] and samaria doped ceria (SDC) [102] have been used as the electrolytes in  $\mu$ SOFCs. Similar to the electrolytes, the electrodes/ catalysts of  $\mu$ SOFC can also have complex chemistries. However, the ceramic electrolytes and the electrodes of  $\mu$ SOFC can be deposited using thin film technologies common to MEMS technologies. Thus, monolithic integration of the electrolyte with other fuel cell components is possible (see Figure 3.28). A comprehensive review of thin film deposition technologies used in fabrication of  $\mu$ SOFC has been recently published by Beckel et al. in [105].



**Figure 3.28** (a) SEM cross sectional view of a  $\mu$ SOFC MEA on a Foturan<sup>®</sup> substrate. (b) blow-up view of the MEA membrane. MEA is fabricated by thin film technologies: Pt anode by RF- sputtering, YSZ electrolyte by pulsed laser deposition and  $\text{La}_{0.6}\text{Sr}_{0.4}\text{Co}_{0.2}\text{Fe}_{0.8}\text{O}_3$  (LSCF) cathode by spray pyrolysis.

Reproduced from [103].

$\mu$ SOFCs operate at significantly higher temperatures, typically in the range of 500-600°C. Thermal management at the micro-scale, reducing the typically slow start-up time and controlling the mechanical stresses induced by rapid thermal cycling are key challenges of  $\mu$ SOFC technology. Due to the large surface to volume ratio at micro scale, controlling the operating temperature of  $\mu$ SOFC is difficult compared to conventional SOFCs. The large temperature gradient, ca. 500°C at the cell stack and near room temperature externally, requires excellent thermal blanketing. Large temperature drops will also induce greater mechanical stresses in the fuel cell components. Another challenge for  $\mu$ SOFCs is that at high temperatures it is difficult to maintain gas-tight seals for the electrode chambers and to ensure their reliability over longer times. This problem can be significantly reduced by using the single chamber  $\mu$ SOFC ( $\mu$ -SC-SOFC) design where both fuel and oxygen share a single chamber.

Though  $\mu$ SOFC technology faces considerable challenges, promising progress has been made in their development. Hütter et al. [103] reported a  $\mu$ SOFC where the MEA is fabricated by thin film technologies (Figure 3.28). They have reported an OCV of 1.06 V and a power density of 150mW/cm<sup>2</sup> at 550°C with butane as the fuel. The external temperature of the fuel cell reaches a manageable 35°C. Shao et. al. [102] fabricated a thermally self-sustained  $\mu$ -SC-SOFC with selective catalysts. They used propane as the fuel, which is first partially oxidized into H<sub>2</sub> and CO by the anode. This

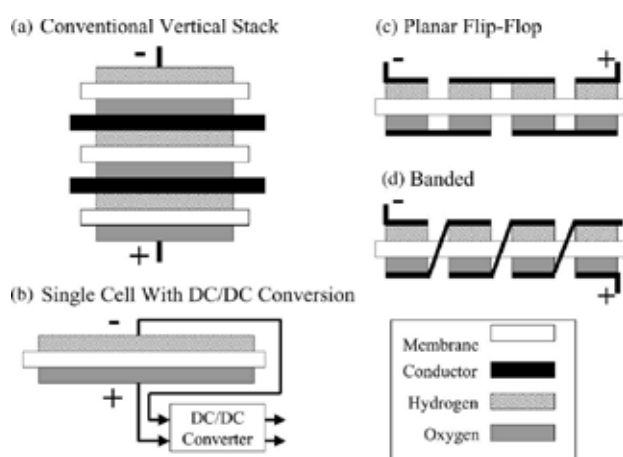
partial oxidation is an exothermic reaction and the heat generated is used to maintain the temperature of the fuel cell. A power density of ca.  $250 \text{ mW/cm}^2$  is reported at an operating temperature of  $500\text{--}600^\circ\text{C}$ .

### 3.7 System considerations

This chapter has so far focused on a single micro fuel cell without any BOP components. For practical applications, more than one cell would need to be electrically connected to provide the desired voltage. The connected micro fuel cells along with the essential BOP components make up the portable micro fuel cell system. The issues that need to be addressed in a micro fuel cell system are explained in the following sections.

#### 3.7.1 Cell connectivity

Individual micro fuel cells can be connected to each other in a vertical stack, planar flip-flop or banded configuration [43] as shown in Figure 3.6. The planar flip-flop and banded configurations are particularly favourable for air breathing fuel cells as all cathodes can be exposed to the atmosphere. However, the current collector's configuration is tricky for planar design as current distribution is not even. The stack design offers even current distribution; however, it requires forced flow of oxidant to operate.



**Figure 3.29** Micro fuel cell connectivity schemes: (a) generic vertical stack, (b) single cell with DC-DC converter, (c) planar flip-flop and (d) banded. Reproduced from [43].

### 3.7.2 Oxidant delivery

Oxygen transport to the cathode is a critical issue for fuel cell systems. Pure oxygen provides much better performance compared to air. However, to minimize the size of the device, it is more advantageous to use air from the surrounding environment instead of storing oxygen in the device. Air can be either transported through active means like external pump, compressors or fans to the cathode [3] or the fuel cell can be of passive self breathing design. In case of passive self breathing fuel cells, the entire surface of the cathode has to be exposed to the atmosphere [10]. For high current densities or longer duty cycles, in the absence of convection, the local oxygen concentration near the cathode of passive breathing fuel cell will deplete and oxygen diffusion path lengths will increase [3,10]. These oxygen transport limitations will limit the performance of the breathing fuel cell. The removal of water vapours from the cathode is also more challenging in passive designs, since it relies on free convection [10]. In case of absence of air, like in underwater applications, hydrogen peroxide or sodium percarbonate can be used as a source of oxygen [3].

### 3.7.3 Fuel delivery

Hydrogen can be supplied to the  $\mu$ PEMFC either through an onboard generation system like a reformer or through a storage device.  $\mu$ PEMFC systems with onboard reformers have been proposed [36, 106-109], in which hydrocarbons like methanol or chemical hydrides like sodium hydride are reformed to produce the hydrogen. In  $\mu$ PEMFCs with onboard reformers, thermal management is complex since the reformers operate at higher temperatures. A fuel reformer constitutes a significant portion of the BOP. It takes significant amount of energy from the device, thus lowering the overall efficiency of the fuel cell system. The second option of hydrogen storage in portable devices is also not without complexities. Hydrogen as a gas requires a very large volume, thus the systems volumetric power density is reduced if hydrogen is stored as a gas. Metal hydrides, carbon materials and recently carbon nanotubes have been proposed as storage materials for hydrogen. An important criterion of hydrogen storage is that the process should be easily reversible to enable the uptake and release of the gas when required. Compared to hydrogen, liquid fuels like methanol, formic acid, glucose and higher hydrocarbons (in case of  $\mu$ SOFC) are easier to store in a portable application. Fuel, like the oxidant, can be supplied with the help of pumping mechanism. For instance, Buie et al. [57] integrated an electroosmotic pump into their  $\mu$ DMFC for methanol delivery. The

fuel can also be stored in a pressurized compartment and the pressure can derive the fuel flow. More detail on issues related to fuel delivery in micro fuel cells can be found in [10].

### 3.7.4 Water management

$\mu$ PEMFCs can operate without any active water management. However, significant improvements in performance can be made if water flow in and out of the device can be controlled. PEM must be kept hydrated to ensure suitable proton conductivity. If the PEM dries up, the ohmic loss across the membrane is large. To keep the PEM hydrated, the hydrogen supplied to the anode is humidified. On the other hand, the water formed at the cathode can cause flooding. If the cathode is flooded, the oxygen can not access the reaction sites. Thus, in  $\mu$ PEMFC system, water must be removed from the cathode. Part of that product water can be feed to the anode while most of it can be rejected to the environment. Typically, the water is removed by pumping air into the cathode channels at significantly higher flow rates. However, some papers have presented alternate approaches. Buie et al. [110] used integrated electroosmotic pumping to actively remove water from the cathode. Metz et al. [111] used a passive approach to remove water. Their flow channels have a triangular design with tapered channel walls which pushes the water away from the GDL using capillary forces. Operating the fuel cell at relatively higher temperatures may also help in evaporating water but it will also remove water from the Nafion membrane. Integration of localized heaters in the micro fuel cell to evaporate water is another alternate. The heaters can operate in a cycle where they are used only for short duration of time when sufficient water has accumulated.

Water management is an important issue for  $\mu$ DMFC and  $\mu$ DFAFC [6,10]. Similar to  $\mu$ PEMFC, water must be transported to their anode and removed from the cathode.  $\mu$ DMFC requires water at the anode as it is an essential reactant in the oxidation reaction (See Table 2.1 for anode reaction). Further, water is also required to hydrate the PEM and dilute the fuel to lower crossover losses. In case of  $\mu$ DGFC, water is one of the reactants (Eq. 3.5 to Eq. 3.13) and is required at the cathode in case of alkaline electrolyte and at the anode in case of acidic media. As water is also a by-product, its requirement at one electrode is fulfilled by its production at the other. In case of one compartment  $\mu$ DGFC design, no active means are required to transport the water between the electrodes.

### 3.7.5 Thermal management

A by product of micro fuel cell operation is heat. If a fuel cell is operating at 50% efficiency and delivers 1W of electrical power to a portable application. Then, it also releases 1W as heat energy into its surroundings [10]. Fins or heat pipes can be used to enable the transfer of heat from the fuel cell to the environment.

The reaction kinetics of the fuel cell depends on the operating temperature. The hydration of PEM is also related to temperature. If the temperature is too high, evaporation will increase, causing the PEM to dehydrate. On the other hand, too low temperature will increase the condensation of water vapours, which will cause electrode flooding.

Thermal management is the biggest challenge faced by  $\mu$ SOFCs. Since they operate at temperature higher than 500°C, the start up time to reach the temperature is longer. The higher temperature also has to be maintained for the  $\mu$ SOFC to continue operation, thus good heat isolation is essential. Schemes can be implemented for thermal management. A heater can be implemented in case the operating temperature needs to be kept high.

### 3.7.6 Load handling

A portable fuel cell system should be able to respond quickly to changes in the power demand of the device, even from “cold start” [10]. The start-up transients in a fuel cell are due to the time it requires to reach optimum operating temperature and/or the time it takes to hydrate the membrane, in case the system is completely dry. Reaching optimum operating temperature in adequate time is a concern for  $\mu$ SOFCs. It is also an issue if the fuel cell is to operate in extreme conditions (near freezing). The humidification of a dry PEM is critical since it requires several seconds to achieve sufficient hydration. A solution to handle transients at start-up and during operation in a micro fuel cell is to include an auxiliary power system like a rechargeable battery; the fuel cell handles most of the power and the battery handles the transient loads [10].





# Chapter 4

## Single Compartment Micro Direct Glucose Fuel Cell

---

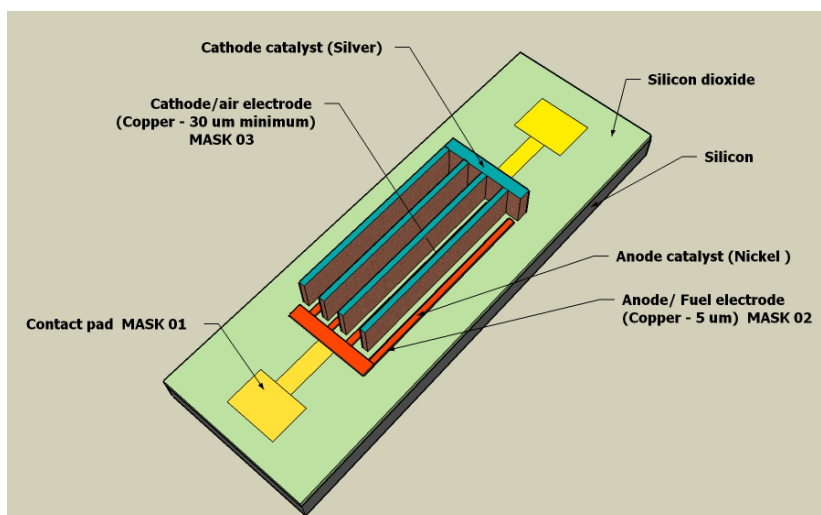
### 4.1 Overview

The single compartment micro direct glucose fuel cell (SC- $\mu$ DGFC) developed in this study is presented in this chapter. Basic operation and literature review of  $\mu$ DGFCs has already been discussed in the previous chapter. This chapter will focus on the design and microfabrication of SC- $\mu$ DGFC, which are discussed in the following sections.

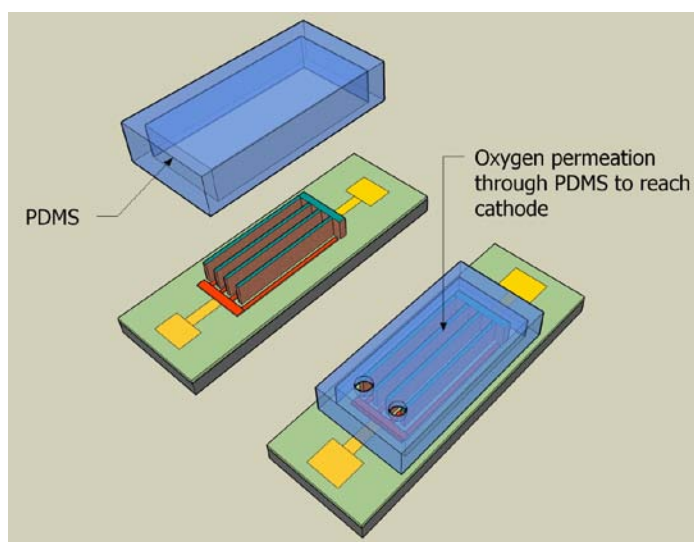
### 4.2 Design features

The design of SC- $\mu$ DGFC is considerably different from conventional stack or planar micro fuel cells. Simplified models of the SC- $\mu$ DGFC are illustrated in Figure 4.1 and 4.2. The main feature of SC- $\mu$ DGFC design is the single compartment for the fuel and electrolyte solution, which is shared by both anode and cathode. The compartment itself is formed of polydimethylsiloxane (PDMS) [112], which also serves as the membrane through which oxygen from ambient environment is able to permeate to the cathode. PDMS is a silicone elastomer which has high oxygen permeability [113]. PDMS has been used before as gas permeable membrane in micro fuel cells fabricated by Mitrovski et al. [114, 115]. Mitrovski et al. fabricated a passive  $H_2$ - $O_2$  micro fuel cells, which used liquid electrolyte ( $H_2SO_4$  or  $NaOH$ ) and electrodes (anode and cathode) that are embedded in PDMS. Hydrogen is force fed through a 0.9 mm thick PDMS membrane to the anode, whereas the cathode takes ambient air that has permeated through the PDMS

membrane. They reported a stable power density of  $0.45\text{mW}/\text{cm}^2$ . Increasing the feed concentration or decreasing the membrane thickness results in linear increase of permeation of air through PDMS [113]. Since, SC- $\mu$ DGFC is of passive self-breathing type, reducing the membrane thickness is the only means to improve oxygen permeation. SC- $\mu$ DGFCs with PDMS membrane thickness ranging from 50 to 250  $\mu\text{m}$  were fabricated in this study.



**Figure 4.1** Simple model of SC- $\mu$ DGFC without the PDMS membrane



**Figure 4.2** Simple model of SC- $\mu$ DGFC after PDMS membrane has been bonded with the substrate.

The anode and cathode of the SC- $\mu$ DGFC are configured in an interdigitating comb electrodes format. This design feature is unique and has only been reported before

by Buergler et al. [104], which have used interdigitating electrodes in their SC- $\mu$ SOFCS. As discussed in previous chapters, reactant crossover is the most critical issue in single compartment fuel cells. Ideally, the catalysts should be selective; otherwise same reactions will occur at both electrodes. Usually enzymes are used as catalysts to achieve this high selectivity in simple one compartment biofuel cells [13]. In our design, metals are used as catalysts since they are compatible with typical microfabrication techniques. In the design of SC- $\mu$ DGFC, two features are incorporated to mitigate losses associated with reactant crossover:

- i. Silver is used as the catalyst at the cathode. Silver is known to selectively reduce oxygen in the presence of glucose [18].
- ii. Non selective catalyst like nickel or platinum is used as catalyst at the anode for glucose oxidation. To reduce the amount of oxygen reaching the anode, the cathodes comb electrode's fingers are at least 25 $\mu$ m (or 45 $\mu$ m in some cases) higher than that of anode. Thus, oxygen diffusing through the PDMS will reach cathode first and would have to further diffuse through fuel/electrolyte solution to reach the anode.

### 4.3 Fabrication

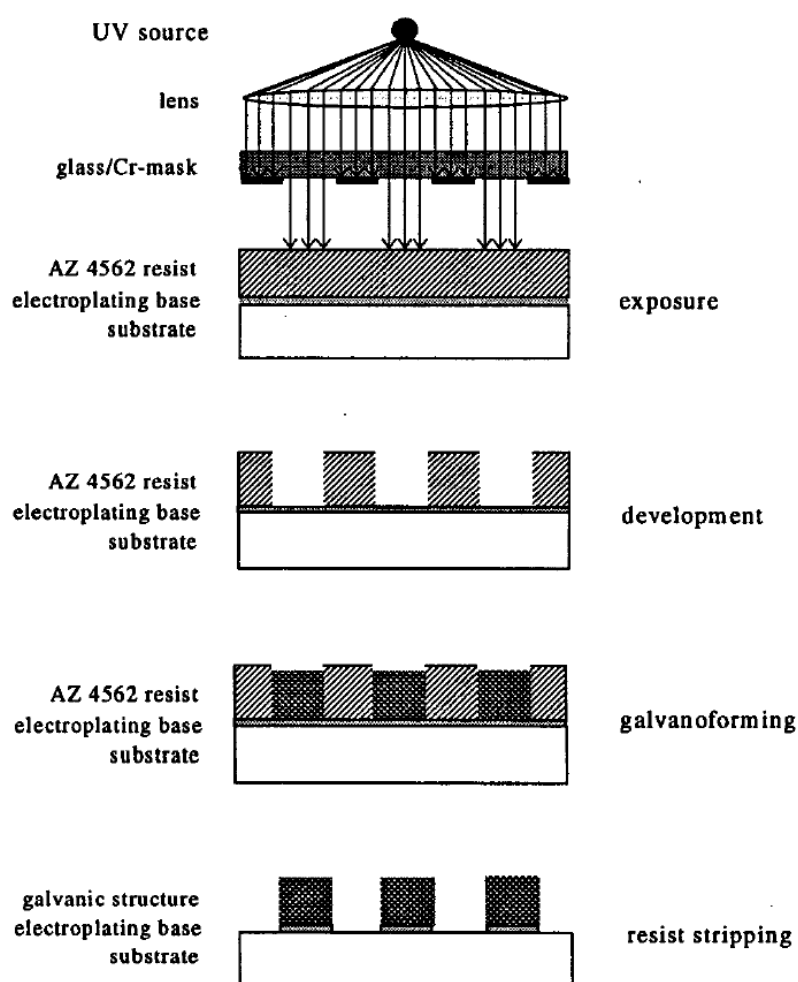
Before all fabrication steps of the SC- $\mu$ DGFC are presented, important processes related to its fabrication need to be explained. The important processes which are discussed in the following subsections include:

- UV-LIGA for fabricating the interdigitating comb electrodes
- Deposition of catalysts on electrodes by lift-off
- Etching of copper seed layer
- PDMS moulding for fabricating the SC- $\mu$ DGFC compartment and membrane
- Bonding PDMS membrane with substrate containing the comb electrodes

#### 4.3.1 UV-LIGA process

LIGA (a German acronym for lithographie, gavanoformung, abformung) technology was introduced more than two decades ago for fabricating high aspect ratio (ratio of feature height to width) metallic or polymeric microstructures [116]. The microstructures fabricated by LIGA process can be several millimetres in height with aspect ratios as high as 100:1 [116-118]. For fabricating metallic microstructures, the

LIGA process starts by coating a conductive substrate with an X-ray sensitive polymer (resist), usually PMMA, which can be up to several millimetres in thickness. The PMMA resist is exposed to short wave (0.2-2nm) and high energy X-rays through a special X-ray mask having the desired microstructure patterns. Parts of the PMMA-resist exposed to the X-rays are chemically altered and dissolved in a chemical developer. The remaining PMMA forms the template for fabricating the desired microstructures by electroplating. The main drawback of LIGA fabrication is that it is very expensive. The X-rays are generated by complicated and expensive synchrotron radiation source which are available only in large labs. Also, the masks used in X-ray lithography are complex and not simple to fabricate.



**Figure 4.3** Principle and fabrication step of UV-LIGA. Reproduced from [117].

UV (ultraviolet)-LIGA technology is a much cheaper alternate to LIGA for fabricating metallic microstructures with moderate aspect ratios. UV-LIGA utilises

ultraviolet source, instead of X-ray, to expose the resist (photoresist). The masks used in UV-LIGA process are simple chromium-glass masks or plastic masks. Figure 4.3 illustrates the fabrication steps involved in UV-LIGA process. The process can be divided into two main parts: (i) UV lithographic patterning of thick film photoresist and (ii) electroplating copper (or other structural material) into the resulting resist pattern.

#### 4.3.1.1 Thick film photoresist processing

The thick film photoresist used in this work is AZ4562. AZ4562 is a Novolak based positive photoresist, which implies that the part of the resist exposed to the UV light is chemically altered and dissolved in the developer. Compared to thinner resists like AZ5214, AZ4562 resists has high viscosity due to lower concentration of solvents and higher optical transparency due to relatively lower concentration of photoactive compound [119]. AZ4562 film can be up to 100 $\mu$ m thick and aspect ratio as high as 10:1 has been reported. It is compatible with IC technology, exhibits good adhesion to most substrates and can be easily stripped by acetone.

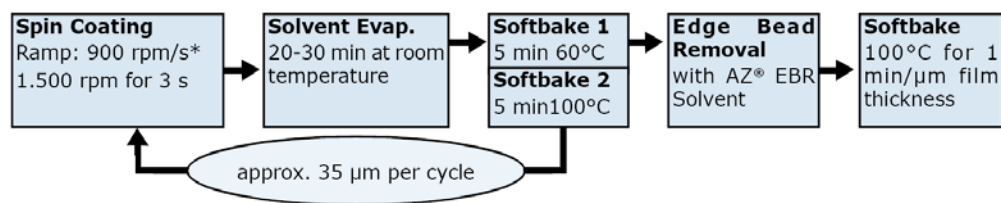
The processing of AZ4562 has complexities which are not encountered during the processing of thin photoresist. The lithography process with AZ4562 resist involves the following sequential steps:

1. *Dispensing*: Manual dispensing of thick photoresist on the substrate with pipette often leads to air bubbles in the resist film. An easier way is to carefully dispense AZ4562 onto the substrate from a small beaker. Usually a substantial excess of photoresist is dispensed compared to the amount that will remain in the final thickness. Before the resist is dispensed, the substrate surface is coated with hexamethyldisilazane (HMDS) to improve adhesion.
2. *Spinning*: To attain a resist film thickness of few tens of  $\mu$ m by spin coating, either the spin speed or the spin time is reduced [119]. Though edge bead is unavoidable, it is more prominent if reduction is made to the spin speed [119]. Edge bead is the photoresist which is accumulated on the rim/edge of the wafer and is many times thicker than the resist thickness in the middle of the substrate. It is usually 3-7mm in width. Edge bead is caused by the surface tension of the resist as surface tension effects make it difficult for solution that is flowing radially outward to detach from the wafer [120]. The evaporation of the solvents during spinning will further increase the viscosity of the resist and increase the accumulation of the resist at the edge [8]. Edge bead prevents a good contact

between the mask and the resist, causing an undesired proximity gap during exposure. This will reduce the lateral resolution and affect the wall profile of the patterns [121]. Edge bead can be lowered/minimized during the spinning process by implementing one of the following solutions [119]:

- Higher spin speed for a shorter duration
  - A spin-off of the edge bead by abruptly increasing the spin speed for a very short duration at a certain stage of the spinning process. Roth et al.[121], introduced the large acceleration spikes in their spin process profile. They only noticed a reduction in the width of the edge bead but not the height.
  - Multiple coating with higher spin speeds for each coating cycle
  - Manually removing the edge bead with a solvent
  - A delay between the coating and prebake prevents the edge bead from growing due to thermally reduced viscosity.
3. *Relaxation:* A delay of 15 to 20 minutes between the coating and the prebake allows solvent to evaporate from the resist. This prevents the edge bead from growing due to thermally reduced viscosity during the prebake step. Relaxation time also enables the resist to settle. Relaxation time is very important in case oven is used for the prebake.
4. *Prebake:* Prebake (softbake) is a very critical step. It influences the exposure energy, development time, structure definition, side wall profile and aspect ratio [121]. Oven or hotplate can be used for prebake. In case an oven is used for prebake, the surface of the photoresist will dry quite fast, forming a crust and trapping some solvent in the bulk of the film [121, 122]. The trapped solvents may form bubbles and lift the resist film, resulting in adhesion failure [122]. This can be avoided by introducing relaxation time before prebake. Prebake in oven takes considerably long time (several hours for few tens of  $\mu\text{m}$ ) and the temperature profile inside an oven is non-homogenous [123]. Hotplate is a better option compared to oven, especially when the temperature is ramped to the final value. In case the temperature is not ramped, and the substrate is directly put in contact with the hotplate at final baking temperature, the thick resist tends to flow which results in non-homogenous resist thickness [121]. The parameters for prebake are very critical. If the prebake is too cool or too short, it may cause bubbles in the resist close to the substrate by nitrogen formed during exposure.

Also, the remaining solvent not evaporated due to cooler/shorter prebake will cause high dark erosions (i.e. dissolution of unexposed resist in the developer). A prebake that is too long or too hot decomposes a fraction of the photo active compound, thus decreasing the development rate and may increase dark erosion [119]. The very low concentration of solvents embrittles the resist and makes it susceptible to cracks [119]. In [119], a prebake at 100°C for 1 minute per 1  $\mu\text{m}$  resist film thickness has been proposed as a good compromise between sufficient solvent evaporation and minimized loss of the photoactive compound. In case multi-layers of resist are spun on the substrate, each coating is followed by a short prebake step. This is illustrated in Figure 4.4.

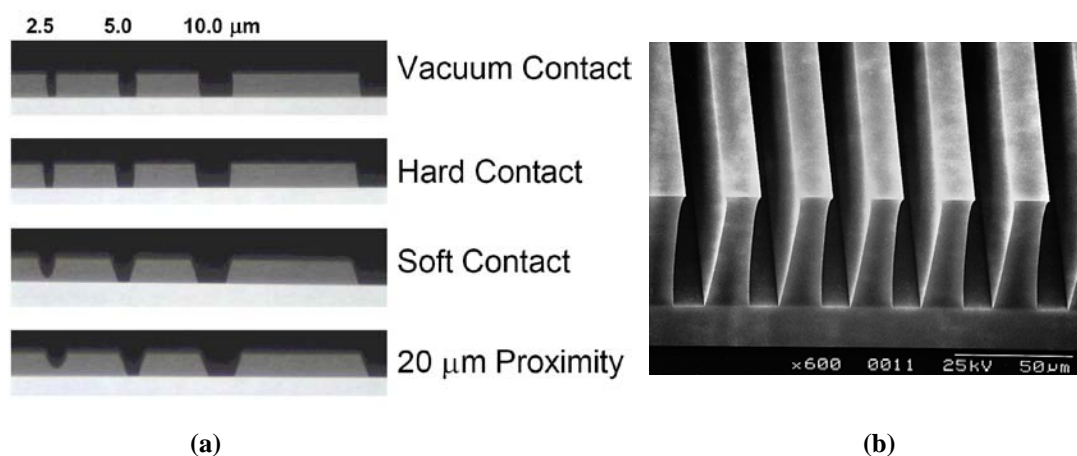


**Figure 4.4** Example of spinning and prebaking cycle for multiple coating.

Reproduced from [119].

5. *Rehydration*: A certain amount of water content is required in the resist film during exposure to maintain a reasonably high development rate and a high contrast [121,124]. However, during the prebake, the water concentration of the resist film drops [124]. A time delay between prebake and exposure is necessary to allow water from the air to diffuse into the resist. Time required to rehydrate the complete photoresist film not only depends on the resist thickness but also on the temperature (water diffusion in the resist is thermal activated) and the air humidity of the room. Usually, thin films (AZ5214) of few  $\mu\text{m}$  thicknesses take a few seconds to rehydrate. Whereas, thick films (AZ4562) of few tens of  $\mu\text{m}$  thickness may take several hours for complete rehydration.
6. *Exposure*: AZ4562 exhibits spectral sensitivity in the UV range of 310-440nm. For thick film resists, high exposure energy is required to assure the illumination through the entire resist layer thickness [121]. AZ4562 layers with thickness in the range of 100 $\mu\text{m}$  require several minutes of exposure [125]. During exposure the photoactive compound diazonaphtoquinone (DNQ) is converted into indene carboxylic acid with  $\text{N}_2$  as side product [119]. This transformation also decreases

the absorbance of the resist, which becomes more transparent to UV light [118]. If the exposure intensity (given in  $\text{mW}/\text{cm}^2$ ) is too high,  $\text{N}_2$  bubbles may appear in the resist film. To prevent bubble formation, multiple exposures of relatively shorter duration with delay between exposures is helpful. Bubble formation is also associated with high exposure dose (given in  $\text{mJ}/\text{cm}^2$ ), in which case exposure dose must be optimized. The exposure tool used in this work is the Karl Süss MA6 mask aligner, which has a mercury lamp with its UV spectrum peaking at 365nm (i-line). The contact mode between the mask and the resist contributes in defining the resolution and wall profile of the resist [126]. The



**Figure 4.5 (a)** Effect of wafer/mask contact modes on thick film photoresist side wall profile.

Reproduced from [128], **(b)** wall profile of 80μm thick AZ4562 with vacuum contact mode. Reproduced from [129].

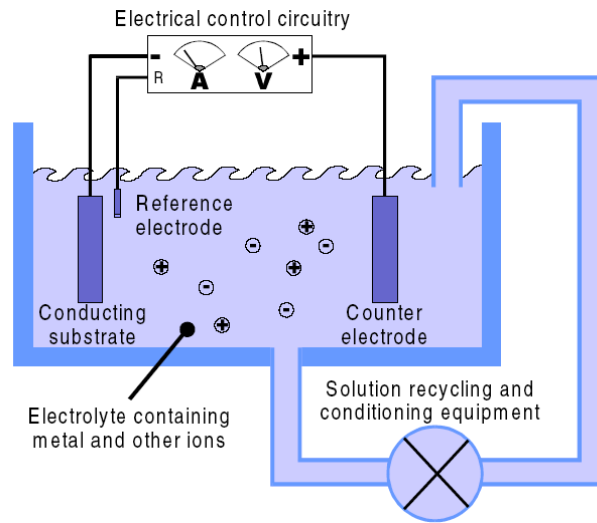
exposure modes available in the MA6 mask aligner are: soft contact, hard contact, vacuum contact and proximity. In the soft contact mode, simple mechanical contact is made between the mask and the wafer, whereas for hard contact mode, nitrogen gas flowing against the back of the wafer pushes the wafer towards the mask to improve contact. In vacuum contact mode, the wafer/mask contact space is pumped down to create a vacuum, realizing the best wafer/mask contact. In proximity mode, the wafer and the mask never come into physical contact and a gap exists between the wafer and the mask during exposure. The wall profiles of a thick film positive photoresist for different contact modes are shown in Figure 4.5(a). For thick film resist, vacuum contact mode is preferred for better resolution as diffraction effects are relatively less



compared to other modes. However, even vacuum contact mode does not yield vertical sidewalls. For vacuum contact mode, undercut is observed just below the photoresist surface and the pattern width is widest at the point and becomes narrow towards the bottom [125]. The undercut is attributed to the diffraction effect, which has been explained in [127].

#### 4.3.1.2 Copper Electroplating

Through-mask electrodeposition of metals/alloys is a well known MEMS technology for fabricating high aspect ratio metallic micro and nanostructures [117, 130]. In through-mask electrodeposition, limits on achievable line width and aspect ratio of the structure are defined by the patterning technique (like lithography). During the electroplating process, the copper ions present in the electrolyte solution are reduced at the surface of the conductive substrate to form the electroplated metal structure. A simple schematic diagram of an electroplating system is shown in Figure 4.6.



**Figure 4.6** Schematic diagram of an electroplater. Reproduced from [130].

The electroplating system consists of [130]:

- An electrically conductive substrate to be electroplated. In this work, the substrate is a silicon wafer with silicon dioxide layer. A 150-200 nm copper thin film is deposited on the wafer to make it electrically conductive and facilitate the nucleation mechanism during beginning of copper electrodeposition. The conductive substrate is also referred to as the cathode.

- The electrolyte solution also referred to as the electroplating bath solution. The bath solution contains the metal ions (e.g. cupric ions) that will be deposited on parts of patterned seed layer exposed to the solution. The bath solution also contains other supporting chemicals like acids (e.g.  $\text{H}_2\text{SO}_4$ ) and proprietary additives.
- A counter electrode (anode) consisting of a soluble metal, usually the same metal as the one being deposited.
- An electrical current or voltage source for controlling the deposition.
- Additional components such as pumps to circulate the bath solution, heater for heating the electrolyte, current and temperature controllers, and filters to keep the bath solution clean.

The uniformity of electroplated Cu is dependent on quality of the seed layer, the chemistry of the bath solution and electrical parameters (plating current and voltage). Cu seed layer is deposited using sputtering or E-beam evaporation. Time delay between seed layer deposition and Cu electroplating should be kept to a minimum. If the Cu seed layer is allowed to sit over time in the clean room, its surface will be oxidized. Oxidation of Cu seed surface prevents wetting during subsequent copper electroplating, which leads to formation of voids in the plated structures [131]. In addition to oxide formation, photoresist residues may remain on the seed layer after the lithography process. These residues will block the electrodeposition of Cu on seed layer, thus causing defects. A number of surface treatments for Cu seed layer have been proposed to counter seed layer contamination [131]. These are:

- Copper oxide reduction by exposure to hydrogen plasma.
- Reverse electroplating technique, in which the Cu wafer acts like the anode when current is applied. The surface of wafer is dissolved, exposing a fresh Cu layer.
- Rinsing the substrate in the electrolyte bath solution. The  $\text{CuSO}_4/\text{H}_2\text{SO}_4$  based electrolyte solution etches the native copper oxide.
- $\text{O}_2$  (or  $\text{O}_2/\text{CH}_4$ ) plasma treatment for removing photoresist residues and inorganic contaminants.
- 10 second dip in 1 - 10% nitric acid to remove copper oxide.

Electrolyte bath solution chemistry is very critical in achieving uniform deposition. Acid copper sulphate bath are the most common type of electrolyte employed for Cu electrodeposition. This bath contains copper sulphate which dissolves in the electrolyte and results in free hydrated cupric ion. This ion is reduced to copper metal during the electrodeposition. Typical cupric ion concentrations in the electroplating bath range from 10 to 60 gm/L [132]. A high concentration of cupric ion will increase the deposition rate. Whereas lower cupric ion concentration will lower the deposit thickness variations across the wafer. Usually sulphuric acid is used in the bath solution to improve the conductivity of the solution and improve wetting and oxide dissolution on Cu seed layers [132]. Typical concentration values for sulphuric acid are from 45 to 325g/L. Electroplating baths with higher concentration of sulphuric acid are usually meant for fabricating very high aspect ratio (20:1) or complex structures. Commercially available bath solutions also contain propriety organic additives. These additives play a significant part in improving the uniformity. More information on additives can be found in [132].

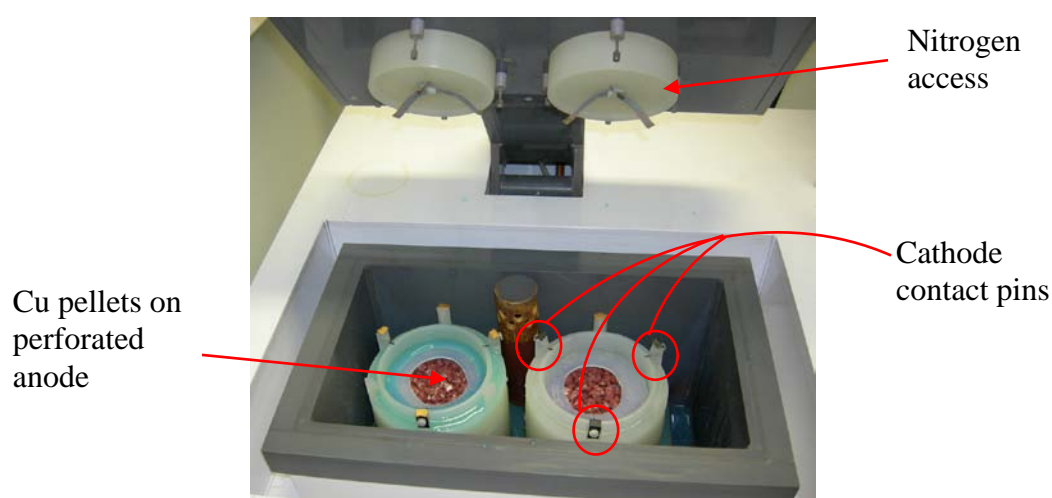
Typical deposition rate of electroplating range from 0.1 to a few  $\mu\text{m}/\text{min}$ . The deposition rate is given as [130]:

$$\frac{h}{t} = \alpha \frac{IM}{nFA\rho} = \alpha \frac{iM}{nF\rho} \quad (4.1)$$

Where  $\alpha$  is the current efficiency (usually above 90% for metal electrodeposition),  $I$  the total current,  $t$  the duration of the deposition,  $n$  the charge of the deposited ions,  $F$  Faraday's constant,  $h$  and  $A$  the thickness and area of the deposit,  $\rho$  the density of the deposit,  $M$  the molar mass and  $i$  the current density. The deposition rate increases proportionally with current density. Though, typical values of current density are from 5 to 50  $\text{mA}/\text{cm}^2$ , 15 to 25  $\text{mA}/\text{cm}^2$  are usually used in microfabrication field. Lower current densities yield uniform depositions, whereas at higher current densities non-uniform depositions are common.

Figure 4.7 and 4.8 present the Cu electroplating system used in this work. The bath solution for the electroplater was prepared in-house. The electrolyte holding tank of the electroplater has a capacity of 5 litres. The electrolyte bath comprised of copper sulphate pentahydrate (60gm/L) and sulphuric acid (230gm/L). No additives were used. The solution is pumped through the anode as shown in Figure 4.8. The wafer is placed

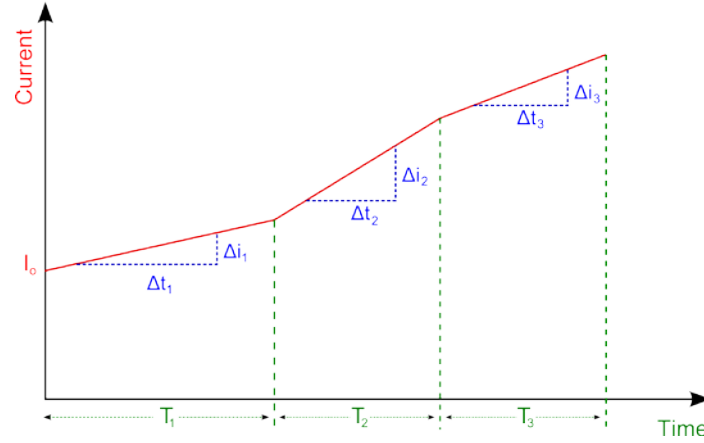
horizontally on the holder and pressure must be applied so that the cathode pins could pierce through the photoresist to make electrical contact with the seed layer. The anode comprises of copper pellets laid in three layers on a stainless-steel circular perforated mesh with electrical contacts (see Figure 4.7). The holding tank has a heater to control the temperature of the bath solution. The plating is performed at room temperature. The current and time parameters that can be adjusted in the electroplater are shown in Figure 4.9. The current and time increments are usually required in case the geometrical surface area of the structures being electrodeposited is continuously increasing.



**Figure 4.7** Photos of the Cu electroplater used in fabricating the SC- $\mu$ DGFC electrodes. Top lid of electroplater is opened and the anode Cu pellets and cathode (wafer) contact pins are visible.



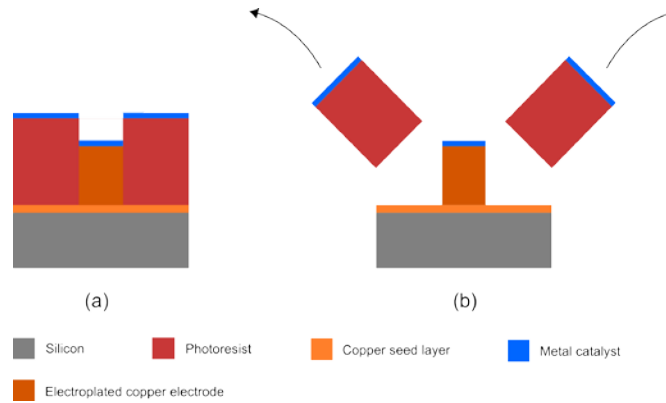
**Figure 4.8** Electroplating bath solution is flowing through the Cu pellets (and perforated copper anode) in the bottom of the wafer holder cup.



**Figure 4.9** Example of plating current profile possible with the Cu electroplater used in this work. The parameters that can be independently adjusted are initial current ( $I_0$ ), plating times ( $T_1$ ,  $T_2$  and  $T_3$ ), current increments  $\Delta i_j$  and time increments  $\Delta t_j$  corresponding to  $\Delta i_j$ .

### 4.3.2 Catalyst deposition

The catalyst is deposited on the Cu electrodes using the lift-off process [8] depicted in Figure 4.10.



**Figure 4.10** Lift-off process (a) metal deposition on copper electrode and photoresist (b) photoresist dissolution and metal lift-off.

In the lift-off process the resist acts like a sacrificial layer. After the UV-LIGA process, metal thin film is deposited on the resist and copper electrode, followed by resist dissolution in solvent. All the metal that is not in contact with the copper electrode will be removed (lifted-off). The catalyst thin film is deposited either using sputtering (for Pt) or E-beam evaporation (for Ni and Ag) deposition technique. The deposition process must take place below ca. 120°C temperature; otherwise, complete dissolution of the photoresist may become difficult. The resist is dissolved in acetone accompanied by ultrasound agitation. To remove resist residues, the sample is also cleaned in isopropanol. Another requirement for a successful lift off process is that the metal deposition should have poor step coverage. Thus, line-of-sight methods like evaporation

are more suitable for lift-off [8]. Photoresist sidewalls with undercut (Figure 4.5 (b)) or retrograde profile are useful in minimizing the unwanted deposition of metal on the sidewalls [8].

Since catalysis is a surface process, catalyst layer as thin as 5nm should be sufficient. However, the final step in the fabrication of the electrode assembly of the SC- $\mu$ DGFC is the etching of the copper seed layer. During this process, the catalysts are also exposed to metal etchants. To avoid unintentional complete etching of the catalyst layers, their film thickness is kept more than 80nm.

### 4.3.3 Copper seed layer etching

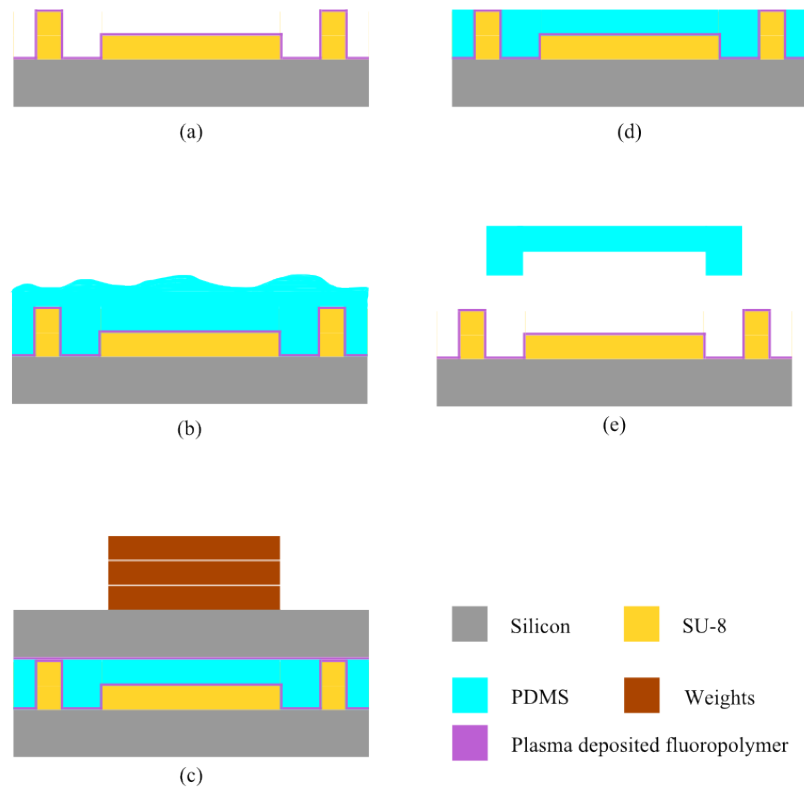
The Cu seed layer must be etched after the fabrication of the electrodes, otherwise the anode and cathode will remain short circuited and the fuel cell will not operate. There are several acid based etchant chemistries that can easily etch Cu. However, to selectively etch Cu in the presence of other metals is a more challenging task. In this work Cu and the underlying Cr or Ti adhesion promotion layer must be etched selectively in the presence of Ni or Pt (anode catalyst), Ag (cathode catalyst) and Ti (Cu current collector protection layer). Pt and Ti are chemically stable metals and are not easily etched by commonly used Cu etchants. However, Ni and Ag are etched by Cu etchants. The etchant solutions studied in this work are: 10% nitric acid ( $\text{HNO}_3$ ), dilute sulphuric acid, ammonium hydroxide, dilute hydrofluoric acid,  $\text{FeCl}_3$  solution, phosphoric acid at different temperatures (RT to  $120^\circ\text{C}$ ), Al etchant (85%  $\text{H}_3\text{PO}_4$ , 5% nitric acid, 5% acetic acid, 10%  $\text{H}_2\text{O}$ ) at RT and  $50^\circ\text{C}$ , 0.05%  $\text{H}_2\text{SO}_4$  with few drops of  $\text{H}_2\text{O}_2$ ,  $\text{HCl} - \text{H}_2\text{O}_2$  3:1 solution and Cr etch solution. The Cr etch solution provided the best result for Cu selective etching against Ni, Ag, Pt and Ti.

The composition of the Cr etch solution is: 200g of cerium ammonium nitrate ( $\text{Ce}(\text{NH}_4)_2(\text{NO}_3)_6$ ), 50ml of perchloric acid ( $\text{HClO}_4$ ) and ca. 1100ml of DIW. The solution is prepared by adding 700ml of DIW into a vessel and adding 50ml of  $\text{HClO}_4$  into the DIW and stirring with a magnetic mixer. Then 200 gm of  $\text{Ce}(\text{NH}_4)_2(\text{NO}_3)_6$  is added, and the solution is stirred until all of  $\text{Ce}(\text{NH}_4)_2(\text{NO}_3)_6$  has dissolved. Finally, more DIW is added to the vessel so that the final solution volume is 1200 ml. The etching of ca. 200nm thin Cu seed layer takes approximately 2 minutes in the Cr etch solution. The etch rate for Ni and Ag in the Cr etch is very low. Surprisingly, the Cr etch solution does not etch ca. 15 nm thin Cr adhesion promotion layer. Cr layer is later etched using a 37%  $\text{HCl}$  solution, which takes ca. 20 seconds. If Ti is used as the

intermediate layer, it can be removed by a very dilute HF solution (ca. 5ml of HF in 200 ml of DIW).

#### 4.3.4 PDMS cover/membrane fabrication

PDMS, a silicon based organic polymer (silicones), is widely used in microfabrication. A large number of microfluidic devices are manufactured in PDMS [133]. Fabrication of microfluidic devices particularly channels in PDMS is very easy as it can be cast against a suitable mould with sub- $0.1\mu\text{m}$  fidelity [112]. PDMS also has useful physical and chemical properties: it is optically transparent, electrically insulating, elastomeric with tuneable Young's modulus, thermally insulating, chemically inert, hydrophobic (low surface energy), impermeable to liquid water, permeable to gases and non polar solvents and nontoxic [112]. As mentioned in Section 4.2, PDMS is used in this work for its high gas (oxygen and other gases) permeability, which allows gas transport through bulk PDMS. PDMS components are usually fabricated using the soft lithography technique of replica moulding (casting). The steps involved in the fabrication of the PDMS compartment for the SC- $\mu$ DGFC are illustrated in Figure 4.11.



**Figure 4.11** Fabrication of PDMS compartment /membrane by replica moulding. (a) Fabricated SU-8 master, (b) PDMS prepolymer is poured on the master, (c) PDMS is heat cured under uniaxial pressure provided by the weights, (d) top wafer is removed, (e) PDMS replica is peeled off from the master and unwanted PDMS is removed.



**Figure 4.12** PDMS is being cured at room temperature and under pressure.

The top wafer and the weights are visible in the photo.

The process starts with the fabrication of an SU-8 master (or mould). The fabrication of the master is explained in detail in the next section. PDMS used in this work is supplied by Dow Corning (Sylgard 184 Silicone Elastomer Kit), and comes in two liquid components, a base and a curing agent. The base is mixed with the curing agent in a 10:1 ratio by weight. Mixing the two components results in the formation of air bubbles in the liquid PDMS prepolymer. The PDMS prepolymer is degassed by keeping it in vacuum for 40 minutes. A vacuum dessicator is used for this purpose. The master wafer is placed in a plastic petri dish and ca. 8 grams of PDMS prepolymer is poured onto the master. To control the thickness of the PDMS membrane a Si wafer is placed on top of the poured PDMS, followed by 800 grams of weight. The weights apply uniaxial pressure on the wafer-PDMS-master sandwich (see Figure 4.11(c) and 4.12). The applied pressure causes the higher support feature on SU-8 master to come in contact with the top wafer by excluding the PDMS. The thickness of the PDMS membrane is defined by the height difference between the higher (support) and lower (compartment) feature of the SU-8 master. According to the manufacturer (Dow Corning), the PDMS is cured in 48 hours at room temperature, 45 minutes at 100°C, 20 minutes at 120°C or 10 minutes at 150°C. In this work, the PDMS is cured at room temperature for 48 hours or in an oven at 55°C for 4 hours. Once the PDMS is cured (transformed into a stable solid elastomer), the top wafer is carefully removed. The PDMS replica (negative of master) is peeled off from the SU-8 master and unwanted PDMS is cut off with a scalpel. The SU-8 master and the top Si wafer is coated with Teflon-like fluoropolymer using plasma deposition. This fluoropolymer layer prevents



the bonding of the PDMS to the master and the top wafer and facilitates the release of the PDMS replica from the mould.

#### 4.3.5 SU-8 master fabrication

It is a common practice to use SU-8 for fabricating master for PDMS replica moulding [134]. SU-8 is a commercially available epoxy based photoresist. SU-8 is a negative photoresist, which implies that the exposed and subsequently cross-linked parts of SU-8 are rendered insoluble to liquid developers. The cross-linking upon exposure proceeds in two steps: (1) formation of a strong acid during the exposure process followed by (2) acid-initiated, thermally driven epoxy cross-linking during the post exposure bake (PEB) step [135]. SU-8 (MicroChem Corp.) is available in different formulations ranging from SU-8 2 to SU-8 100, each corresponding to a particular viscosity and maximum thickness achievable with a single coat for a standard spin rotation. Film thickness up to 2mm thick with multiple coatings [136] and aspect ratio over 25:1 are achievable with SU-8 [137]. In this work, the master has been fabricated using multi-layer SU-8 fabrication technique [137] in which each layer undergoes softbake, exposure and PEB but the all layers are developed simultaneously at the end. Three SU-8 masters were fabricated to mould PDMS covers with the following dimensions:


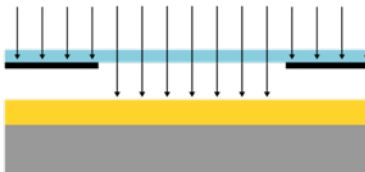

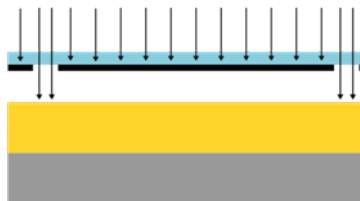


- i. Compartment height of 30 $\mu$ m and membrane thickness of 270 $\mu$ m
- ii. Compartment height of 30 $\mu$ m and membrane thickness of 100 $\mu$ m, and
- iii. Compartment height and membrane thickness of 50 $\mu$ m.

The fabrication steps and the process parameters used in the fabrication of these SU-8 masters are presented in Table 4.1 (page 76) and 4.2 respectively. In table 4.2, the exposure is mentioned in terms of time instead of the more meaningful parameter of exposure dose since the mask aligner used in the work is not calibrated.

**Table 4.2 Process parameters for fabrication of SU-8 master**

	Resist	Thickness ( $\mu$ m)	Spinning speed (rpm)	Softbake at 65°C (Min)	Softbake at 95°C (Min)	Exposure (sec)	Post exposure bake at 95°C (min)
Layer 1	SU-8 50	30	6000	5	12	20	12
	SU-8 50	50	3000	5	15	25	15
Layer 2	SU-8 50	50	3000	5	15	25	15
	SU-8 50	100	1500	15	30	50	10
	SU-8 100	270	1500	25	150	70	40

**Table 4.1 Fabrication steps of SU-8 Master**

Step No.	Process Steps	
<div><div><div>Legend</div><div><div><div>SU-8</div><div>Mask - transparent region</div></div><div><div>Silicon</div><div>Mask - opaque region</div></div><div><div>Plasma deposited fluoropolymer</div></div></div></div></div>		
1.	Silicon wafer was cleaned with RCA solution followed by a dip in buffered HF solution, which is meant to improve adhesion. First layer of SU8 is spun on the wafer and softbaked on a hotplate. The first layer of SU8 defines the height of the PDMS compartment which corresponds to the height of the cathode. The layer thickness is either 30 μm or 50μm.	
2.	First layer of SU8 is exposed and subjected to post exposure bake (PEB).	
3.	Second layer of SU8 is spin coated on top of the first layer without developing the first layer. After spin coating, the second layer is softbaked on a hotplate. The thickness of the second layer of SU8 defines the thickness of the PDMS membrane.	
4.	SU8 multilayer is exposed with Karl Süss MA6 mask aligner and post exposure bake is done on a hotplate.	
5.	SU8 is developed in a commercially available SU8 developer. The development takes about 10 to 30 minutes depending on layer thickness. However, as the structures are relatively large, development time is not critical.	
6.	The SU8 master is coated with Teflon like fluoropolymer using plasma deposition.	

#### **4.3.6 PDMS membrane bonding**











The PDMS cover/membrane fabricated with moulding must be bonded with the Si substrate supporting the electrodes to complete the fabrication of SC- $\mu$ DGFC. The PDMS cover is permanently bonded to the Si substrate using oxygen plasma assisted bonding. The PDMS cover is exposed to oxygen plasma for 1 minute. This improves the adhesiveness of PDMS by removing surface contaminates and altering the surface chemistry. Oxygen plasma treatment generates silanol groups (Si-OH) on the surface of the PDMS by the oxidation of methyl groups (PDMS surface chemistry changes from hydrophobic to hydrophilic). Surface oxidized PDMS can be irreversibly bonded to a number of substrates including itself, glass, Si, SiO<sub>2</sub>, silicon nitrate, quartz, polystyrene and polyethylene [112,138]. The second surface may also have to be exposed to oxygen plasma. However, in this work, the Si substrate is not exposed to oxygen plasma as this may oxidize the catalysts and render them inactive during fuel cell operation.

The bonding process requires some manual dexterity. After oxygen plasma treatment of PDMS, the two surfaces must be brought into intimate contact quickly (<10 min) and the cover must be aligned with the underlying interdigitating comb electrode structures. The bond strength increases over several hours until it becomes irreversible.

#### **4.3.7 Complete fabrication process**

The essential microfabrication technologies used in the fabrication of SC- $\mu$ DGFC have been explained in the preceding sections. This will facilitate the understanding of the whole fabrication process of SC- $\mu$ DGFC which is presented in Table 4.3.

**Table 4.3 Fabrication Steps of SC- $\mu$ DGFC**

Legend	 Silicon	 Silicon Dioxide	 Copper seed layer	 Chromium	 Titanium
	 Photoresist	 Copper electrode	 Nickel/Platinum	 Silver	 PDMS
Step No.	Process Step				
1.	300 to 400 nm thick silicon dioxide is deposited on the Si wafer by PECVD. Alternately, the wafer can be thermally oxidized to form a 1 $\mu$ m thick thermal oxide layer. The purpose of oxide layer is to electrically insulate the anode and cathode from each other.				
2.	Cu seed layer (electroplating base) is deposited on the wafer. The seed layer is 120 - 200 nm in thickness and is deposited by sputtering or E-beam evaporation. Before Cu film is deposited, a 10-15nm intermediate layer of Ti or Cr is deposited to improve the adhesion between Cu and SiO <sub>2</sub> .				
3.	The current collectors and the contact pads are defined in the seed layer. To define the current collector and contact pads, Ti is deposited by the lift off process. The process starts by lithography as show in the corresponding figure. <i>Positive photoresist (AZ5214) is spun at 4000 rpm for 30 seconds to obtain a resist thickness of 1.4<math>\mu</math>m. The resist is softbaked in an oven for 20 minutes at 93°C or it can be softbaked on a hotplate at 100°C for 1 minute. The exposure time is 3 seconds and the development takes 50 seconds in AZ351B developer (1:4).</i>				
4.	Ti is deposited by sputtering or E-beam evaporation. The thickness is 25 – 40 nm.				
5.	Dissolution of photoresist and lift-off of unwanted Ti by immersion in acetone. The process takes ca. 15 minutes with ultrasound agitation. The wafer is further cleaned with isopropanol and ultrasound agitation for 15 minutes. Ti will act as a hard mask to protect the underlying Cu during seed layer etching.				
6.	<p>Photolithography of AZ4562 photoresist to form the mould for anode fabrication by electroplating. The parameters for this process are:</p> <p><i>Resist spinning: 5000 rpm for 30 seconds</i></p> <p><i>Softbake: 100°C for 5 minutes on a hotplate</i></p> <p><i>Rehydration time: 1-2 hours</i></p> <p><i>Exposure: 12 seconds; hard contact mode</i></p> <p><i>Development time: 3-4 minutes; AZ351B developer diluted in DIW (1:4)</i></p> <p><i>Resist thickness: ca. 5.3 <math>\mu</math>m</i></p> <p>The photoresist is exposed to O<sub>2</sub> plasma for 30-45 seconds to remove resist residues and inorganic contaminants from the seed layer.</p>				

<b>Legend</b>	 Silicon	 Silicon Dioxide	 Copper seed layer	 Chromium	 Titanium
	 Photoresist	 Copper electrode	 Nickel/Platinum	 Silver	 PDMS

7. Electroplating through photoresist mask to form the anode.  
Electroplating parameters are:  
*Plating area: ca.  $7.66 \text{ cm}^2$*   
*Plating current: 153mA*  
*Current density:  $20 \text{ mA/cm}^2$*   
*Rate:  $0.5 \mu\text{m/min}$ .*



8. Anode catalyst (Pt or Ni) is deposited using lift off process. In case of Ni E-beam evaporator is used, whereas Pt is sputtered. The thickness of the catalyst layer is 80-90nm.



9. The thick resist is stripped with acetone and isopropanol. The sample is immersed in acetone and isopropanol for 15 minutes each with ultrasound agitation. It was observed that retrograde sidewall profile is not essential for the lift off process to succeed in case of AZ4562



10. Photolithography of AZ4562 photoresist to form the mould for fabricating cathode by copper electroplating. Cathodes comb electrode fingers were either ca. 30 or 50  $\mu\text{m}$  high using single or multiple coating.

**The parameters for fabricating 34  $\mu\text{m}$  high cathode mould by single coating are:**

*Resist spinning: 100 rpm ( chuck acceleration 500rpm/sec) for 0.5 seconds followed by main spin: 1800 rpm (chuck acceleration 900rpm/sec) for 3 seconds*  
*Softbake: 60 to 98 °C in 4 minutes; at 98°C for 30 minutes on a hotplate*

*Rehydration time: ca. 10 hours;*

*Exposure: Multiple exposure in low vacuum contact mode, 2 cycles of 90 seconds exposure with 90 seconds delay between exposures*

*Development time: 12-15 minutes with AZ351B developer, diluted in DIW (1:4)*

*Resist thickness : ca. 34.4  $\mu\text{m}$*

**The parameters for fabricating 52  $\mu\text{m}$  high photoresist mould:**

*First coat : 100 rpm (500rpm/sec acceleration) for 0.5 seconds followed by main spin: 2000 rpm for 3 seconds (chuck acceleration 900rpm/sec)*

*Intermediate Softbake: 60°C for 5 minutes; at 98°C for 5 minutes on a hotplate*

*Second coat : 100 rpm (500rpm/sec acceleration) for 0.5 seconds followed by main spin: 2000 rpm for 3 seconds (chuck acceleration 900rpm/sec)*

*Relaxation time: 15 - 20 minutes*

*Softbake: 60°C for 5 minutes and 98°C for 50 minutes*

*Rehydration time: ca. 12 -24 hours*

*Exposure: Multiple exposure in low vacuum contact mode, 2 cycles of 120 seconds exposure with 100 seconds delay between exposures*

*Development time: ca. 30-35 minutes with AZ351B developer, diluted in DIW (1:4)*

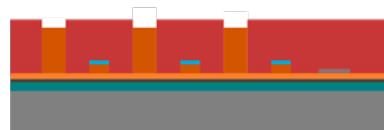
*Resist thickness : ca. 52  $\mu\text{m}$*



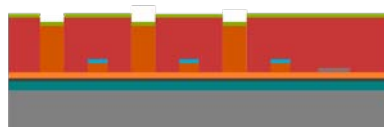
**Legend**

	Silicon		Silicon Dioxide		Copper seed layer		Chromium		Titanium
	Photoresist		Copper electrode		Nickel/Platinum		Silver		PDMS

- 11.** Electroplating through photoresist mask to form the anode.  
Electroplating parameters are:  
*Plating area: ca.  $7.66 \text{ cm}^2$*   
*Plating current: 153mA*  
*Current density:  $20 \text{ mA/cm}^2$*   
*Rate:  $0.5 \mu\text{m/min}$ .*



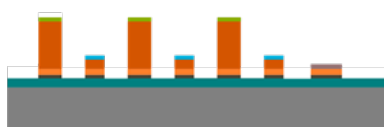
- 12.** Ag is deposited by E-beam evaporation process. The thickness of the Ag film is ca. 80-90 nm.



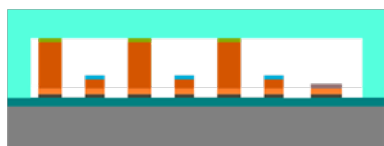
- 13.** Lift-off process for selective deposition of Ag. The resist is removed with acetone and isopropanol in combination with mild ultrasound agitation.



- 14.** Copper seed layer is etched using the Cr etch solution mentioned in Section 4.3.3. The underlying Cr or Ti adhesion promotion layer is not etched by the Cr etch solution. Cr is etched by a concentrated HCl acid. In case of Ti layer, diluted HF acid (5ml HF in 120ml DIW) is used as the etchant.



- 15.** PDMS membrane is exposed to oxygen plasma for one minute and then attached to the fuel cell. A temporary bond is formed at the  $\text{SiO}_2$  – PDMS interface, which becomes permanent after a few hours.



# Chapter 5

## Results and Discussion

---

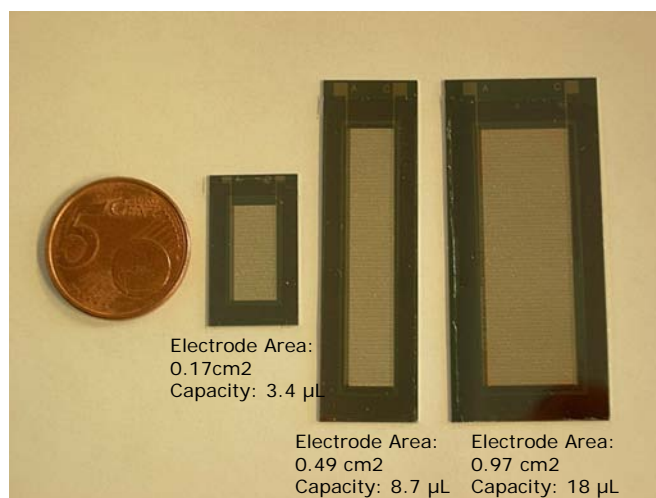
### 5.1 Overview

In this chapter the fabrication and performance of the SC- $\mu$ DGFC is evaluated. Results are presented for different stages of the fabrication process and key issues encountered during these stages are discussed. The SC- $\mu$ DGFCs were not only tested for glucose but also for ethanol. The results of these tests are presented in this chapter and their performance analyzed.

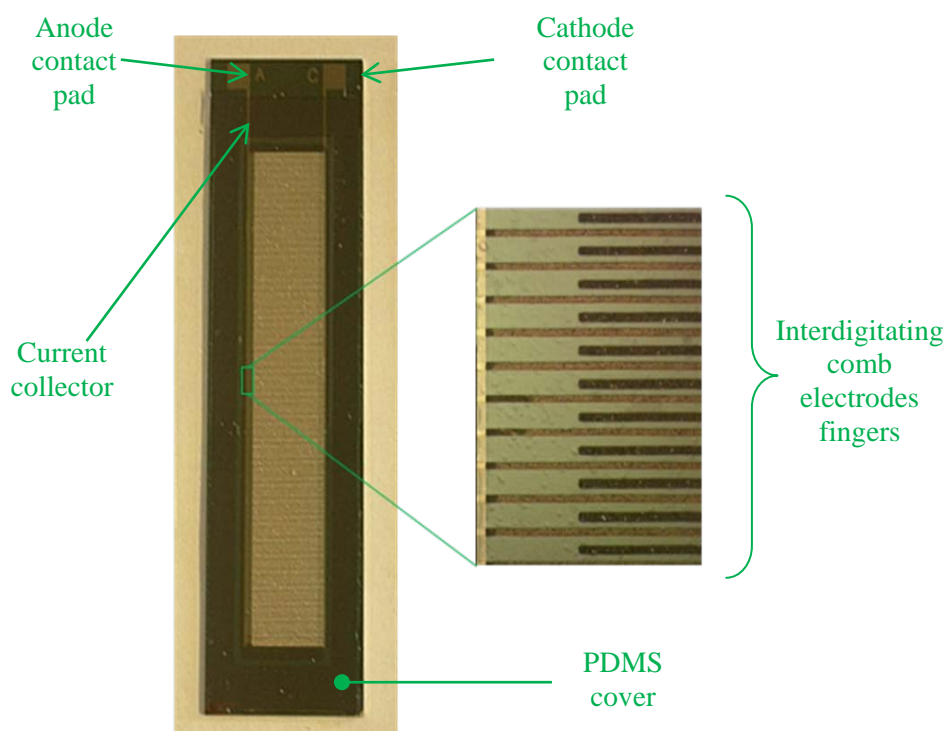
### 5.2 Fabrication results

Most of the processes for fabricating the SC- $\mu$ DGFCs were carried out in an ISO class 5 cleanroom. Copper electroplating, nickel deposition by evaporation, PDMS moulding and dicing of the wafer was performed outside the cleanroom. The fabricated SC- $\mu$ DGFCs are shown in Figure 5.1. Three different sizes of fuel cell were fabricated: small (2.2 x 1.25 cm), medium (5 x 1.35 cm) and large (5 x 2.2 cm). Individual components of the SC- $\mu$ DGFC are highlighted in Figure 5.2.

The layout of a 4 inch Si wafer used in fabricating SC- $\mu$ DGFC chips is shown in Figure 5.3. This simple layout facilitates the wafer dicing process. Figure 5.3 also shows the 5mm wide outer rim of Si wafer that cannot be utilized due to the formation and subsequent removal of the AZ4562 edge bead.

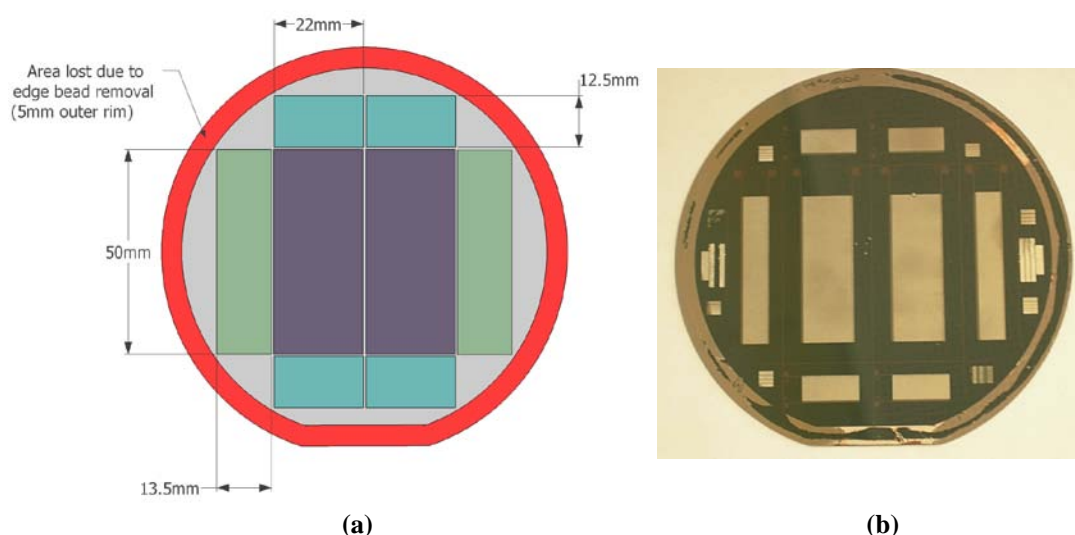


**Figure 5.1** Fabricated SC-μDGFCs of three different sizes with volumes for 31 μm high cathodes.



**Figure 5.2** Components of a SC-μDGFC.





**Figure 5.3 (a) and (b)** Layout of a 4 inch silicon wafer used to fabricate the SC- $\mu$ DGFC chips. Each wafer accommodates four small fuel cells of dimension  $2.2 \times 1.25$  cm, two medium sized fuel cell of dimensions  $5 \times 1.35$  cm and two large fuel cells of dimensions  $5 \times 2.2$  cm.

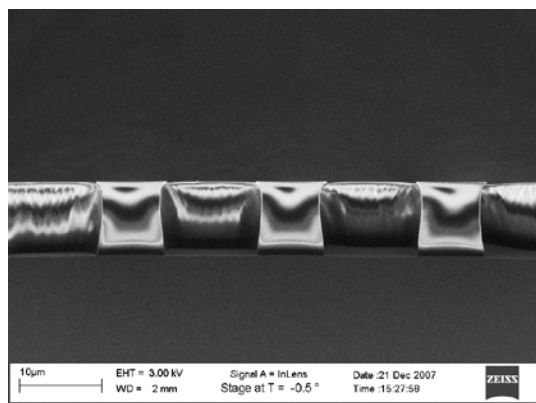
Photomasks printed on plastic film were used for the photolithography process. The photomasks were drawn using LAYED (Catena Software GmbH) computer aided design tool. The minimum achievable line width for plastic photomasks ranges from 15 to  $30\mu\text{m}$  depending on the printer (vendor). Keeping this fact in mind, the line width of each electrode finger is set to be  $30\mu\text{m}$ . However, the plastic mask obtained from the printer had electrode fingers with width of  $23\mu\text{m}$  due to production problems at the mask vendor. The distance between an anode finger and the adjacent cathode finger is designed to be  $30\mu\text{m}$ . The current collector lines connecting the electrode fingers to each other and to the contact pad are  $250\mu\text{m}$  wide.

Key issues related to the fabrication of the SC- $\mu$ DGFCs are addressed in the following subsections.

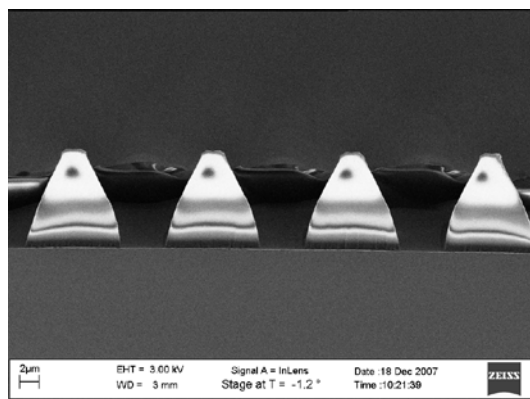
### 5.2.1 AZ4562 processing

As discussed in Section 4.3.1, the side wall profile of the comb electrode fingers depends on the profile of the AZ4562 resist mould. The impact of different contact modes between the photomask and wafer during exposure can be seen in Figure 5.4(a) and (b). The vacuum contact mode (Figure 5.4(a)) leads to wall profiles with undercut below the surface of the resist. The undercut is beneficial in deposition of metals on the electroplated copper as unwanted deposition on the sidewall is blocked by the undercut

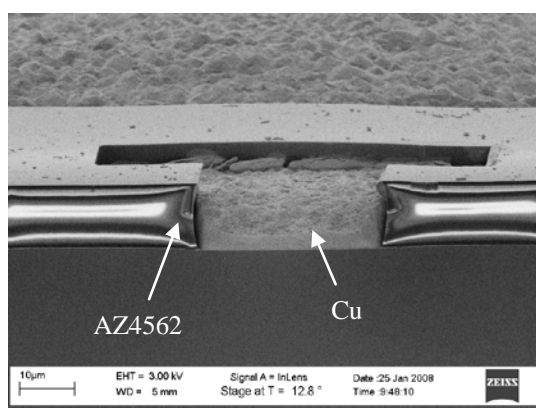
(Figure 5.4 (c)). Using soft contact mode will lead to inclined sidewalls profile as shown in Figure 5.4(b).



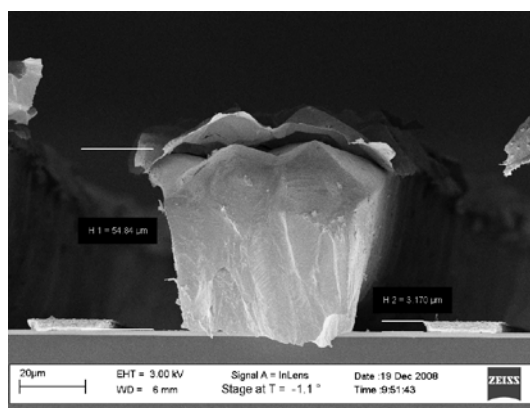
(a)



(b)



(c)



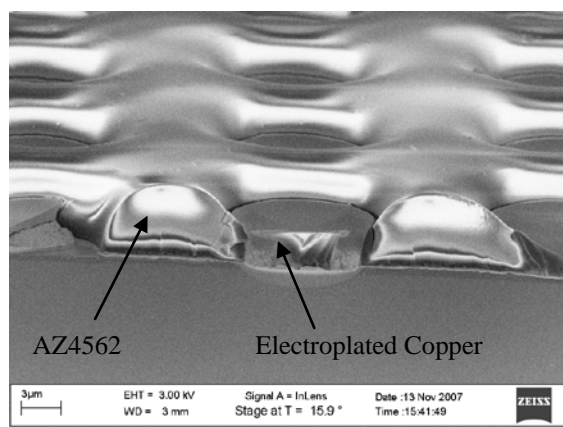
(d)

**Figure 5.4** (a) AZ4562 exposed using vacuum contact mode. (b) Inclined sidewall profile obtained using soft contact mode. (c) Pt deposited on copper electroplated using AZ4562 mold with undercut (d) widening of the patterns due to a long development time caused by a long softbake. The electroplated Cu follows the shape of the resist mould.

Though the contact mode during exposure is important, it is not as critical as the softbake time and temperature. It was observed that too long softbake time resulted in very long development times and extremely inclined sidewalls with widened patterns. The widening of the pattern is associated with significant dark erosion during development. Figure 5.4(d) shows a cathode comb electrode finger in between two anode electrode fingers. During the processing of ca. 52µm thick AZ4562 (obtained by double coating) for fabricating this cathode comb electrode, the resist was softbaked for 70 minutes at 100°C, and was exposed using 5 exposure cycles; each with exposure time of 100 seconds and delay of 60 seconds between exposures. The softbake time was

too long, which resulted in a very long development time of 3 hours and 20 minutes. The long development time resulted in significant erosion of unexposed areas, resulting in widening of the cathode finger. The width of the cathode finger should be equal to the width of the anode finger (ca.  $23\mu\text{m}$ ). However, in this case it is almost twice the width of the anode. The optimized parameters for coating  $31\mu\text{m}$  and  $52\mu\text{m}$  AZ4562 resists have already been mentioned in Section 4.3.7.

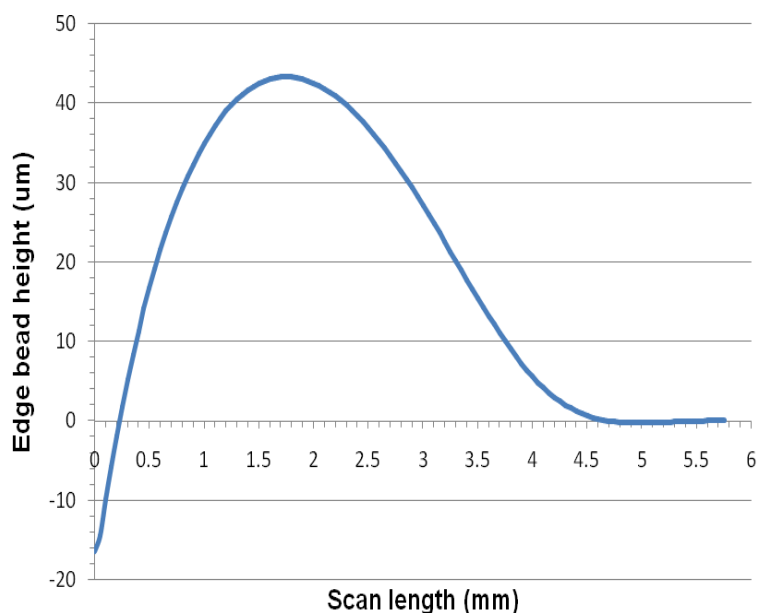
To protect the photoresist from the electroplating bath solution, it can be hard baked in an oven at  $120^\circ\text{C}$  for ca. 15-20 minutes. When an AZ4562 sample was hard baked before electroplating, it was observed that the resist patterns shape changed. This happens because the resist softens during the hard bake and reflows. The hard bake was evaluated to be a redundant step since AZ4562 is chemically stable in the plating bath solution.



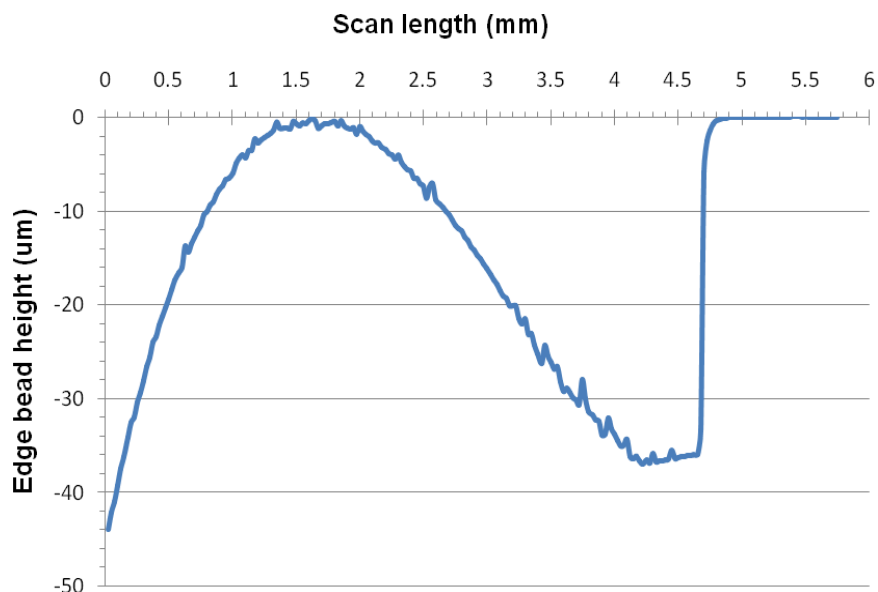
**Figure 5.5** AZ4562 reflows when it is hard baked in an oven at  $120^\circ\text{C}$ .

Vacuum contact mode was evaluated to be the best option for obtaining near vertical side walls. However, the formation of edge bead introduced an unwanted proximity gap between the photomask and the wafer. The thickness of the resist at the edge for some samples was found to be twice as thick as the resist in the centre of the wafer. The width of the rim formed by the edge bead was ca. 5 mm. The edge bead was removed by photolithography. 5mm wide outer rim of the wafer was exposed and the edge bead was reduced by subsequent development. It is preferred not to completely remove all photoresist from the edge but to only reduce its thickness to a level where it is equal to the photoresist film on the rest of the wafer. Figure 5.6 shows the profile of edge bead formed when a  $52\mu\text{m}$  thick AZ4562 film is coated. This bead was removed by

photolithography (100 second exposure and 12 minute development) and the resulting profile of the resist at the edge after development is shown in Figure 5.7.



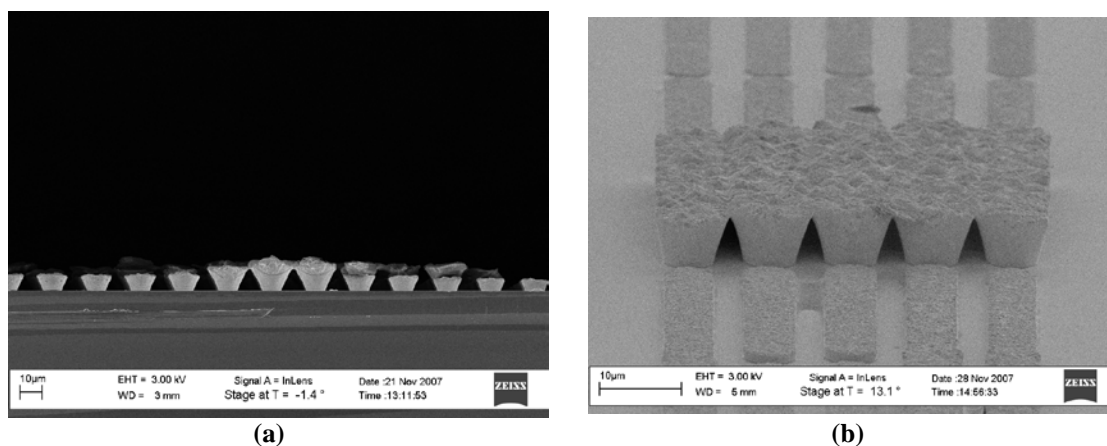
**Figure 5.6** AZ4562 film profile at the edge of the wafer measured with a profilometer. The wafer edge begins at zero mark on the horizontal axis, whereas zero on the vertical axis corresponds to planar surface of the photoresist film outside the edge bead region.



**Figure 5.7** AZ4562 film profile at the edge after the edge bead has been reduced using photo-lithography. The wafer edge begins at zero mark on the horizontal axis, whereas zero on the vertical axis corresponds to planar surface of the photoresist film outside the edge bead region.

### 5.2.2 Electrode electroplating

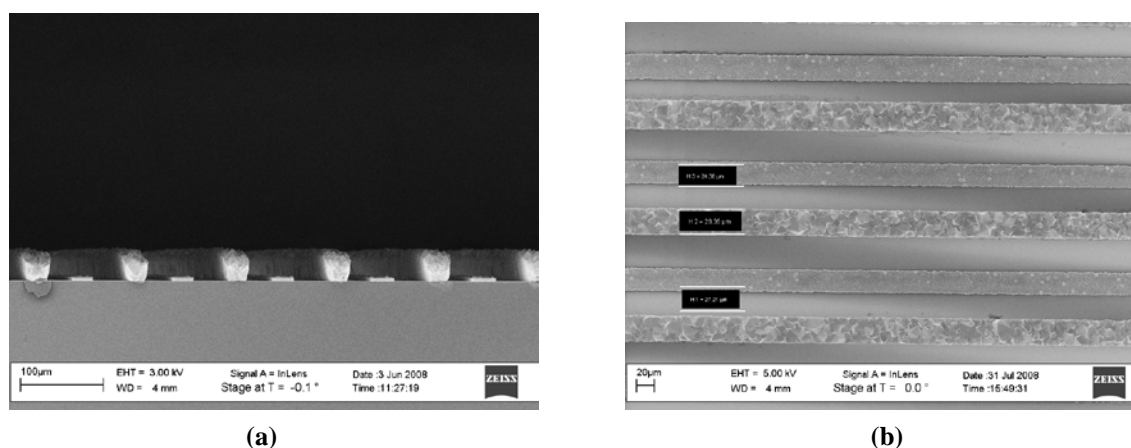
Parameters for electroplating process like electroplating bath composition, current density and Cu seed layer surface treatments were studied before the process was used to fabricate the comb electrodes. The composition of the plating bath used in the initial tests was 75 g/L of copper sulphate pentahydrate ( $\text{CuSO}_4 \cdot 5\text{H}_2\text{O}$ ), 190g/L of sulphuric acid ( $\text{H}_2\text{SO}_4$ ) and 150 mg/L of hydrochloric acid (HCl). The current density values ranged from 10 to 20  $\text{mA}/\text{cm}^2$ . In the initial tests, the seed layer was not subjected to any surface treatment. Some results from the initial tests are shown in Figure 5.8. The electroplated structures exhibited large non-uniformity in thickness over the entire wafer. This indicates that the depositing Cu film does not grow at the same rate on all the patterns in the photoresist mould. Possible reasons for this “pattern-scale” non uniformity in thickness are: (i) high concentration of copper, (ii) high current density, (iii) mass transfer kinetics dependent on electroplating cell geometry, (iv) limited wettability of the seed layer, (v) contaminants on the seed layer that inhibit electrodeposition, and (vi) the arrangement, density and geometry of the patterns on the photoresist mould [131,132,139].



**Figure 5.8 (a) & (b)** Non uniformity in the height of electrodeposited microstructures.

Changes were made to the electroplating process in order to improve the uniformity of deposition. The Cu concentration was reduced by reducing the concentration of  $\text{CuSO}_4 \cdot 5\text{H}_2\text{O}$  to 60 gm/L. The concentration of  $\text{H}_2\text{SO}_4$  was increased to 230gm/L. A higher concentration of  $\text{H}_2\text{SO}_4$  helps in minimizing the variations in thickness uniformity arising from the electroplating cell geometry [132]. To improve the wetting of the seed layer, the wafer was dipped in DIW for a minute before it was placed

in the electroplater. The Cu electroplater also has a routine to improve wetting. The electrolyte flow in the electroplater runs for three short durations before the current is applied. This cycle is meant to properly wet the seed layer. The seed layer was also subjected to surface treatments before electroplating. The seed layer was exposed to oxygen plasma for 30 - 45 seconds to remove the resist residues and organic contaminants from its surface. Oxygen plasma treatment was found to be very effective in improving the uniformity of deposition. After oxygen plasma treatment, the native copper oxide from the seed layer was removed by dipping the wafer in 10% nitric acid for 10 seconds. However, etching the copper oxide in nitric acid was found to be a redundant process step as the electrolyte solution itself can effectively etch the copper oxide. The current density for plating was set to be  $20\text{mA}/\text{cm}^2$ , which is a good compromise between good thickness uniformity and reasonable deposition rate of ca.  $0.45 - 0.55\mu\text{m}/\text{min}$ . The above mentioned changes in electroplating process significantly improved the uniformity of the electrodeposition and reduced the number

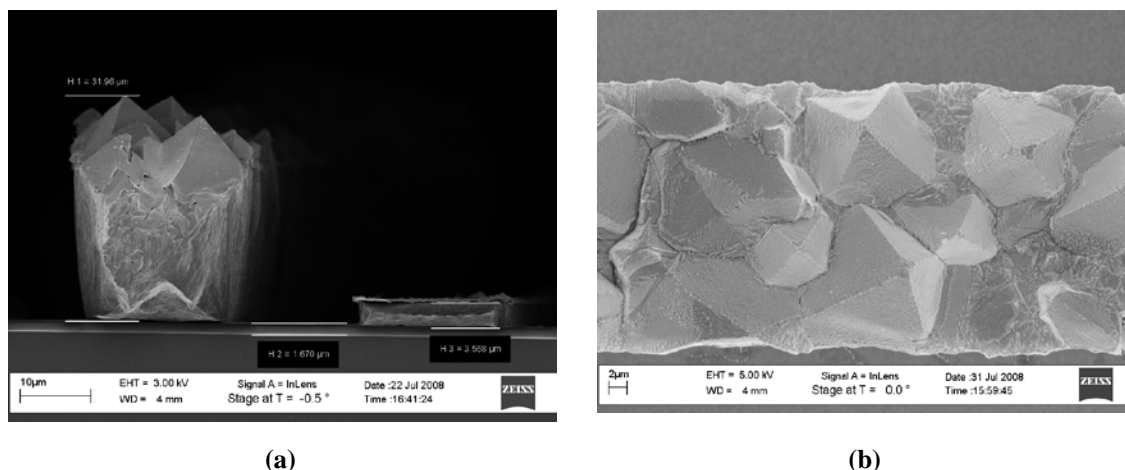


**Figure 5.9** SEM image of (a) cross sectional and (b) top view of comb electrodes of SC- $\mu$ DGFC.

Each electrode finger is  $25\mu\text{m}$  wide and the gap between two adjacent anode and cathode comb electrode fingers is  $27\mu\text{m}$ .

of voids (patterns with no electrodeposited Cu). Figure 5.9(a) shows the electrodeposited electrode comb fingers with good height uniformity at the pattern scale. The uniformity of the deposition across the wafer depends on the pattern spacing and geometry [139]. The test photomask used during the initial testing had features of different sizes, density and spacing. The variations on this photomask were very large with the smallest feature size in the range of  $5\text{-}10\mu\text{m}$  and the maximum feature as wide as  $1\text{mm}$  and running across the entire wafer. In contrast, the masks for the anode and cathode comb electrode

fingers have patterns of uniform sizes and spacing as shown in Figure 5.9(b). It was observed that the uniform geometry of the comb electrodes plays a major role in improving the uniformity of the electrodeposition.

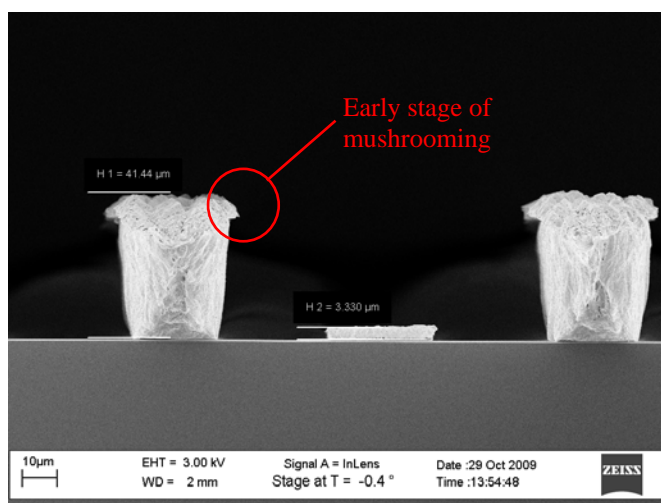


**Figure 5.10** (a) SEM image of cross sectional view of anode and cathode finger. The pyramid shaped mounds on the cathode are visible. (b) SEM image of the top view of the pyramidal mounds on the surface of the cathode finger.

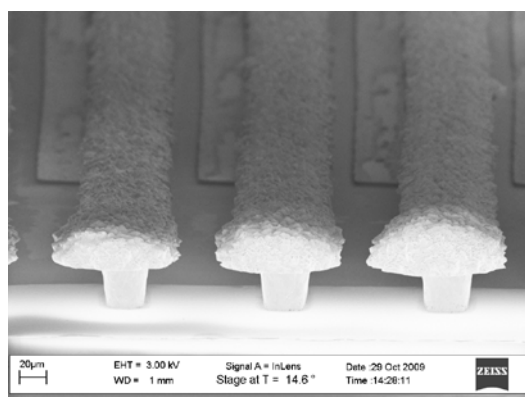
In the above discussion, the thickness distribution of the electrodeposition is discussed at the “macro” pattern scale and the surface morphology of individual features is not considered. The surface of the electrodeposited Cu was not planar, which was expected as no additives were used in the electroplating bath solution [132, 140]. The roughness in the surface of the electrodeposited Cu was more prominent for the cathode comb electrode fingers. The surface of cathode had large pyramidal mounds as shown in Figure 5.10 and 5.13(b). At the molecular scale, the pyramidal mounds are formed of series of steps (terraces). The formation of the pyramidal mounds is primarily ascribed to the Schwoebel effect [140-142]. According to the Schwoebel effect, the diffusing adatoms will face a resistance to the step-down diffusion. The resistance arises from the potential barrier that exists at the edge of the step and it will most likely reflect the atom upwards. Hence, the diffusing atoms have a tendency to ascend steps rather than to descend steps. In addition to the Schwoebel effect, short-range attraction of the surface adatoms to the ascending steps also causes mounding [141]. As the electrodeposition progresses, the mounds size increases with time and eventually coalescence occurs. The coalescing of neighbouring mounds creates larger mounds which become bigger and steeper with time, decreasing the empty area between as well as the total number of

mounds on the surface [141]. More information on formation of pyramidal mounds can be found in [140] and [141].

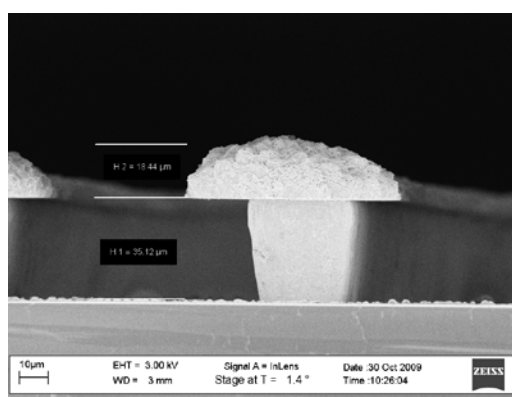
When electrodeposition height is greater than the photoresist mask thickness, the deposition will proceed in the lateral direction as well as vertical. This phenomenon is referred to as mushrooming. To avoid mushrooming, the electrodeposition in progress is interrupted to monitor the height of the structures with a profilometer. The height of the deposit can also be predicted since the electroplating rate is known. The deposition rate was usually in the range of 0.45 to 0.55  $\mu\text{m}/\text{min}$ . However, there were samples which exhibited non-uniformity in deposition and lead to mushrooming on same parts of the sample. Figure 5.11 and 5.12 show the progression of mushrooming at the beginning and advance stage respectively.



**Figure 5.11** SEM image of cross sectional view of comb electrode fingers showing early signs of mushrooming for the cathode fingers.



(a)



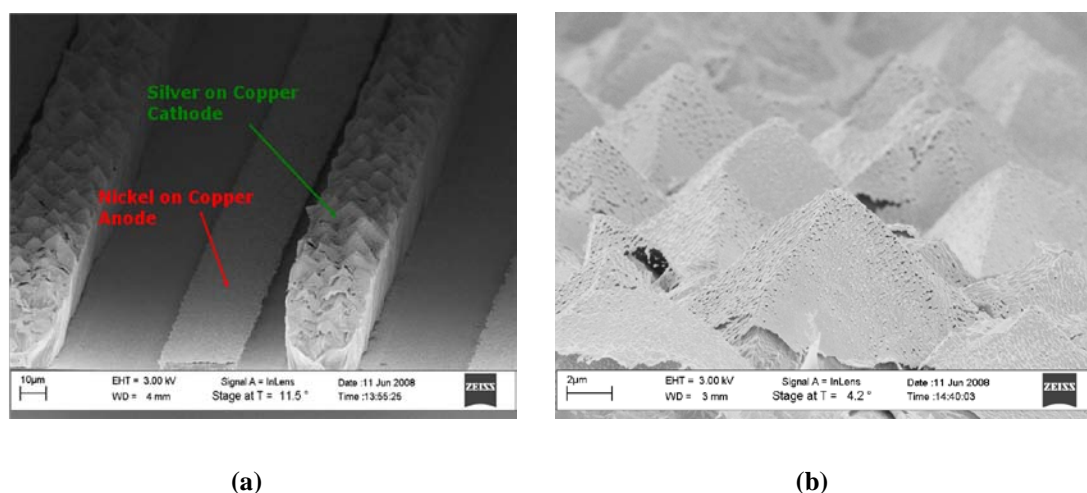
(b)

**Figure 5.12** SEM images of cross sectional view of comb electrode fingers with excessive mushrooming.

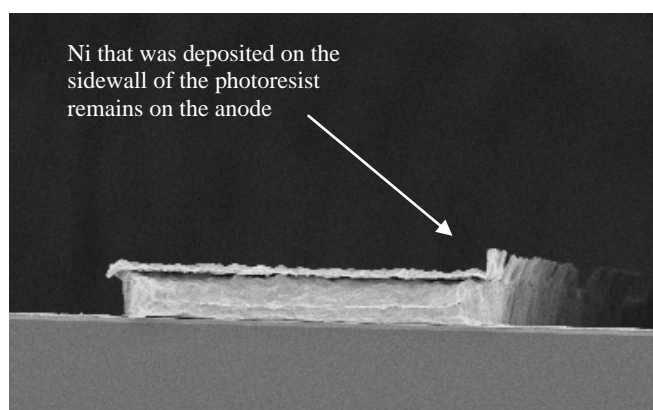


### 5.2.3 Catalyst Deposition

Ni and Ag are deposited using E-beam evaporation. Later, Ni was replaced by Pt, which is deposited using sputtering system. Before depositing the catalyst layer, the wafer is immersed in 10% nitric acid for ca. 30 seconds to remove any native oxide from the electroplated copper. The layer thickness of the catalysts ranged from 80 to 90 nm. Figure 5.13 show the catalyst deposited on the electrodes with the lift-off process. It is beneficial to have vertical or retrograde sidewall profile of the resist to minimize the metal deposition on the side wall. However, it was found that even with inclined sidewalls, lift-off of metal was easily achieved. In some cases, the metal deposited on the sidewalls of the resist remains attached to the electrode after lift-off. This is shown for an anode comb electrode finger in Figure 5.14. The free hanging catalyst film, however, does not result in device failure.



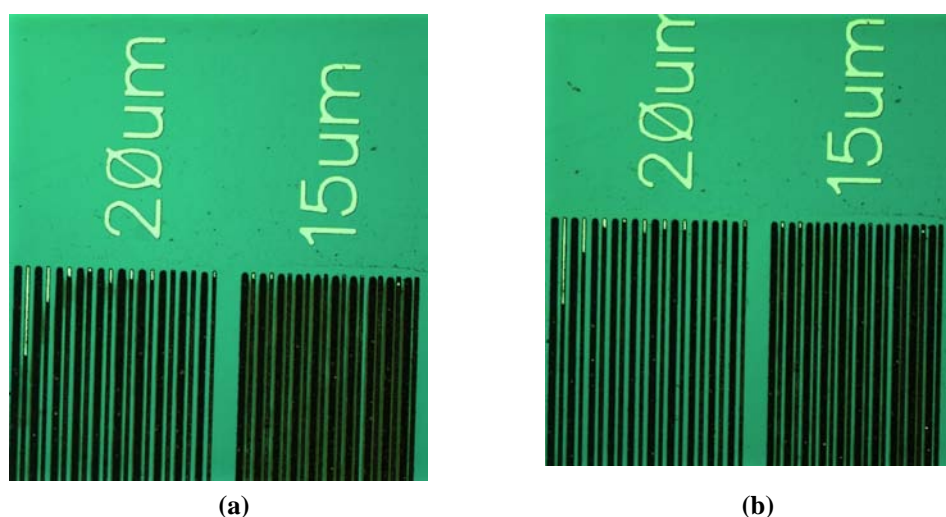
**Figure 5.13** (a) SEM image of fuel cell anode and cathode fingers with catalyst layers (b) Surface topography of cathode with silver catalyst.



**Figure 5.14** (a) SEM image of fuel cell anode finger with Ni catalyst. The Ni deposited on the sidewall of the resist remains after the lift-off process.

### 5.2.4 Seed layer etching

Cu seed layer is etched in the Cr etch solution as described in Section 4.3.3. Time to etch 150nm Cu seed layer takes ca. 60 to 120 seconds depending on the gap between the adjacent electrodes. Though, it is expected that the gap between the adjacent anode and cathode fingers should be fixed i.e.  $27\mu\text{m}$ . It was observed that the plastic photomask for photolithography had discrepancies which translated into slight misalignment and varying gap between the adjacent electrodes. The variation in the gaps was more prominent for small sized fuel cells. Figure 5.15 shows test samples etched in Cr etch solution. The numbers (15 and  $20\mu\text{m}$ ) indicate the gap between the adjacent copper fingers. 150 nm thin Cu seed layer between Cu fingers with  $20\mu\text{m}$  gap is etched in 80 seconds, whereas, the Cu in the  $15\mu\text{m}$  gap takes additional 15 seconds to etch.

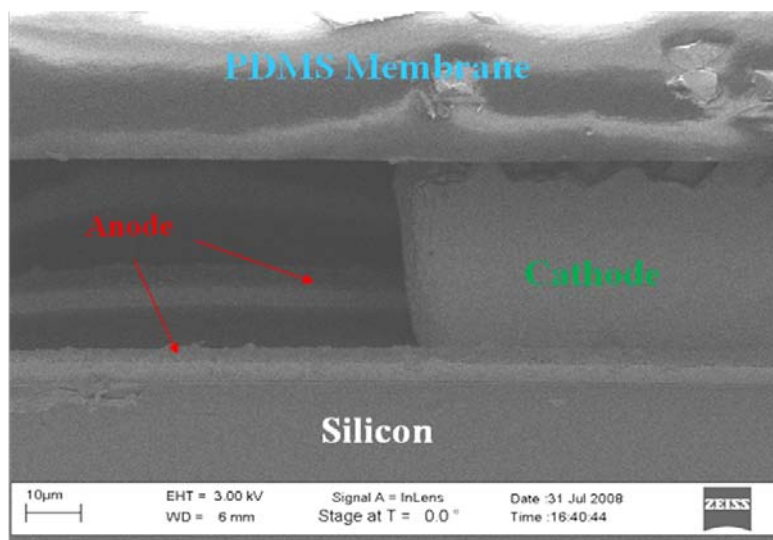


**Figure 5.15** Progress in Cu seed layer etching after (a) 80 seconds and (b) 95 seconds.

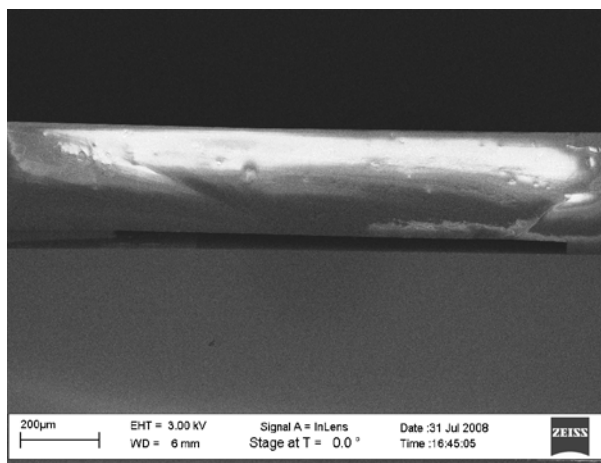
The underlying adhesion promotion layer of 15-20nm thin Cr between Cu film and  $\text{SiO}_2$  is not etched by the Cr etchant even. This is an unusual result as the cerium ammonium nitrate and perchloric acid based Cr etchant is supposed to etch Cr easily. This may be attributed to a possible electrochemical effect which hinders the etching of Cr in the Cr etchant when it is in contact with Cu or Ag is present. A similar electrochemical effect has been reported by Williams et al. [143] for a similar Cr etchant composition. They reported significantly reduction in the etch rate of Cr when it is in contact with Au. The Cr layer is etched in 37% HCl, which takes about 30 seconds for 20nm. If Ti is used for adhesion promotion, it is removed in very dilute HF, which takes ca. 20 seconds. The etching of Cr or Ti layer is monitored by measuring the sheet resistance of the substrate with 4 point probe station.

### 5.2.5 PDMS Membrane

The process for fabricating the PDMS membrane and bonding it to the Si substrate has been discussed in Section 4.3.4 and 4.3.6 respectively. Fuel cells with three different PDMS membrane thickness (50, 100 and 270  $\mu\text{m}$ ) were fabricated. Figure 5.16 and 5.17 show cross sectional SEM images a SC- $\mu$ DGFC with 270 $\mu\text{m}$  PDMS membrane.



**Figure 5.16** SEM image of cross sectional view of SC- $\mu$ DGFC.



**Figure 5.17** SEM image of cross sectional view of a SC- $\mu$ DGFC in which ca. 270 $\mu\text{m}$  thick PDMS membrane, the cell compartment and the Si substrate are visible.

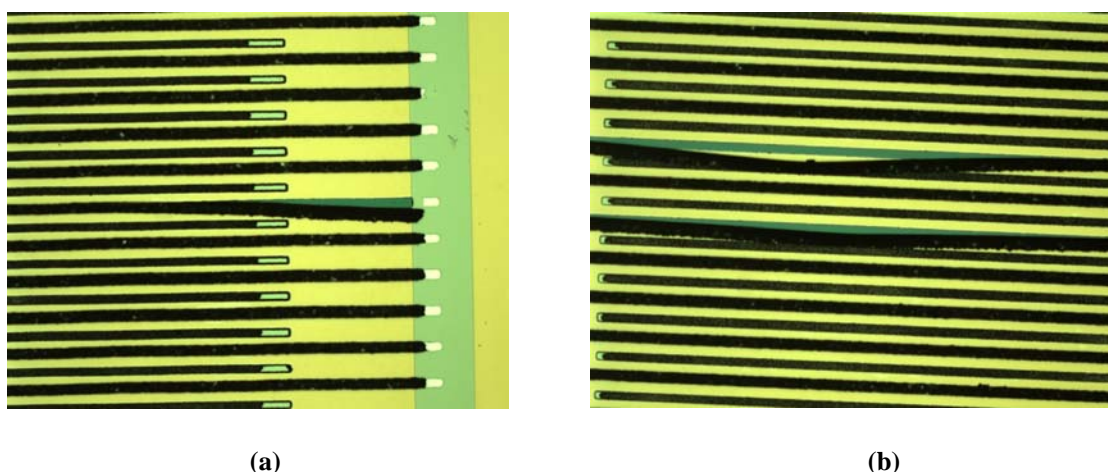
It was observed that the PDMS compartment swells/bulges out when fuel-electrolyte solution was pumped into the fuel cell. This increases the gap between the cathode surface and the PDMS membrane and lowers the performance of the fuel cell as

access of oxygen to the cathode is reduced. A possible solution to this problem is to have cathode fingers which are much higher than the height of the PDMS compartment. In this case, the cathode will be tightly pressed against the PDMS membrane which will be stretched by the cathode. This will ensure that the PDMS membrane's capacity to further stretch is reduced when fuel-electrolyte solution is pumped in. Optimum height for the cathode and the compartment would have to be evaluated for this purpose.

### 5.2.6 Defect analysis

In this section, the defects in the fabrication of some SC- $\mu$ DGFCs that lead to their failure to operate are discussed. The SC- $\mu$ DGFCs will not operate if either a short circuit exists, i.e. an electrically conductive path exists between the anode and cathode, or an open circuit exist, in which case an electrode is not electrically connected to its respective current collector.

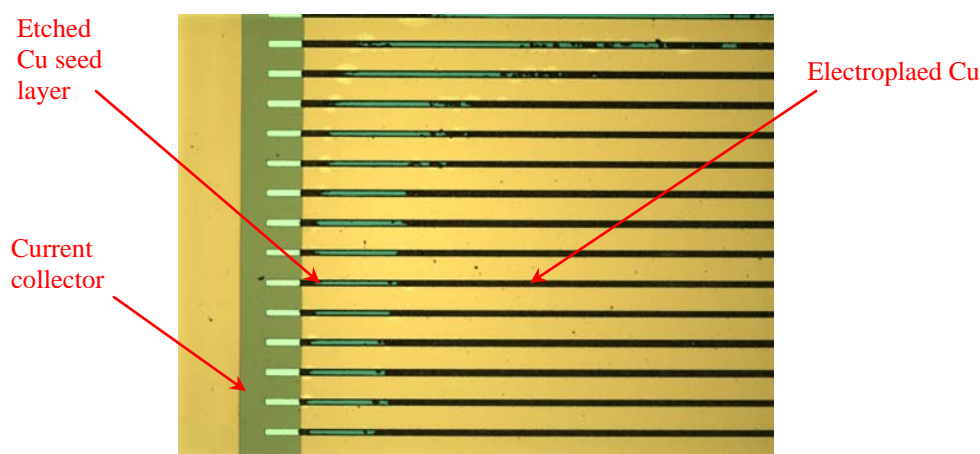
Figure 5.18 shows electrode fingers that are partially detached from the substrate. This problem was usually encountered with the cathode fingers. The partially detached fingers, in most cases, came into contact with the adjacent electrode fingers. This short circuited the fuel cells. This problem was very uncommon as most electroplated structures exhibited good adhesion to the substrate.



**Figure 5.18** Optical microscope images of electrode fingers of the SC- $\mu$ DGFC. Some cathode comb electrode fingers are partially detached from the substrate and in contact with the anode.

Before electroplating, Cu seed layer was dipped in 10% nitric acid for 10-15 seconds to remove copper native oxide from the surface. However, for a few samples, it

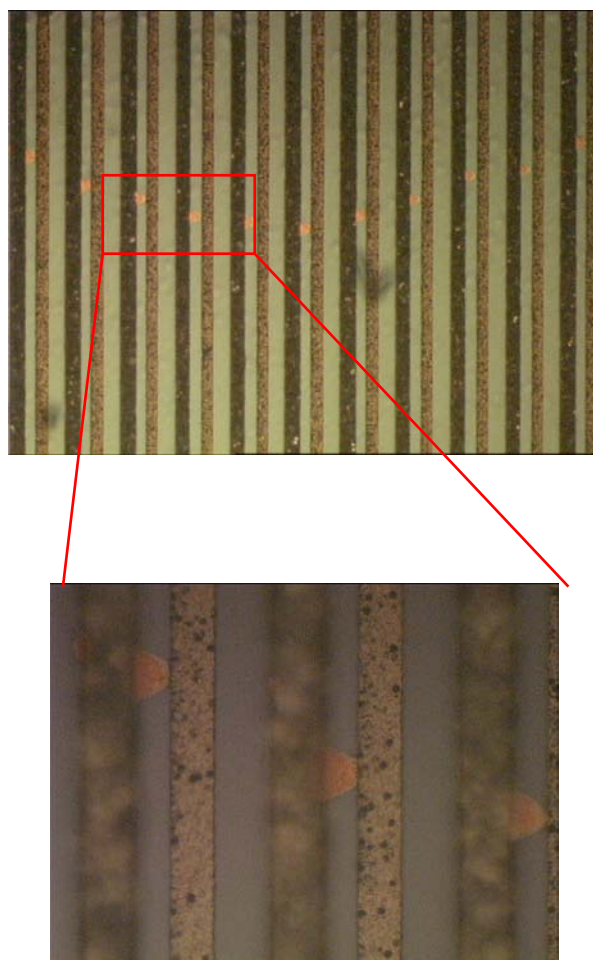
was observed that the Cu seed layer is also etched completely in the nitric acid solution. This etching proceeds from the ends of the electrode finger patterns as shown in Figure 5.19. Due to this unwanted etching, most or all electrode fingers will not remain in electrical contact with the current collector. The electroplating bath solution also acts as an etchant for copper oxide. Thus, cleaning the seed layer in the nitric acid was a redundant process step and was avoided in latter fuel cell samples.



**Figure 5.19** Optical microscope image of electrode fingers after electroplating. The parts of the seed layer that were unintentionally etched in the nitric acid do not have any electroplated copper.

Another cause for short circuiting in the fuel cells is the presence of resist residues or other contaminant on the seed layer. These contaminants will block the etching of the underlying Cu seed layer and cause the anode and cathode fingers to remain in electrical contact as show in Figure 5.20. These contaminants existed as series (or line) of spots running in direction perpendicular to the electrode fingers. Cleaning the samples in acetone and propanol prior to etching did not remove theses contaminants. To remove the spots, the etching time had to be increased to 3-4 minutes. This is not a feasible solution as prolonged etching exacerbates the peeling of the catalyst layers (discussed below). The seed layer was etched after the dicing step. The dicing process may be the source of these contaminants. A solution is to coat the wafer with thick photoresist to protect against contaminants during the dicing process.

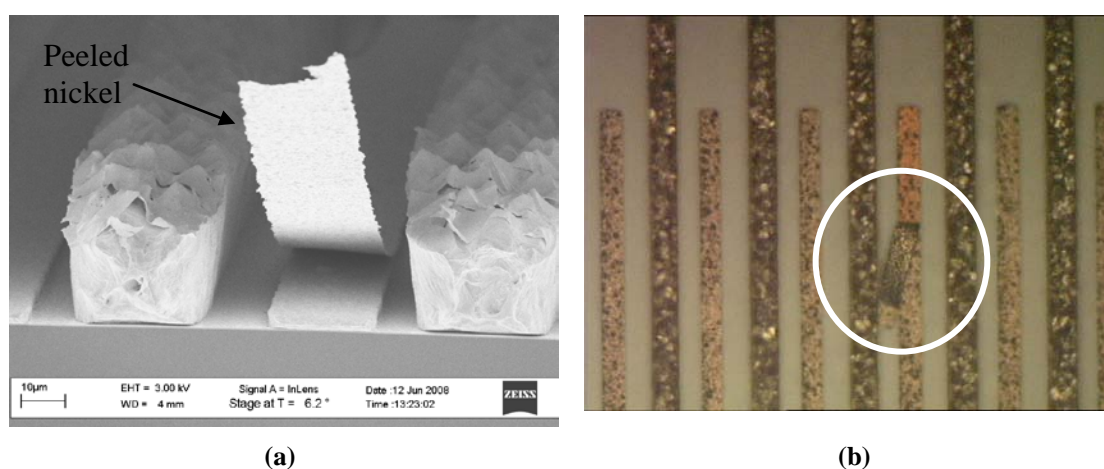




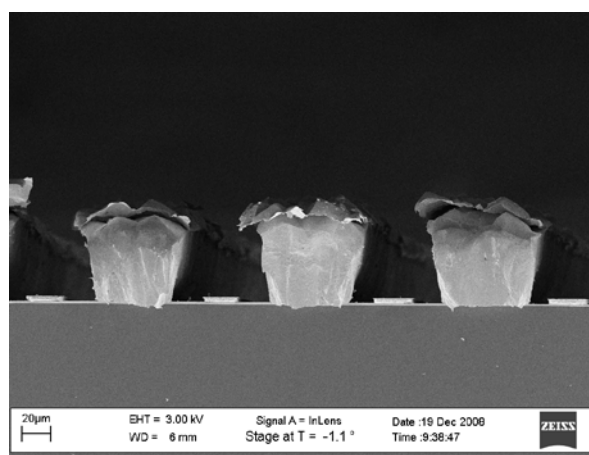
**Figure 5.20** Optical microscope images of Cu spots left on the sample after Cu seed layer is etched.

The most common reason for the failure of SC- $\mu$ DGFCs was the peeling of the catalyst layer during etching of Cu seed layer in the Cr-etchant solution. It was observed that after 45 -70 seconds in the etchant, Ni film deposited on the anode began to peel. This peeling was not only observed for Ni but also, in case of some samples, for Ag. In case of Ag, the peeling began later than Ni, usually starting after 150 seconds of being immersed in the etchant. Figure 5.21 show Ni film partially peeled from the anode. The free hanging Ni film gets in contact with the adjacent cathode, thus short circuiting the fuel cell. The peeling does not occur for Pt films. It is suspected that some electrochemical effect occurs in which the Cu immediately below the Ni or Ag film etches very quickly in the Cr-etchant solution. This hypothesis is supported by the results obtained when a test sample was etched in the Cr etchant. The result from the test is shown in Figure 5.23. The test sample was prepared using the photolithography photomasks used in the fabrication of SC- $\mu$ DGFC. A 100nm Cu seed layer was deposited on Si wafer with SiO<sub>2</sub> film. There is also a 20nm Cr adhesion promotion layer

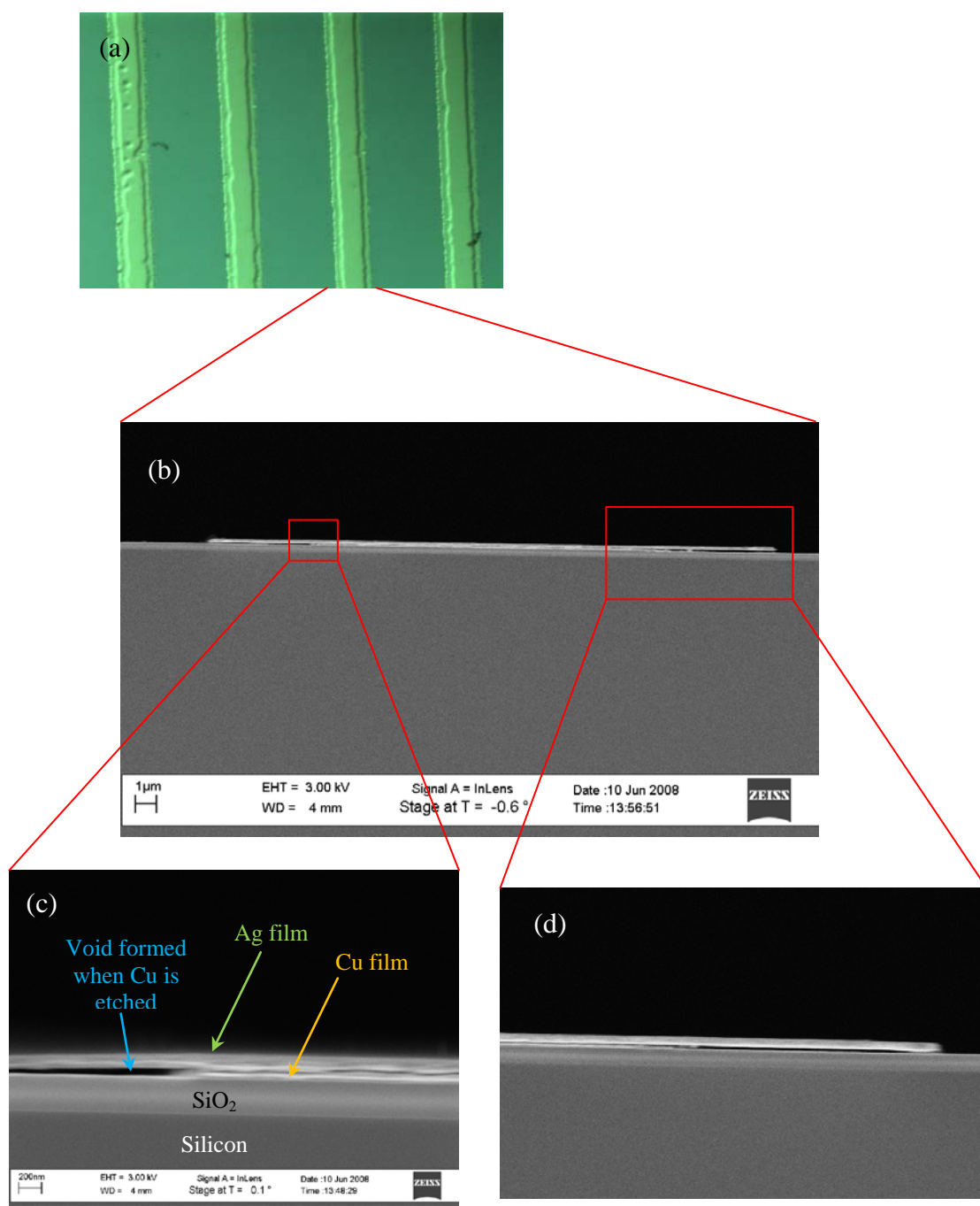
between Cu and SiO<sub>2</sub>. Ni and Ag interdigitating lines were deposited directly on top of the Cu film using the lift-off process. Electroplating was not used in preparation of this sample. Unprotected 100nm Cu film etches in Cr-etchant in ca. 60 seconds. From Figure 5.23, it can be seen that Cu below Ni and Ag lines was also etched. The etching progressed a lateral distance of ca. 4.5μm from each edge of the line toward its centre. This is very fast rate of etching. Normally lateral etching that progresses under an etch mask has an etch rate similar to that of the unprotected material. If the lateral etching is allowed to continue, in ca. 3 minutes all the Cu below the Ni and Ag lines is etched and the Ni and Ag films are removed from the substrate.



**Figure 5.21** (a) SEM image of nickel film that has peeled away from the anode (b) optical image of nickel film that has peeled away from the anode and is in contact with the adjacent cathode, thus causing a short circuit.



**Figure 5.22** SEM image of SC-μDGFC with Pt catalyst for the anode (lower electrode) and Ag catalyst for the cathode (higher electrode). The Pt film do not exhibit peeling, whereas, Ag film has begun to peel from the cathode when Cu seed layer is etched in the Cr-etchant.



**Figure 5.23** (a) Optical microscope image of Ni and Ag lines from the top after Cu etching.

The etching of the underlying Cu layer is visible by the topography of the lines. (b), (c)

& (d) SEM images of cross sectional view of Ag thin film line. The lateral etching of the Cu film below the Ag is clearly visible.

Ti adhesion promotion layer was used to improve the adhesion between Ag and electroplated copper. Whereas, peeling of Ni was avoided by replacing it with Pt film. Despite the used of intermediate Ti film, Ag was peeled from some samples if the



etching lasted for more than 2 minutes. The peeling of the catalyst can be avoided if they are deposited after the seed layer has been etched. This can be accomplished by altering the fabrication process of the SC- $\mu$ DGFC. After electrodeposition of anode and cathode, the seed layer is etched. This is followed by two additional lithography steps to deposit the catalysts on the anode and cathode by lift-off. In the original fabrication process of SC- $\mu$ DGFC, the catalyst is deposited immediately after the electrodeposition which makes it a self-aligned process. In the alternate fabrication process, the additional lithography step to deposit the catalyst on the electrodes would require careful alignment.

### 5.3 Performance of SC- $\mu$ DGFCs

The fuel-electrolyte solutions that were tested for the SC- $\mu$ DGFCs were:

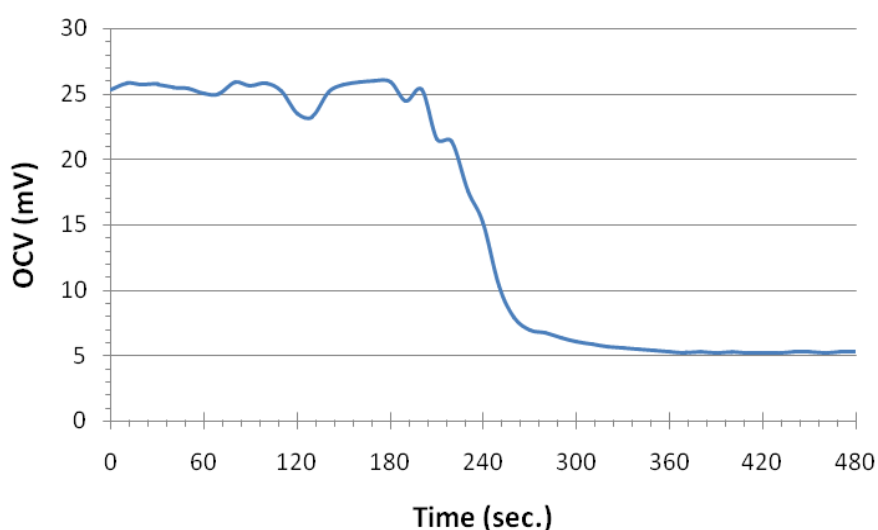
- 1M Ethanol + 0.5 M NaOH, and
- 1M Glucose + 2M KOH.

The SC- $\mu$ DGFC compartment was filled with the fuel-electrolyte solutions using a syringe with a 0.3mm diameter needle. Air trapped inside the PDMS compartment resists the filling. To remove the air from the compartment, a needle (0.3mm diameter) is inserted into the opposite corner of the PDMS compartment while filling the fuel cell with the syringe. Ethanol based solution easily spreads inside the fuel cell compartment. This is facilitated by the capillary action induced by the cathode comb electrode fingers; two adjacent cathode fingers behave as side walls of a capillary channel. Filling the SC- $\mu$ DGFCs with glucose is harder as glucose solution has high viscosity. Some fuel cells were also tested without the PDMS cover. In this case, few drops of the fuel-electrolyte solution were dropped on the fuel cell, while the fuel cell was kept at an inclined angle. The redundant fuel-electrolyte solution flows down and drops from the fuel cell, leaving behind a thin film of the fuel-electrolyte solution on the fuel cell electrodes. This is shown in Figure 5.24.

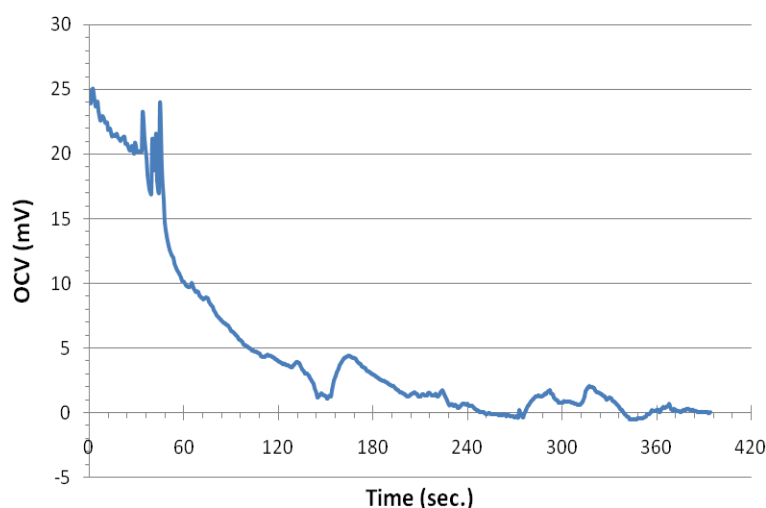


**Figure 5.24** Small sized SC- $\mu$ DGFC without the PDMS cover is being tested.

For ethanol-KOH solution, a very low maximum OCV of 24 - 27mV was recorded (see Figure 5.25). The OCV remains stable for only ca. 3 minutes 20 seconds, before it drops and stabilizes at 5mV. Possible explanations for the drop in OCV are: (i) fuel crossover; oxygen is able to diffuse to the anode in significant amounts and (ii) permeability of PDMS to ethanol vapor; volumetric evaporation of ethanol from the compartment through the entire surface of PDMS membrane may be occurring. However, it is expected that these would cause gradual decrease in the OCV unlike the more abrupt drop in OCV seen in Figure 5.25. The drop in the OCV is also encountered when a fuel cell without the PDMS cover is tested with ethanol solution. In this case, the OCV drops more gradually, starting at ca. 25 mV and reaching zero in about 5 minutes. This result agrees with the hypothesis that ethanol evaporation coupled with oxygen diffusion to the anode causes the OCV to drop from its starting value.



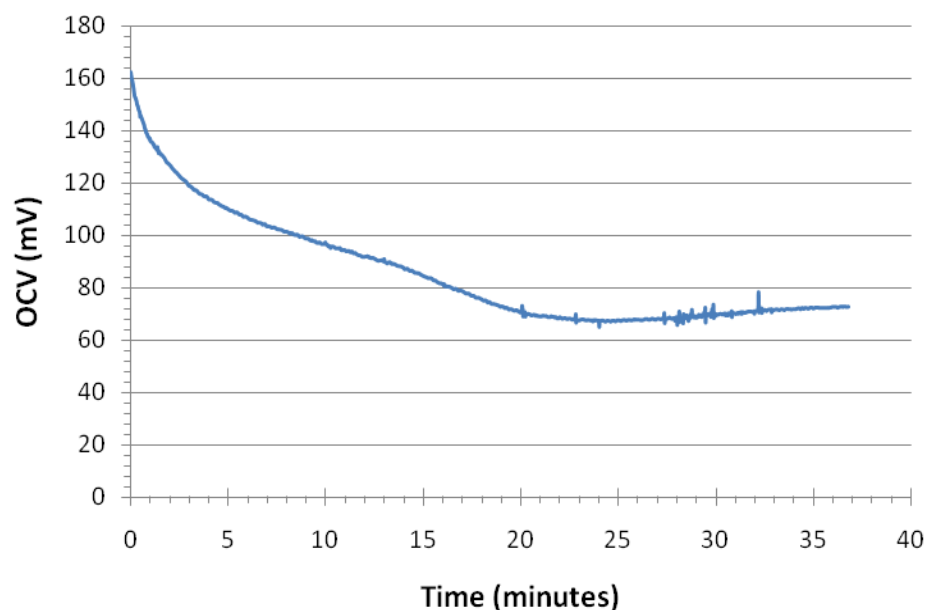
**Figure 5.25** OCV of a SC- $\mu$ DGFC for 1M Ethanol + 0.5 M NaOH fuel-electrolyte solution. The critical dimensions of the fuel cell are: cathode height: 31 $\mu$ m, anode height: 4.5 $\mu$ m, PDMS membrane thickness: 270 $\mu$ m. Catalysts used are: Ag for cathode and Ni for anode.



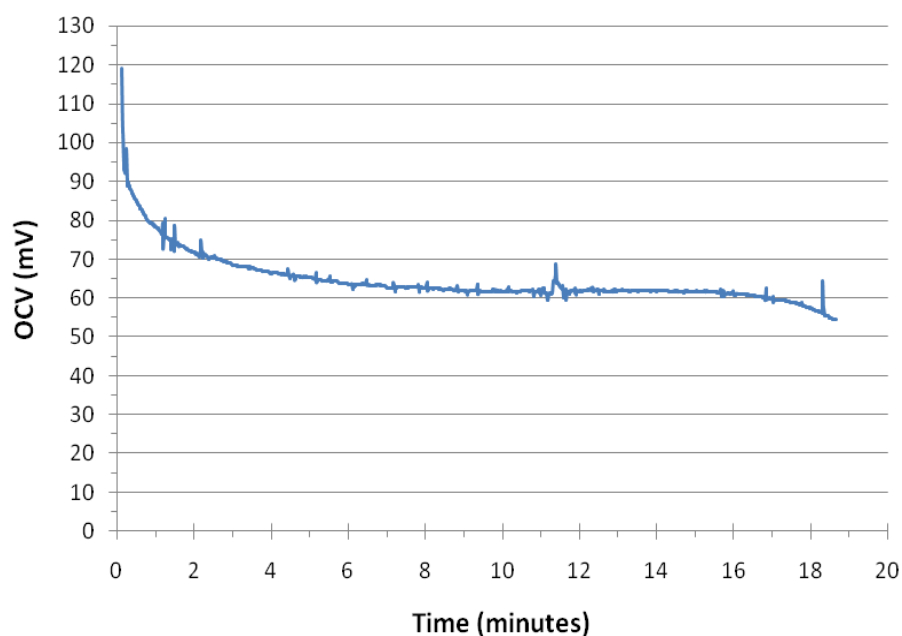
**Figure 5.26** OCV of a SC- $\mu$ DGFC without the PDMS cover. The fuel electrolyte solution used is: 1M Ethanol + 0.5 M NaOH fuel-electrolyte solution. The critical dimensions of the fuel cell are: cathode height: 31 $\mu$ m and anode height: 4.5 $\mu$ m. The Catalysts used are: Ag for cathode and Ni for anode.

OCVs of small scale abiotically catalyzed glucose fuel cells mentioned in literature (and summarized in Table 3.2, page 47) range from 218mV to 850mV. The OCVs obtained from the SC- $\mu$ DGFCs for glucose were much lower compared to these values. Figure 5.27 and 5.28 show the OCV curves for SC- $\mu$ DGFC with PDMS cover tested for 1M Glucose + 2M KOH solution. The result presented in Figure 5.27 show that the fuel cell gave initial OCV of ca.160mV, which gradually decreased with time and stabilized to a value between 65-75mV after ca. 20 minutes. It is suspected that the gradual decrease in OCV is related to the gradual permeation of oxygen through the PDMS and its subsequent saturation in the fuel electrolyte solution with time. A SC- $\mu$ DGFC without PDMS was also tested for 18 hours and it registered a stable OCV in the range of 60 - 65mV for major duration of the test. Maximum OCV of ca. 135mV was recorded for one of the SC- $\mu$ DGFC without the PDMS membrane (Figure 5.30). The OCV was measured while keeping the fuel cell in inclined orientation, so that the redundant glucose can run off from the fuel cell (see Figure 5.24).The OCV gradually increases from its starting value of ca. 45 mV and reaches 135mV in 90 minutes. This increase may be explained by the fact that as the glucose flows off the fuel cell, a thinner layer is left behind and the access of oxygen to the cathode is improved. For this particular SC- $\mu$ DGFC, a current of 64 $\mu$ A was recorded at 0.01 mV. For electrode area of 0.17 cm<sup>2</sup> (small SC- $\mu$ DGFC), this corresponded to a power density of 0.38 $\mu$ W/cm<sup>2</sup>. This

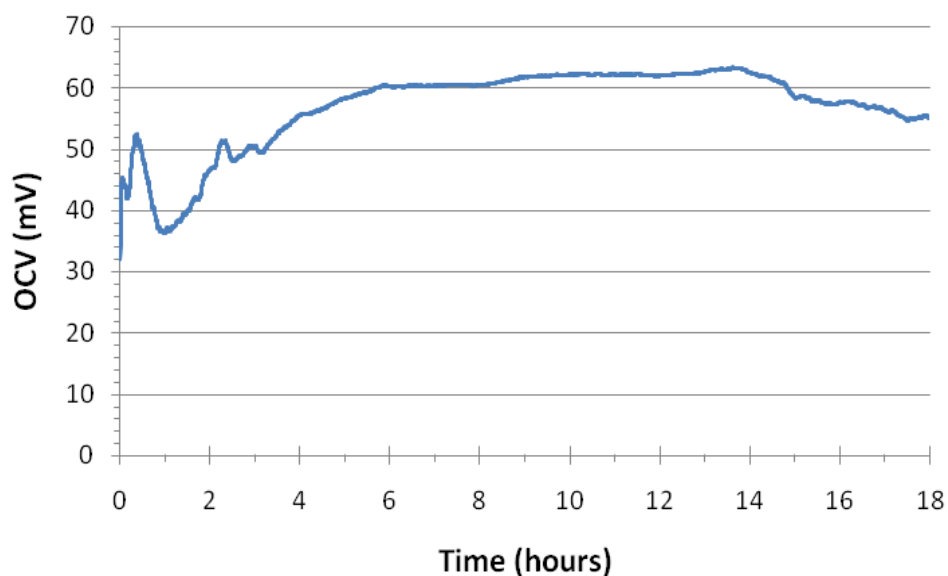
is a very low value when compared to the power densities of DGFCs mentioned in Table 3.2.



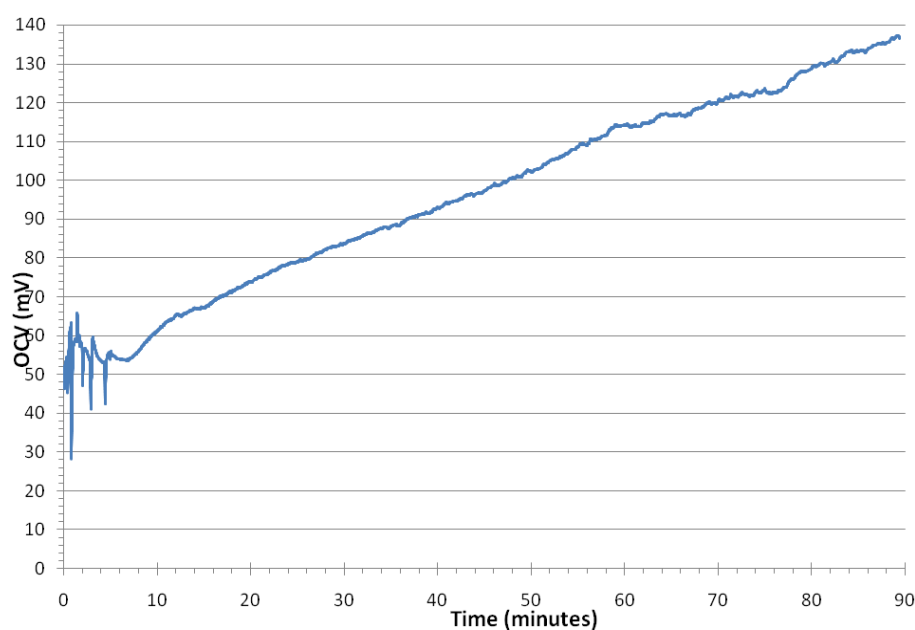
**Figure 5.27** OCV of a SC- $\mu$ DGFC for 1M Glucose + 2 M KOH fuel-electrolyte solution. The critical dimensions of the fuel cell are: cathode height: 31 $\mu$ m, anode height: 4.5 $\mu$ m, PDMS membrane thickness: 270 $\mu$ m. Catalysts used are: Ag for cathode and Ni for anode.



**Figure 5.28** OCV of a SC- $\mu$ DGFC for 1M Glucose + 2 M KOH fuel-electrolyte solution. The critical dimensions of the fuel cell are: cathode height: 31 $\mu$ m, anode height: 4.5 $\mu$ m, PDMS membrane thickness: 270 $\mu$ m. Catalysts used are: Ag for cathode and Ni for anode.



**Figure 5.29** OCV of a SC- $\mu$ DGFC without the PDMS cover. The fuel electrolyte solution used is: 1M Glucose + 2 M KOH fuel-electrolyte solution. The critical dimensions of the fuel cell are: cathode height: 31 $\mu$ m and anode height: 4.5 $\mu$ m. The Catalysts used are: Ag for cathode and Ni for anode.



**Figure 5.30** Linear increases in the OCV of a SC- $\mu$ DGFC without the PDMS cover. The fuel electrolyte solution used is: 1M Glucose + 2 M KOH fuel-electrolyte solution. The critical dimensions of the fuel cell are: cathode height: 31 $\mu$ m and anode height: 4.5 $\mu$ m. The Catalysts used are: Ag for cathode and Ni for anode.

Possible reason(s) for the poor performance of the SC- $\mu$ DGFC are mentioned below:

- The most likely reason for the poor performance of SC- $\mu$ DGFCs is fuel crossover. The height difference between anode and cathode might not be sufficient to minimize the diffusion of oxygen to the anode. A possible source of oxygen supply to the anode is the fuel-electrolyte solution. The solution was prepared in air and oxygen from the atmosphere also diffuses into the solution.
- Fuel cells usually have electrodes with three phase contact area many times more than their simple geometrical area. However, in case of SC- $\mu$ DGFCs, the three phase contact area is almost the same as the geometrical area of the electrode. This factor must have a significant effect on the performance.
- The cathode top surface is immersed in the fuel-electrolyte solution. This will reduce the three phase contact area. The oxygen would have to diffuse through the glucose to reach the cathode.
- The poisoning of the catalyst is another possibility. The intermediate products of glucose oxidation are known to poison Pt. This may as well be true for Ni and Ag. However, this process would require time, whereas the SC- $\mu$ DGFC exhibit low values from the start of the test. A second very likely source of damage to the catalyst layer is the Cr-etchant used in the etching of the Cu seed layer. Ag and Ni may have reacted with the Cr-etchant to form another chemical compound on the surface that would act as a barrier for the reactants. The oxidation of the Ni and Ag when exposed to air can also be source of degradation of fuel cell performance.
- The electrical resistance of current collectors of SC- $\mu$ DGFCs may be high. Unlike conventional stack type fuel cells, the current distribution in the SC- $\mu$ DGFC will be non uniform across its current collector. This is because the electrode fingers near the contact pads are more accessible for current compared to electrode fingers at the end of the current collector line.

## Conclusions

---

Micro fuel cells are a promising alternate to batteries due to their large energy density, rapid refuelling capability and non-polluting operation. Different types of micro fuel cells have been developed using a variety of materials and microfabrication technologies. Micro fuel cells have power densities that range from a few  $\mu\text{W}/\text{cm}^2$  to several hundred  $\text{mW}/\text{cm}^2$ .

A novel single compartment micro direct glucose fuel cell (SC- $\mu$ DGFC) has been developed using microfabrication technologies. The fuel cell design features a single compartment for the glucose/electrolyte solution, which was shared by the interdigitating anode and cathode comb electrodes. The compartment itself was formed of polydimethylsiloxane (PDMS), which also serves as the membrane through which oxygen from ambient environment is able to permeate to the cathode. Single compartment fuel cells suffer from severe fuel crossover losses. Two features were incorporated in the SC- $\mu$ DGFC design to minimize the losses associated with fuel crossover: (i) silver was used as the catalyst to selectively reduce oxygen in the presence of glucose and (ii) cathodes were made 25-45  $\mu\text{m}$  higher than the anode to minimize the diffusion of oxygen to the anode with Ni or Pt catalyst.

SC- $\mu$ DGFCs were fabricated using microfabrication technologies. The comb electrodes were fabricated using UV-LIGA process. The height and wall profile of the comb electrode fingers depends on the processing parameters of the AZ4562 electroplating mask. Fuel cells with cathode height of ca. 30 and 50  $\mu\text{m}$  were fabricated. The catalysts were deposited on the anode and cathode using the lift-off process. The PDMS compartment/membrane was fabricated using the moulding process. The master for the moulding process was fabricated using SU-8. The PDMS compartment is bonded to the substrate with the electrodes using oxygen plasma assisted bonding method. The

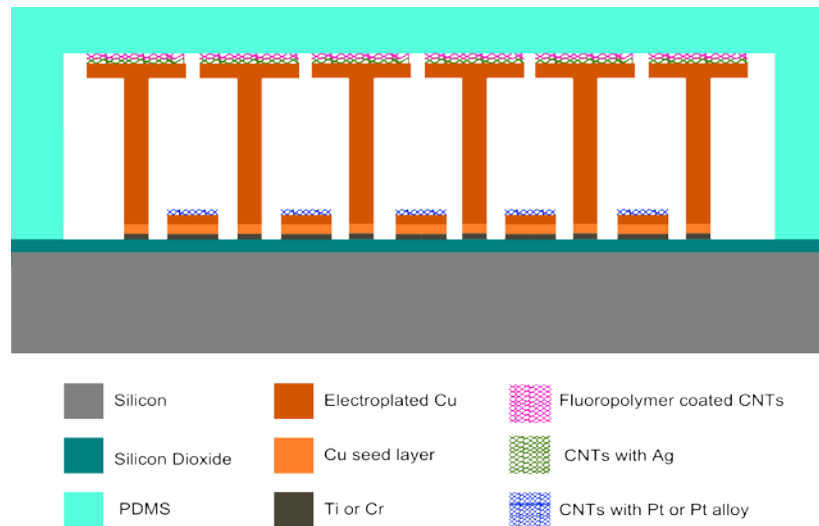
smallest sized fuel cells were the least susceptible to fabrication defects. The key defects in fabrication which lead to short circuiting of the fuel cells were: (i) presence of contaminants on the seed layer which inhibited the etching of the Cu seed layer from some parts and (ii) peeling of Ni and Ag catalyst films from the electrode fingers during Cu seed layer etching in the Cr-etchant solution (ammonium cerium nitrate and perchloric acid). The peeling is attributed to an electrochemical effect, which induces rapid laterally directed etching of Cu below the catalyst layer. These two defects can be eliminated by etching the Cu seed layer before the catalysts are deposited on the electrodes.

Some fuel cells with Ni and Ag as the catalysts provided meaningful results. The rest of the SC- $\mu$ DGFCs were damaged due to the above mentioned defects in the fabrication process. SC- $\mu$ DGFCs were tested for glucose as well as ethanol. For 1M ethanol mixed with 0.5 M NaOH, only ca. 25mV OCV was recorded which gradually dropped to 5mV after ca. 3 minutes. SC- $\mu$ DGFCs which were tested for 1M Glucose + 2M KOH solution gave relatively better performance. SC- $\mu$ DGFCs with 270 $\mu$ m thick PDMS membrane gave initial OCV in the range of 120 - 160mV which gradually decreased with time and stabilized to a value o between 60-70mV. It is suspected that the gradual decrease in OCV is related to the gradual permeation of oxygen through the PDMS and its subsequent saturation in the fuel electrolyte solution with time. SC- $\mu$ DGFC was tested without PDMS membrane for 18 hours and it registered a stable OCV of ca. 60-70mV for major part of the test. Another SC- $\mu$ DGFC, tested without the PDMS membrane and kept at an inclined angle so as to leave only a thin layer of fuel-electrolyte solution on the cathodes, reported a maximum OCV of ca. 135mV. This increase in OCV is likely due to better access of oxygen to the cathodes. For this fuel cell a power density of 0.38mW/cm<sup>2</sup> was measured.

The low performance of the SC- $\mu$ DGFC is mainly attributed to significant fuel crossover losses due to the diffusion of oxygen to the anode. In addition to fuel crossover, probable factors for low performance of the fuel cells are: low number of reaction sites, cathode flooding leading to limited access of oxygen to the cathode, catalyst poisoning by intermediate products formed during glucose oxidation, chemical change in the catalysts when exposed to Cr-etchant solution, and uneven current distribution in the current collector. Changes must be made in the design of the SC- $\mu$ DGFC to improve its performance. Following design features are proposed for future SC- $\mu$ DGFCs:



- The diffusion of oxygen to the anode may be minimized by increasing the height of the cathode. It should be possible to fabricate above 100 $\mu$ m high cathode comb electrode fingers using chemically amplified thick positive resists like AZ 40XT-11D by AZ Electronic Materials. With this photoresist, film thickness as high as 120  $\mu$ m are possible [144]. A more robust method to minimize fuel crossover losses would be to create an oxygen depleted region near the anode. This may be accomplished by fabricating cathode fingers with mushroom or T-shaped cross section as shown in Figure C.1 and reducing the gap between adjacent anode and cathode fingers. Larger area of the cathode fingers would mean that more oxygen is consumed at the top of the fuel cell compartment and less oxygen will be available to diffuse to the anode. In addition to this T-shaped cathode, other configurations like meshed shaped cathodes and integrating oxygen reducing catalyst particles in the PDMS membrane itself might help in creating oxygen depleted region inside the fuel cell compartment.



**Figure C.1** Revised design of SC- $\mu$ DGFC featuring T-shaped cathodes fingers. The catalysts are supported on CNTs. The cathode fingers also have a GDL formed of fluoropolymer coated CNTs.

- The three phase contact area of the SC- $\mu$ DGFC can be increased by using carbon nano tubes (CNTs) as the catalyst support material (see Figure 5.31). Layers of CNTs can be selectively deposited on substrates using the

lift-off process. For the SC- $\mu$ DGFCs, a 50-60nm layer of CNTs can be deposited on the electrode comb fingers, followed by the deposition of 10-30nm catalyst film by sputtering or e-beam evaporation and lift-off. Number of reaction sites may also be increased by spray coating catalyst ink (see Section 3.3.3) on the electrodes. It may be possible to accomplish this by lift-off. However, the presence of solvents in the catalyst ink layer may partially dissolve the underlying resist. For cathode, activated carbon would have to be used instead of Pt/C in the catalyst ink. The catalyst ink has proton conducting Nafion solution; thus an acidic electrolyte would have to be used instead of alkaline.

- The access of oxygen to the cathode can be improved by depositing fluoropolymer coated CNTs on its surface. This GDL like structure can be fabricated by first depositing a 50-100 nm layer of CNTs on the cathode and then coating the CNT layer by plasma deposited Teflon like fluoropolymer. The fluoropolymer coated CNTs should behave as hydrophobic layer that will minimize the flooding of the cathode by the fuel-electrolyte solution while providing access to the underlying catalyst layer to ambient air.
- Pt-Bi, Pt-Pb or Pt-Ru alloy can replace Ni or Pt as the catalyst for glucose oxidation. These alloys are known to be less susceptible to catalyst poisoning as explained in Chapter 3.
- The effect of metal etchants on the catalysts can be eliminated by etching the seed layer before the deposition of catalysts.
- The electrical resistance of the current collectors can be reduced by increasing their thickness. This can be accomplished by fabricating the current collectors using Cu electroplating instead of defining them in the Cu seed layer.

## References

---

- [1] C.K. Dyer, Fuel cells for portable applications, *Journal of Power Sources*, Vol. 106, 2002, 31–34.
- [2] J.D. Morse, Micro-fuel cell power sources, *Int. J. Energy Res.*, Vol.31, 2007, 576–602.
- [3] N.T. Nguyen and S.H Chan , Micromachined polymer electrolyte membrane and direct methanol fuel cells—a review, *J. Micromech. Microeng.*, Vol. 16, 2006, R1–R12.
- [4] T. Pichonat and B.G. Manuel, Recent development in MEMS-based miniature fuel cells, *Microsyst Technol*, Vol.13, 2007, 1671–1678.
- [5] A. Kundu et al., Micro-fuel cells – Current development and applications, *Journal of Power Sources*, Vol.170, 2007, 67–78.
- [6] J. Larminie and A. Dicks, *Fuel Cell Systems Explained*, 2nd ed., John Wiley and Sons Ltd, 2003.
- [7] A. Heller, Miniature biofuel cells, *Phys. Chem. Chem. Phys.*, Vol. 6, 2004, 209–216.
- [8] S. Franssila, *Introduction to Microfabrication*, John Wiley and Sons Ltd, 2004.
- [9] G.J. La O’ et al., Recent advances in microdevices for electrochemical energy conversion and storage, *Int. J. Energy Res.*, Vol. 31, 2007, 548–575.
- [10] J.P. Meyers, et al., Design considerations for miniaturized PEM fuel cell, *Journal of Power Sources*, Vol.109, 2002, 76–88.
- [11] L. Carrette et al., *Fuel Cell–Fundamentals and Applications*, Fuel Cells, Vol.1, No.1, 2001, 5–39.
- [12] F. de Bruijn, The current status of fuel cell technology for mobile and stationary applications, *Green Chem.*, Vol. 7, 2005, 132–150.
- [13] R.A. Bullen et al., Biofuel cells and their developments, *Biosensors and Bioelectronics*, Vol. 21, 2006, 2015–2045.

- [14] F. Davis and S.P.J. Higson, Biofuel cells – Recent advances and applications, *Biosensors and Bioelectronics*, Vol. 22, 2007, 1224–1235.
- [15] J. Kim et al., Challenges in biocatalysts for enzyme-based biofuel cells, *Biotechnology Advances*, Vol. 24, 2006, 296–308.
- [16] S.M. Haile, Fuel Cell Materials and Components, *Acta Materialia*, Vol. 51, 2003, 5981–6000.
- [17] S.K. Kamarudin et al., Overview on the challenges and developments of micro-direct methanol fuel cells (DMFC), *Journal of Power Sources*, Vol. 163, 2007, 743–754.
- [18] S. Kerzenmacher et al., Energy harvesting by implantable abiotically catalyzed glucose fuel cells, *Journal of Power Sources*, Vol. 182, 2008, 1–17.
- [19] S.W. Cha et al., Geometric scale effect of flow channels on performance of fuel cells, *Journal of The Electrochemical Society*, Vol. 151, No. 11, 2004, A1856–A1864.
- [20] T.M. Squires and S.R. Quake, Microfluidics: Fluid physics at the nanoliter scale, *Rev. Mod. Phys.*, Vol. 77, No. 3, 2005, 977–1026.
- [21] D.H. Han and M.A. Kedzierski, Micro effects for single phase pressure drop in microchannels, *I.J. Trans. Phenomena*, 10, 2008, 103–112.
- [22] H.L. Wang and Y. Wang, Flow in microchannels with rough walls: flow pattern and pressure drop, *J. Micromech. Microeng.*, Vol. 17, 2007, 586–596.
- [23] M. Bahrami et al., Pressure drop of fully developed, laminar flow in microchannels of arbitrary cross-section, *Transactions of the ASME*, Vol. 128, 2006, 1036–1044.
- [24] S.W. Cha et al., Electrochemical impedance investigation of flooding in micro-flow channels for proton exchange membrane fuel cells, *Journal of Power Sources*, Vol. 161, 2006, 138–142.
- [25] S.J. Lee et al., Design and fabrication of a micro fuel cell array with “flip-flop” interconnection, *Journal of Power Sources*, Vol. 112, 2002, 410–418.
- [26] K.B. Min et al., Fabrication of novel MEMS-based polymer electrolyte fuel cell architectures with catalytic electrodes supported on porous SiO<sub>2</sub>, *J. Micromech. Microeng.*, Vol. 16, 2006, 505–511.
- [27] J. Yu et al., Fabrication of miniature silicon wafer fuel cells with improved performance, *Journal of Power Sources*, Vol. 124, 2003, 40–46.

- 
- [28] J. Yeom et al., Microfabrication and characterization of a silicon-based millimeter scale, PEM fuel cell operating with hydrogen, methanol, or formic acid, *Sensors and Actuators B*, Vol. 107, 2005, 882–891.
- [29] J.D. Morse et al., Novel proton exchange membrane thin-film fuel cell for microscale energy conversion, *J. Vac. Sci. Technol. A*, Vol. 18, No. 4, 2000, 2003–2005.
- [30] S. Gold et al., Acid loaded porous silicon as a proton exchange membrane for micro-fuel cells, *Journal of Power Sources*, Vol.135, 2004, 198–203.
- [31] K.L. Chu et al., Porous silicon fuel cells for micro power generation, *J. Micromech. Microeng.*, Vol.17, 2007, S243–S249.
- [32] T. Pichonat and B.G. Manuel, Mesoporous silicon-based miniature fuel cells for nomadic and chip-scale systems, *Microsyst Technol*, Vol.12, 2006, 330–334.
- [33] S.C. Kelley et al., Miniature fuel cells fabricated on silicon substrates, *AIChE Journal*, Vol.48, No.5, 2002, 1071–1082
- [34] A.D. Taylor et al., Nanoimprinted electrodes for micro-fuel cell applications, *Journal of Power Sources*, Vol.171, 2007, 218–223.
- [35] Z. Xiao et al., A silicon-based fuel cell micro power system using a microfabrication technique, *J. Micromech. Microeng.*, Vol. 16, 2006, 2014–2020.
- [36] L.Zhu et al., Integrated micro-power source based on micro-silicon fuel cell and a micro electromechanical system hydrogen generator, *Journal of Power Sources*, Vol.185, 2008, 1305–1310.
- [37] S. Tanaka, et al., MEMS-based components of a miniature fuel cell/fuel reformer system, *Chemical Engineering Journal*, Vol. 101, 2004, 143–149.
- [38] R. Hahn et al., Development of a planar micro fuel cell with thin film and micro patterning technologies, *Journal of Power Sources*, Vol. 131, 2004, 73–78.
- [39] M. Müller et al., Micro-structured flow fields for small fuel cells, *Microsystem Technologies*, Vol. 9, 2003, 159–162.
- [40] S.S Hsieh et al., A novel design and micro-fabrication for copper (Cu) electroforming bipolar plates, *Micron*, Vol.39, 2008, 263–268.
- [41] S.H. Chan et al., Development of a polymeric micro fuel cell containing laser-micro machined flow channels, *J. Micromech. Microeng.*, Vol. 15, 2005, 231–236.

- [42] K. Shah et al., A PDMS micro proton exchange membrane fuel cell by conventional and non-conventional microfabrication techniques, *Sensors and Actuators B*, Vol. 97, 2004, 157–167.
- [43] R. O’Hayre et al., Development of portable fuel cell arrays with printed-circuit technology, *Journal of Power Sources*, Vol. 124, 2003, 459–472
- [44] R. Hahn et al., Development of micro fuel cells with organic substrates and electronic manufacturing technologies, in *Proceedings of Electronic Components and Technology Conference*, 2008.
- [45] S. Wagner et al., Influence of structure dimensions on self-breathing micro fuel cells, *Journal of Power Sources*, Vol. 190, 2009, 76–82.
- [46] P.C. Lin, et al., Development and characterization of a miniature PEM fuel cell stack with carbon bipolar plates, *Journal of Power Sources*, Vol. 176, 2008, 207–214.
- [47] A.L.M. Reddy et al., Design and fabrication of carbon nanotubes-based microfuel cell and fuel cell stack coupled with hydrogen storage device, *International Journal of Hydrogen Energy* 32, 2007, 4272 – 4278.
- [49] H.J. Ahn et al., Three-dimensional nanostructured carbon nanotube array/PtRu nanoparticle electrodes for micro-fuel cells, *Electrochemistry Communications*, Vol. 11, 2009, 635–638.
- [50] Y. Zhang et al., Development of MEMS-based direct methanol fuel cell with high power density using nanoimprint technology, *Electrochemistry Communications*, Vol. 9, 2007, 1365–1368.
- [51] Y. Zhang et al., Effects of the nanoimprint pattern on the performance of a MEMS-based micro direct methanol fuel cell, *J. Micromech. Microeng.*, Vol. 19, 2009, 1-6
- [52] S. Liu et al., From nanochannel-induced proton conduction enhancement to a nanochannel-based fuel cell, *Nano Letters*, Vol. 5, No. 7, 2005, 1389–1393.
- [53] K. Kanamura et al., Preparation of composite membrane between a uniform porous silica matrix and injected proton conductive gel polymer, *Chem. Mater.*, Vol. 17, 2005, 4845–4851.
- [54] K.G. Stanley et al., A hybrid sequential deposition fabrication technique for micro fuel cells, *J. Micromech. Microeng.*, Vol. 15, 2005, 1979–1987.
- [55] T. Pichonat and B.G. Manuel, Development of porous silicon based miniature fuel cell, *J. Micromech. Microeng.*, Vol. 15, 2005, S179–S184.

- 
- [56] S.S Hsieh et al., A novel design and microfabrication for a micro PEMFC, *Microsystem Technologies*, Vol. 10, 2004, 121–126.
- [57] C.R. Buie et al., A microfabricated direct methanol fuel cell with integrated electroosmotic pump, in *Proceedings of MEMS 2006*, 2006, 938–941.
- [58] J.P. Esquivel et al., A silicon-based direct methanol micro fuel cell, in *Proceeding of Spanish Conference on Electron Devices*, 2007, 177–180.
- [59] Y. Jiang et al., Design, fabrication and testing of a silicon-based air-breathing micro direct methanol fuel cell, *J. Micromech. Microeng.*, Vol.16, 2006, S233–S239.
- [60] G.Q. Lu, et al., Development and characterization of a silicon-based micro direct methanol fuel cell, *Electrochimica Acta*, Vol.49, 2004, 821–828.
- [61] Y. Zhang et al., Application of nanoimprint technology in MEMS-based micro direct-methanol fuel cell ( $\mu$ -DMFC), *Journal of Microelectromechanical systems*, Vol. 17, No.4, 2008, 1020–1028.
- [62] J. Santander et al., Towards a monolithic micro direct methanol fuel cell, in *Proceedings of IEEE SENSORS Conference*, 2008, 37–40.
- [63] Y.H. Seo and Y.H. Cho, Micro direct methanol fuel cells and their stacks using a polymer electrolyte sandwiched by multi-window microcolumn electrodes, *Sensors and Actuators A*, Vol. 150, 2009, 87–96.
- [64] L. Zhong et al., A silicon-based micro direct methanol fuel cell stack with compact structure and PDMS packaging, in *Proceeding of MEMS 2007*, 2007, 891–894.
- [65] S.C. Yao et al., Micro-electro-mechanical systems (MEMS)-based micro-direct methanol fuel cell development, *Energy*, Vol. 31, 2006, 636–649.
- [66 ] T.J. Yen et al., A micro methanol fuel cell operating at near room temperature, *Applied Physics Letters*, Vol. 83, No. 19, 2003, 4056–4058.
- [67] T. Ito et al., Characteristics of micro DMFCs array fabricated on flexible polymeric substrate, *Electrochemistry Communications*, Vol. 8, 2006, 973–976.
- [68] G.Q. Lu and C.Y. Wang, Development of micro direct methanol fuel cells for high power applications, *Journal of Power Sources*, Vol.144, 2005, 141–145.
- [69] P. Schechner et al., Silver plated electrospun fibrous anode for glucose alkaline fuel cells, *Journal of The Electrochemical Society*, Vol.154 , No.9, 2007, B942–B948.

- [70] S. Kerzenmacher et al., A surface mountable glucose fuel cell for medical implants, in *Proceeding of Transducers and Eurosensors*, 2007, 125–128
- [71] C. Apblett et al., Bio micro fuel cell grand challenge final report, Sandia National Laboratories, 2005. Retrieved on 21 May 2009 from:  
< <http://prod.sandia.gov/techlib/access-control.cgi/2005/055734.pdf> >
- [72] J.R. Rao and G.Richter, Implantable bio-electrochemical power sources, *Naturwissenschaften*, Vol.61, 1974, 200–206.
- [73] K.B. Kokoh et al., On line chromatographic analysis of the products resulting from the electrocatalytic oxidation of D-glucose on Pt, Au and adatoms modified Pt electrodes, *Electrochimica Acta*, Vol. 37, 1992, 1333–1342.
- [74] H. Lerner et al., Electrochemical glucose oxidation on a platinized platinum electrode in Krebs-Ringer solution, *J. Electrochem. Soc.*, Vol. 126, No.2, 1979, 237–242.
- [75] S. Kerzenmacher, et al., An abiotically catalyzed glucose fuel cell for powering medical implants: Reconstructed manufacturing protocol and analysis of performance, *Journal of Power Sources*, Vol. 182, 2008, 66–75.
- [77] U. Gebhardt et al., A special type of Raney-alloy catalyst used in compact biofuel cells, *Journal of Applied Electrochemistry*, Vol. 6, 1976, 127–134.
- [76] S. Kerzenmacher et al., A novel fabrication route yielding self-supporting porous platinum anodes for implantable glucose micro fuel cells, in *Proceedings of Power MEMS*, 2007, 31–34.
- [78] J. Wang et al., Nonenzymatic electrochemical glucose sensor based on nanoporous PtPb networks, *Anal. Chem.*, Vol.80, 2008, 997–1004.
- [79] M. Tominaga et al., Electrocatalytic oxidation of glucose at gold nanoparticle-modified carbon electrodes in alkaline and neutral solutions, *Electrochemistry Communications*, Vol.7, 2005, 189–193.
- [80] S.B. Aoun and I. Taniguchi, Effective electrocatalytic oxidation of glucose at platinum nanoparticle-based carbon electrodes, *Chemistry Letter*, Vol. 37, No.9, 2008, 936–937.
- [81] H.F. Cui et al., Pt-Pb alloy nanoparticle/carbon nanotube nanocomposite: a strong electrocatalyst for glucose oxidation, *Nanotechnology*, Vol. 17, 2006, 2334–2339.
- [82] F. von Stetten, et al., A one-compartment, direct glucose fuel cell for powering long-term medical implants, in *Proceedings of MEMS 2006*, 2006, 934–937.



- 
- [83] A. Klok et al., A single layer biofuel cell as potential coating for implantable low power devices, in *Proceeding of Eurosensors*, 2008, 1416–1419.
- [84] C.K. Colton et al., Analysis of in vivo deoxygenation of human blood, Feasibility study for an implantable biological fuel cell, *Trans. Am. Soc. Artif. Intern. Organs*, Vol. 15, 1969, 187–199.
- [85] F. von Stetten et al., Biofuel cells as micro power generators for implantable devices, in *Proceedings of Eurosensors XX*, 2006, 222–225.
- [86] K.Y Chan et al., Methods and apparatus for the oxidation of glucose molecules, US Patent Application Publication, Pub. No. US2002/0125146 A1, 2002.
- [87] L.Mor et al., Performance of a glucose AFC, in *Proceedings of the 11<sup>th</sup> IEEE International Conference on Electronics, Circuits and Systems*, 2004, 278–281.
- [88] E. Bubis et al., Saccharide fuel cells with platinum particles anode, in *Proceedings of 23rd IEEE Convention of Electrical and Electronics Engineers*, 2004, 350–353.
- [89] S. Ha and R.I. Masel, A miniature air breathing direct formic acid fuel cell, *Journal of Power Sources*, Vol.128, 2004, 119–124.
- [90] C. Rice et al., Direct formic acid fuel cells, *Journal of Power Sources*, Vol. 111, 2002, 83–89.
- [91] J. Yeom et al., Passive direct formic acid microfabricated fuel cells, *Journal of Power Sources*, Vol. 160, 2006, 1058–1064.
- [92] C. Rice et al., Catalysts for direct formic acid fuel cells, *Journal of Power Sources*, Vol.115, 2003, 229–235.
- [93] Y.W Rhee et al., Crossover of formic acid through Nafion<sup>®</sup> membranes, *Journal of Power Sources*, Vol.117, 2003, 35–38.
- [94] E.R. Choban et al., Membraneless laminar flow-based micro fuel cells operating in alkaline, acidic, and acidic/alkaline media, *Electrochimica Acta*, Vol. 50, 2005, 5390–5398.
- [95] E.R. Choban et al., Microfluidic fuel cell based on laminar flow, *Journal of Power Sources*, Vol. 128, 2004, 54–60.
- [96] E.R. Choban et al., Characterization of limiting factors in laminar flow-based membraneless microfuel cells, *Electrochemical and Solid-State Letters*, Vol.8, No.7, 2005, A348–A352.

- [97] A. Li et al., A laser-micromachined polymeric membraneless fuel cell, *J. Micromech. Microeng.*, Vol.17, 2007, 1107–1113.
- [98] E. Kjeang, et al., An alkaline microfluidic fuel cell based on formate and bleach, *Electrochimica Acta*, Vol.54, 2008, 698–705.
- [99] R. Ferrigno et al., Membraneless vanadium redox fuel cell using laminar flow, *J. Am. Chem. Soc.*, Vol. 124, No.44, 2002, 12930–12931.
- [100] J.L. Cohen et al., Fabrication and preliminary testing of a planar membraneless microchannel fuel cell, *Journal of Power Sources*, Vol. 139, 2005, 96–105.
- [101] R.S. Jayashree et al., Air-breathing laminar flow-based microfluidic fuel cell, *J. Am. Chem. Soc.*, Vol. 127, 2005, 16758–16759.
- [102] Z. Shao et al., A thermally self-sustained micro solid-oxide fuel-cell stack with high power density, *Nature*, Vol. 435, No.9, 2005, 795–798.
- [103] A.B. Hütter et al., A micro-solid oxide fuel cell system as battery replacement, *Journal of Power Sources*, Vol. 177, 2008, 123–130.
- [104] B.E. Buegler et al., From macro- to micro-single chamber solid oxide fuel cells, *Journal of Power Sources*, Vol. 171, 2007, 310–320.
- [105] D. Beckel et al., Thin films for micro solid oxide fuel cells, *Journal of Power Sources*, Vol. 173, 2007, 325–345.
- [106] L. Zhu et al., Hydrogen generation from hydrides in millimeter scale reactors for micro proton exchange membrane fuel cell applications, *Journal of Power Sources*, Vol. 185, 2008, 1334–1339.
- [107] S. Moghaddam et al., A self-regulating hydrogen generator for micro fuel cells, *Journal of Power Sources*, Vol. 185, 2008, 445–450.
- [108] D.E. Park et al., Micromachined methanol steam reforming system as a hydrogen supplier for portable exchange membrane fuel cells, *Sensors and Actuators A*, Vol. 135, 2007, 58–66.
- [109] A.V. Pattekar and M.V. Kothare, A microreactor for hydrogen production in micro fuel cell applications, *Journal of Microelectromechanical Systems*, Vol.13, No.1, 2004, 7–18.
- [110] C.R. Buie et al., Water management in proton exchange membrane fuel cells using integrated electroosmotic pumping, *Journal of Power Sources*, Vol. 161, 2006, 191–202.

- 
- [111] T. Metz, et al., Micro structured flow-field for passive water management in miniaturized PEM fuel cells, in Proceedings of IEEE MEMS 2007, 2007, 863–866.
- [112] J.C. McDonald and G.M. Whitesides, Poly(dimethylsiloxane) as a material for fabricating microfluidic devices, *Accounts of Chemical Research*, Vol. 35, No.7, 491–499
- [113] I.D. Bo et al., Investigation of the permeability and selectivity of gases and volatile organic compounds for polydimethylsiloxane membranes, *Journal of Membrane Science*, Vol. 215, 2003, 303–319.
- [114] S.M. Mitrovski and R.G. Nuzzo, An electrochemically driven poly(dimethylsiloxane) microfluidic actuator: oxygen sensing and programmable flows and pH gradients, *Lab on a Chip*, Vol.5, 2005, 634–645
- [115] S.M. Mitrovski et al., Microfluidic devices for energy conversion: planar integration and performance of a passive, Fully Immersed  $H_2$ - $O_2$  Fuel Cell, *Langmuir*, Vol.20, 2004, 6974–6976.
- [116] C.K. Malek and V. Saile, Applications of LIGA technology to precision manufacturing of high-aspect-ratio micro-components and -systems: a review, *Microelectronics Journal*, Vol.35, 2004, 131–143.
- [117] W. Qu et al., UV-LIGA: a promising and low-cost variant for microsystem technology, in Proceedings of Conference on Optoelectronic and Microelectronic Materials Devices, 1999, 380–383.
- [118] V. Con'ed'era and M. Dilhan, A simple optical system to optimize a high depth to width aspect ratio applied to a positive photoresist lithography process, *J. Micromech. Microeng.*, Vol. 7, 1997, 118–120.
- [119] MicroChemicals GmbH, Application notes–Thick resist processing, 2007. Retrieved on 20 November 2008 from:  
<[http://www.microchemicals.eu/technical-information/thick\\_resist\\_processing.pdf](http://www.microchemicals.eu/technical-information/thick_resist_processing.pdf)>.
- [120] Apex Instruments Company, Brief theory of spin coating process, 2009. Retrieved on 22 September 2009 from:  
<<http://www.apexicindia.com/SpinCoatingTheory.htm>>
- [121] S Roth et al., High aspect ratio UV photolithography for electroplated structures, *J. Micromech. Microeng.*, Vol.9, 1999, 105–108.
- [122] Swiss Federal Institute of Technology Zurich, Clariant AZ 4500 Series Data Sheet, 2009. Retrieved on 30 June 2009 from:

- <[http://www.first.ethz.ch/infrastructure/Chemicals/Photolithography/Data\\_AZ4500.pdf](http://www.first.ethz.ch/infrastructure/Chemicals/Photolithography/Data_AZ4500.pdf)>
- [123] MicroChemicals GmbH, Application notes–Softbake of photoresist films, 2007. Retrieved on 20 November 2008 from  
<[http://www.microchemicals.eu/technical-information/softbake\\_photoresist .pdf](http://www.microchemicals.eu/technical-information/softbake_photoresist.pdf)>
- [124] MicroChemicals GmbH, Application notes–Rehydration of photoresist films, 2007. Retrieved on 20 November 2008 from:  
<[http://www.microchemicals.eu/technical-information/photoresist \\_rehydration .pdf](http://www.microchemicals.eu/technical-information/photoresist _rehydration.pdf)>
- [125] B. Loechel, Thick-layer resists for surface micromachining, *J. Micromech. Microeng.*, Vol.10, 2000, 108–115.
- [126] H. Miyajima and M. Mehregany, High-aspect-ratio photolithography for MEMS applications, *Journal of Microelectromechanical Systems*, Vol. 4, No. 4, 1995, 220–229.
- [127] Y.Cheng et al., Wall profile of thick photoresist generated via contact printing, *IEEE Journal of Microelectromechanical Systems*, Vol. 8, No. 1, 1999, 18–26.
- [128] E. Cullmann, Suss MicroTech AG, Presentation on Thick film resist advances, 2004. Retrieved on 26 May 2009 from:  
<[http://www.sussmicrotec.de/presentations/secap/ResistProcessing/SussMicroTec\\_Cullmann.pdf](http://www.sussmicrotec.de/presentations/secap/ResistProcessing/SussMicroTec_Cullmann.pdf)>
- [129] A. Heuberger and B. Löchel, Optical DUV-lithography for high microstructures, *Microsystem Technologies*, Vol.3, 1996, 1–6.
- [130] W. Ruythooren et al., Electrodeposition for the synthesis of Microsystems, *J. Micromech. Microeng.*, Vol. 10, 2000, 101–107.
- [131] D.C. Gilkes et al., Effect of copper seed aging on electroplating-induced defects in copper interconnects, *Journal of Electronic Materials*, Vol. 31, No. 10, 2002.
- [132] J. Reid, Copper electrodeposition: Principles and recent progress, *Jpn. J. Appl. Phys.*, Vol.40, 2001, 2650-2657.
- [133] J.C. McDonald et al., Fabrication of microfluidic systems in poly(dimethylsiloxane), *Electrophoresis*, Vol. 21, 2000, 27–40.
- [134] A. Folch et al., Molding of deep polydimethylsiloxane microstructures for microfluidics and biological applications, *Transactions of the ASME*, Vol. 121, 1999, 28–34.

- 
- [135] MicroChem,NANO<sup>TM</sup> SU-8 Negative tone photoresist formulations 50-100 datasheet, 2002. Retrieved on 18 May 2009 from:  
<[http://www.microchem.com/products/pdf/SU8\\_50-100.pdf](http://www.microchem.com/products/pdf/SU8_50-100.pdf)>
- [136] E.H. Conradie and D.F. Moore, SU-8 thick photoresist processing as a functional material for MEMS applications, *J. Micromech. Microeng.* , Vol.12, 2002, 368–374.
- [137] A. Mata et al., Fabrication of multi-layer SU-8 microstructures, *J. Micromech. Microeng.*, Vol. 16 , 2006, 276–284
- [138] J.K. Kallio and P.J.Kallio., PDMS and its suitability for analytical microfluidic devices, in *Proceedings of the 28th IEEE EMBS Annual International Conference*, 2006, 2486–2489.
- [139] M. Datta and D. Landolt, Fundamental aspects and applications of electrochemical microfabrication, *Electrochimica Acta* , Vol. 45, 2000, 2535–2558.
- [140] A. Wu and D.P. Barkey, Pattern recognition and scaling studies of copper electrodeposition on Cu(100) in the presence of additives, *J. Electrochem. Soc.*, Vol. 150, 2003, C533–C537.
- [141] A.O. Acquah et al., Transition in surface growth from self-affine to mounds during copper electrodeposition, *J. Electrochem. Soc.*, Vol. 153, 2006, C535–C539.
- [142] M.Saitou et al., Surface roughening in the growth of direct current or pulse current electrodeposited nickel thin films, *J. Electrochem. Soc.*, Vol.148, 2001, C780–C783.
- [143] K.R. Williams et al., Etch rates for micromachining processing-Part II, *Journal of Microelectromechanical Systems*, Vol.12, No.6, 2003, 761-778
- [144] AZ Electronic Materials, AZ 40XT Series – Chemically amplified positive tone thick photoresist for etch and plating applications, 2008. Retrieved on 25 August 2009 from:  
<[http://www.az-em.com/PDFs/40xt/az\\_40xt\\_photoresist.pdf](http://www.az-em.com/PDFs/40xt/az_40xt_photoresist.pdf)>